Multiscale wavelet and upscaling-downscaling for reservoir simulation

Imperial College London
Department of Department of Earth Science and Engineering

Multiscale Wavelet and Upscaling-Downscaling for Reservoir Simulation

Masoud Babaei

January 2013

Supervised by Prof. Peter R. King

Submitted in part fulfilment of the requirements for the degree of
Doctor of Philosophy in Department of Earth Science and Engineering of Imperial College London
and the Diploma of Imperial College London

Abstract

The unfortunate case of hydrocarbon reservoirs being often too large and filled with uncertain details in a large range of scales has been the main reason for developments of upscaling methods to overcome computational expenses. In this field lots of approaches have been suggested, amongst which the wavelets application has come to our attention.

The wavelets have a mathematically *multiscalar* nature which is a desirable property for the reservoir upscaling purposes. While such a property has been previously used in permeability upscaling, a more recent approach uses the wavelets in an operator-coarsening-based upscaling approach. We are interested in enhancing the efficiency in implementation of the second approach. the performance of an wavelet-based operator coarsening is compared with several other upscaling methods such as the group renormalization, the pressure solver and local-global upscaling methods.

An issue with upscaling, indifferent to the choice of the method, is encountered while the saturation is obtained at coarse scale. Due to the scale discrepancy the saturation profiles are too much averaged out, leading to unreliable production curves. An idea is to downscale the results of upscaling (that is to keep the computational benefit of the pressure equation upscaling) and solve the saturation at the original *un-upscaled* scale. For the saturation efficient solution on this scale, streamline method can then be used.

Our contribution here is to develop a computationally advantageous downscaling procedure that saves considerable time compared to the original proposed scheme in the literature. This is achieved by designing basis functions similar to multiscale methods used to obtain a velocity distribution.

Application of our upscaling-downscaling method on EOR processes and also comparing it with non-uniform quadtree gridding will be further subjects of this study.

The publications from this work are:

M. Babaei, P.R. King (2012), "*A modified nested-gridding for upscaling-downscaling in reservoir simulation*", Journal of Transport in Porous Media, **93**(3), 753-775

M. Babaei, A. H. Elsheikh, P.R. King, "*A comparison study between an adaptive quad-tree grid and uniform grid upscaling for reservoir simulation*" , submitted to Journal of Transport in Porous Media

M. Babaei, P.R. King, "*An Upscaling-Static-Downscaling Scheme for Simulation of Enhanced Oil Recovery Processes*", submitted to Journal of Transport in Porous Media

Conference proceedings:

M. Babaei, P.R. King, "*A modified nested-gridding for upscaling-downscaling in reservoir simulation*" International Conference on Flows and Mechanics in Natural Porous Media from Pore to Field Scale - Pore2Field 16-18 November 2011

M. Babaei, P.R. King, "*A Comparison between wavelet and renormalization upscaling methods and iterative upscaling-downscaling scheme*" SPE Reservoir Simulation Symposium, 21-23 February 2011, The Woodlands, Texas, USA

M. Babaei, P.R. King, "*Upscaling reservoir simulation using multilevel operator coarsening*" presented at XVIII Conference on Computational Methods in Water Resources, 21-24 June, 2010. Barcelona, Spain

Contents

List of Tables

List of Figures

1 Introduction

The work flow of reservoir studies is an integration of interdisciplinary works by the geophysicists, reservoir geologists, petrophysicists and reservoir engineers. The reservoir studies can be outlined as follows:

The objectives of reservoir simulation are to estimate oil and gas reserves, predict reservoir performance, make decision regarding reservoir management for process design and strategic planning.

Reservoir simulation can be used to estimate recovery factor alongside analogy or analytical methods. Recovery factor, in its turn, is used in the estimation of reserves (see e.g. Demirmen, 2007; Rietz & Usmani, 2009).

To obtain maximum net present value from a field the engineer or the engineering team must identify and define all individual reservoirs and their physical properties and deduce each reservoir's performance. Such reservoir performance studies lead to estimation of expected production rates of oil, water and gas or prediction of recovery, estimation of water/gas breakthrough time for water/gas injection, design of facilities, plan for the safe drilling of additional wells, prevention of drilling of unnecessary wells, identification of the number of wells required, plan for the optimal placement, spacing and completion of wells, representation of highly deviated or horizontal wells and determination of the present and future needs for artificial lift.

Moreover reservoir simulation helps to determine initiation of operating controls at the proper time, and to consider all important economic factors. Future improvement in oil recovery with pressure maintenance by re-injection of produced gas or by water injection into an aquifer can also be evaluated. Early and accurate identification and definition of the reservoir system is essential to effective engineering (Essley, 1965). The various predictions using different production, well and injection scenarios are interpreted and ranked according to acceptability.

Additionally, the application of enhanced oil recovery (EOR) processes requires that the field possesses the necessary characteristics to make application successful. Model studies can assist in this evaluation. Reservoir simulations can take into account detailed areal variations in reservoir properties to design a sound enhanced recovery process (Carlson, 2003).

Uncertainty is an important factor in reservoir engineering that is conjoined with

reservoir simulations. There is a need to run multiple realisations to assess uncertainty of the models in oil recovery and future production. Uncertainty in reservoir data can be classified into uncertainty in geophysical, geological, dynamic and reservoir fluids data (Schulze-Riegert & Ghedan, 2007) and is usually investigated by constructing several different realisations of the sets of attribute values. The behaviour of the resulting simulation models can indicate the associated level of economic uncertainty.

For example consider the situation that we wish to build a reservoir simulation model to investigate what parameters our model is sensitive to and also to obtain an estimated range of values of some objective function (e.g. total oil production or gas in place). Rather than running just one instance of the simulation model with just one set of parameter values, we would really like to run as many simulation model instances as possible (given time and budget constraints), each simulation run having its own set of parameter values and resulting in a new estimated objective function value (e.g. total oil production). Hence, the multiple number of models are produced. Some models will be optimistic, some pessimistic, but all are designed to characterise the reservoir and the uncertainty about the reservoir (Farmer, 2005). There is a definite trend toward ensemble reservoir forecasting, where a wide range of models are developed that sample probability distributions of reservoir parameters. Running all of these simulation models helps us to quantify the range of uncertainty in our objective function and we should be able to pull out forecast values.

There are various methods for quantifying uncertainties in reservoir simulations (see e.g. Floris *et al.*, 2001; Barker *et al.*, 2000). One obvious observation is that, quantification of geological uncertainty relies on having high-quality upscaled reservoir model that honours the geological model details, because while we are quantifying uncertainties based on such details we are not able to do so on the geological model itself. In this case the workflow to generate such an upscaled model is as follows:

Firstly, a high resolution geological model for the reservoir is provided through the application of an integrated workflow that includes robust seismic and petrophysical analysis. The objective is to design a static model that includes reservoir heterogeneities and internal baffles and barriers to flow and account for inherent degree of uncertainty that is related to the partial knowledge of the reservoir and the limitations of the techniques that are commonly utilised.

The static description of the reservoir, both in terms of geometry and petrophysical properties, is one of the main controlling factors in determining the field production performance (Cosentino, 2001).

Once a detailed reservoir model has been constructed, the next step is to build a reservoir simulation model by *upscaling* of the geological model and run reservoir sim-

ulations. The results of actual production analysis obtained from field are used for comparison to reservoir simulations, in a process called *history-matching*, using parameters representative of the field. The idea is to match gas oil ratios, water cuts, and pressures predicted by the model to actual real-time performance data. In general, some previously unknown aspects of the reservoir (uncertainties) will become apparent by the analysis of production performance. The objective is to determine why the reservoir performance is not matching our production. This knowledge is used to correct our conceptual model of reservoir and devise plans to improve reservoir performance (Carlson, 2003). At this stage the application of Bayes' rule can be used to update our prior probability assessment performed previously and to produce the posterior probability distribution (see e.g. Busby *et al.*, 2007).

Reservoir monitoring to study the changes that occur in a reservoir during production is performed. The monitoring can include renewed seismic surveys or log and core data designed to detect changes that occur during production. These *dynamic* data are integrated into the geological model and subsequently into the reservoir simulation model in order to assess changes and to edit input data for the simulator. The data is used to manage the reservoir, and to make or revise decisions that will drive production plans for the future.

The above-mentioned stages of reservoir engineering studies should be tightly integrated in order to foster more effective, less expensive reservoir engineering projects (Cosentino, 2001).

In the sections that follow, we describe the geological and reservoir simulation models and the upscaling/gridding process that links up these models.

1.1 Geological Fine Scale Model

Flow processes occur in reservoirs involving large gaps in scales. The extent of scale is so wide that we have kilometre scale of reservoirs on one hand and micrometre scale of the pore channels on the other. In between these scales, we may have centimetre scale of the wells. In order to model the reservoir, we attempt to recreate the true geological heterogeneity in the reservoir rock by static geological models which are commonly referred to as geomodels.

The geomodels typically have several components. The first component of is the structural framework that incorporates the spatial positions of the major boundaries of the formations, including the effects of rock uncorformities such as faulting, folding, and erosion. The information for this stage comes from different sources. For example, seismic surveys can be used to obtain a description of the geological structure of the reservoir at

a resolution of metres. Exploratory wells can be drilled to collect further data at specific locations. The major stratigraphic divisions obtained are further subdivided into layers of cells with geometries with relation to the bounding surfaces. Subsequently, maximum cell dimensions are dictated by the minimum sizes of the features to be resolved.

Next, for each cell in the model we assign a rock type. Rock type probability maps control the distribution of the rock types within the model. Also we can emplace statistical distributions of rock type based on well data that are spaced sufficiently closely. Subsequently, the reservoir petrophysical parameters including porosity and permeability must be assigned for each cell.

Different sources at different scales are used to obtain information for porosity and permeability. Seismic surveys provide distributed but low resolution information about the reservoir whilst data from wells (logs and tests) is only describing the reservoir around the well. The wells can be separated by 100 m or 1 km. Consequently the sources present separate and small contributions with their limited data at limited resolutions and at relatively high cost of acquirement.

In summary, the process of making a geological model is generally strongly underdetermined (Aarnes *et al.*, 2007). To resolve the issue, spatial statistics, often called geostatistics that is concerned with problems of interpolation under conditions of uncertainty, are used to populate the cells with porosity and permeability values that are appropriate for the rock type of each cell. Using geostatistical techniques one builds petrophysical realisations in the form of grid models that both honour measured data and satisfy petrophysical trends and heterogeneity.

Having built a geological model with values for the rock properties that are averaged and interpolated from the microscopic physics of flow in pores, the resulting geomodel, subsequently, can barely reflect all pertinent scales that impact fluid flow. Small scale features such as flow through narrow high permeable channels, radiant flow around the well or important detailed geological features are not properly resolved by a geomodel. One important aspect, however, is that at this coarse scale, Darcy's law applies.

1.2 Simulation Upscaled Flow Model

Unfortunately, after all averaging, interpolation and data populating, from a simulation point of view, geological models are ironically too complex and too large, i.e., they contain more information than we can handle in simulation studies. Therefore, we usually use a coarsened grid model, or a simulation flow model. The model consists of grid blocks with their petrophysical properties replaced by averaged or upscaled quantities based on variations of underlying geomodel quantities that occur at length

scales below the simulation grid block. The main reason for using the upscaled models is computational limitations since it is usually impossible to perform flow simulations on the geomodel. However it is worth mentioning that, the advent of new computers with high computational capabilities gives a hope that the fine scale geological models will be directly used for flow simulation. To this hope one must notice that the sizes and complexity of geomodels have been increasing continuously and simultaneously with the enhancement of computer memory and processing power. Therefore, considering this current trend, the upscaling of geomodels seems an unavoidable stage of reservoir studies.

The computational justifications of using a coarse upscaled model for flow simulation is more emphasized once we acknowledge the fact that in the geostatistical interpolation of data to create a fine geomodel, most of the information obtained is of a statistical kind and should be treated as such. To account for the uncertainty in our knowledge of the reservoir, multiple models should be produced (Farmer, 2005). Consequently it is more desirable to use a simulation model with less computational expenses for multiple runs that provides a reliable trend and are easier to history-match than using a geomodel for a single run that provides a detailed yet uncertain result.

In the upscaling techniques that coarsen the geomodels to simulation models, the effective petrophysical properties are calculated in each cell of the simulation grids based on properties of the underlying geomodels. In this process, the aim is to preserve as much as possible the small scale effects in the large scale computations. Systematic small scale variations in permeability and porosity can have a significant effect on a larger scale, and this should be captured in the upscaled model. The quality of upscaling is usually assessed by comparing upscaled production characteristics with those obtained from a reference solution computed on an underlying fine grid (Aarnes *et al.*, 2007). The closer the production predictions of an upscaling technique for a reservoir model is to those obtained by the fine scale reference model, the better the upscaling technique is rendered.

Upscaling techniques are mainly classified into single phase and multiphase flow upscaling methods. In multiphase flow upscaling, the problem is to upscale relative permeabilities and capillary pressure, that exist only for multiphase flow, in addition to absolute permeability and porosity. Reviews on single phase flow upscaling can be found for example in Renard & de Marsily (1997) and Farmer (2002). Reviews on multiphase flow upscaling can be found in Barker & Thibeau (1997) and Das & Hassanizadeh (2005).

There are numerous upscaling techniques developed for the absolute permeability, as the main property to upscale in reservoir engineering. On one hand, we have absolute

permeability upscaling techniques, e.g. Journel *et al.* (1986), that yield upscaled values close to simple averaging where important information about the subgrid flow (flow from the underlying fine geomodel) are more or less discarded. On the other hand, we have more advanced techniques, e.g. Begg *et al.* (1989) and Durlofsky (1991), that deal with solving flow problems over local heterogeneous regions of a geomodel to provide better upscaled values. More complicated upscaling techniques such as Chen & Durlofsky (2006) are generally proved to be robust and reliable for a range of heterogeneity patterns, nevertheless, they require considerable computational efforts compared to the simple techniques.

Alternatively or alongside the absolute permeability and porosity upscaling, for adjusting the grid cells sizes and shapes to the reservoir features, non-uniform and flexible grids can be implemented. Non-uniformity helps to adjust the resolution of a simulation model, avoid averaging for scale-sensitive areas and preserve the effects of these areas on flow. We will describe non-uniform gridding in the next section.

Further to aforementioned averaging issues that arise form upscaling, the coarsening of scale can inflict considerable impact on flow predictions by introducing numerical diffusion error[1]. This error smears the sharp flow fronts which consequently leads to incorrect production forecasts particularly where the number of grid blocks between wells is small (Carr & Christie, 1983; Lantz, 1971). Inaccuracy is in the form of earlier breakthrough times of production or lower water cut productions at later times for an upscaled model compared to a realistic geomodel. The sensitivity of an upscaling technique to the coarsening of geomodel, can be analysed and solutions can be proposed by downscaling techniques. In downscaling, the resolution of solution is restored, and it means that at some stage, for a part of flow solution, the original fine scale geomodel is used. The implementation of downscaling, however, must align with the benefits of upscaling.

An upscaling-downscaling procedure is dual-mesh approach (Ramé & Killough, 1992; Guérillot & Verdière, 1995; Gautier *et al.*, 1999; Audigane & Blunt, 2004). In the dual-mesh approach, the pressure equation is upscaled to reduce computational effort whereas the saturation is solved at the fine scale to minimize the discretization error. The switch from the coarse scale of pressure to the fine scale of saturation requires a downscaling procedure. The decisive factor here is to produce fine scale inputs for the saturation solver derived from the upscaled model that produces accurate results compared to use of inputs provided by the geomodel.

The procedures to add fine scale solutions adaptively to the upscaling, or set up algorithms that enhance the upscaling altogether are referred to as multiscale methods

[1]Numerical diffusion is the first order truncation error form discretization of partial differential equations whereas numerical dispersion describes the higher order errors.

where both the geomodel and the coarse flow model are interactively employed.

The single phase flow upscaling techniques, that we will review in the next chapter, Section 2.2, each has particular inherent deficiencies. Such deficiencies can be broadly attributed to other currently available upscaling techniques, in particular, the problem is discarding the heterogeneities and averaging out the subgrid flows (the homogenization/upscaling error). This is very serious, for heterogeneous permeability fields, for two techniques that we chose: the renormalization and the pressure solver methods. However more recent method of adaptive local global upscaling resolves this issue to a satisfying degree. Nevertheless, in our experiments we could not resolve the diffusion error for this technique that affect the well production curves. This is due to the fact that the flow pattern is no longer uniform around a well and the pressure gradient typically increases close to the well and becomes highly sensitive to the spatial variation of permeability (Desbarats, 1992). One solution to the problem could be adding near-well upscaling techniques (see e.g. Ding, 1995; Durlofsky *et al.*, 1999; Mascarenhas & Durlofsky, 2000; Muggeridge *et al.*, 2002), however, we used downscaling to address diffusion error instead.

1.3 Non-uniform Grid Generation

Alongside the implementation of computationally complicated upscaling techniques to better capture the fine scale heterogeneity of geomodel, one can look at the potential of non-uniform gridding. An alternative to regular grid upscaling is to design irregular and unstructured grids that include fewer degrees of freedom and save computations. This approach is favoured bearing in mind that the use of uniform regular coarse grids introduces errors which can be avoided if the grid lines are designed to follow the streamlines or at least the regions of flow. The impact of a uniform upscaling for high flow regions appears in the form of errors in the coarse scale velocity field and incorrect saturation profiles. As a result, unreliable predictions (e.g. exaggerated sweep and inaccurate breakthrough times) are often observed from uniform upscaling of highly heterogeneous geological models.

The design of a non-uniform grid involves adaptive adjustment of the mesh resolution for physical processes that occur at a wide range of spatial and temporal scales. Non-uniform grid generation can be thought of as a grid coarsening problem, where grid blocks are merged without compromising the simulation accuracy. Also, it can be thought of as a grid refinement problem where additional grid resolution is locally added throughout the simulation domain to increase the solution quality. For the resulting grid a multilevel upscaling procedure is needed. The procedure depends on the coarse

grid type which can be unstructured or structured, regular Cartesian or geometrically irregular.

In unstructured gridding, the coarse grid blocks can be misaligned with the fine grid so that flow features can be captured more efficiently. One of the most commonly used unstructured grid is Voronoi tessellations or Perpendicular Bisector (PEBI) grid and their dual Delaunay tessellation (see e.g. Mahani & Evazi, 2010; Heinemann *et al.*, 1991; Mlacnik *et al.*, 2006; Palagi, 1992). Delaunay forms the triangles in such a way that circle circumscribing vertices of each triangle does not contain any of the other grid points. Voronoi grid block vertices are obtained from the centre of circles circumscribing the triangle's vertices. Such flexibility can also be achieved by constructing non-uniform Cartesian grids or structured curvilinear or elliptic grids. Non-uniform Cartesian grids are constructed by patch-based refinement or by merging a collection of fine scale Cartesian cells. Curvilinear grid is a grid with the same structure as a regular grid, in which the cells are quadrilaterals or cuboids rather than rectangles or rectangular parallelepipeds.

Different criteria can be used for adapting the grid. For example, geometrical or geological information of reservoirs such as high permeability areas, fractures, faults or boundaries can be used (see e.g. Farmer *et al.*, 1991; Li *et al.*, 1995). Also, the grid can be adjusted non-uniformly based on information obtained by the solution of a flow problem (see e.g. Durlofsky *et al.*, 1996, 1997; Darman *et al.*, 2001; Wen *et al.*, 2003; Prevost *et al.*, 2005). This presents a possibility where grids can be constructed based on streamlines where areas with high density of streamlines are candidates for refinement. Furthermore, the grid can be aligned with streamlines to capture the flow paths efficiently.

In permeability grid adaptation, generally, the heterogeneous areas of the domain were left at the finer scales and the homogeneous regions were coarsened. For example Qi *et al.* (2001) refined a grid block if the permeability variance is higher than a pre-specified threshold. Flow-based gridding or streamline-based gridding requires the solution of a fine scale problem. It is assumed that flow field will not undergo severe changes in later times of the simulation (Castellini *et al.*, 2000). The requirement of initial fine scale solution imposes a fairly small computational cost relative to the simulation of the multiphase system (Durlofsky, 2005a).

Both criteria of flow and permeability variations can be combined for adapting the grid. Wen & Gómez-Hernández (1996) introduced an iterative procedure to add velocity variations to the grid constructed by Garcia *et al.* (1992). Elliptic Jacobian-based gridding was also proposed by He (2005) and He & Durlofsky (2006). It involves deriving the solution of a set of nonlinear elliptic equations and obtaining a transformation

operator to map from physical to logical Cartesian space. A grid was constructed using both the obtained map and streamline information. This method is fast and simple to apply. However, in some cases, the convergence is slow and there is no guarantee the grid will have non-intersecting coordinate lines (Durlofsky, 2005a).

Under any circumstances and geometries of the resulting constructed grid, a proper upscaling must assign coarse properties to the new grid. There are numerous combinations using both gridding and upscaling in reservoir simulations. Acquiring the advantages from unstructured grid depends directly on how well the upscaled values are assigned from the overlaid geomodel cells to each geometrically shape-variant grid blocks. Due to such variation of geometry of grid blocks, upscaling is more difficult and less straight forward than for the structured grid. To compound difficulties of unstructured gridding, one must account for the computational overheads caused by extra bookkeeping for different shaped grids and loss of uniformity that is enjoyed for the structured grid. Nonetheless, unstructured grid means more flexibility at resolving features of the geomodel.

1.4 Aims and Objectives

For our studies on upscaling, three separate subjects related to the topic will dominate this thesis. First is the application of wavelet transformation in upscaling. Second, is the issue of discretization error and unavoidable loss of resolution in upscaling of the geomodels. The third subject is non-uniform coarse gridding.

The wavelets were applied in the framework of *operator coarsening* approach. The approach aims at solving the Darcy's law in a coarse wavelet-transformed space and constraining the upscaled solution to the fine scale solution. Consequently, a coarse operator acting on the coarse space substitutes the fine scale differential operator. The wavelets are very desirable for this purpose because they have natural multiscale features.

The operator in this work is derived from transforming the pressure into its spatial averages by wavelets. Trying to preserve the structure of Darcy's law, certain parameters within the fine operator are grouped together to form a representative coarse parameter within the upscaled operator. This grouping shares methodological similarities with the renormalization procedure which consists of a progressive and hierarchical coarsening of a fine scale field. Therefore, we will overview the renormalization concept and its upscaling use based on resistor analogy alongside the wavelets.

As we discussed in the previous section, the upscaling results may suffer from numerical diffusion error. The second subject of interest related to upscaling is about this

issue. To reduce the error a suggestion is to use *dual-mesh* approach. For the downscaling stage required, we will propose and test the idea of construction of special basis functions that can be used throughout the simulation. This is the major contribution of this thesis. The method is computationally beneficial in change of scales. The applicability of static downscaling is very similar to application of streamline simulators that take advantage of incompressibility of flow and slow changes in velocity field and hence the streamlines.

Finally, the third subject covered in this thesis is an application of non-uniform quadtree grid generation. The generated grid captures the details of flow by preserving the resolution in areas where the fine scale information are significant for the global solution, elsewhere the grid is upscaled. There are different criteria for the detecting the regions that should be refined. The regular options are guides provided by variation in permeability and flow. Either of these criteria will be attempted in this thesis.

Putting the three subjects together, the aim of this research is to extend the wavelet operator coarsening approach, to describe and apply a state-of-the-art static downscaling for reservoir simulation and to build a non-uniform quadtree grid generation based on permeability and flow solution.

The objectives are:

1. To evaluate the performance of wavelet-based operator coarsening in comparison with several existing upscaling methods for single phase and multiphase flow in terms of accuracy.

2. To evaluate the performance of the proposed upscaling-static-downscaling method, in terms of accuracy and computational efficiency in comparison with fine scale reference solution, for different boundary conditions, various flooding cases and under fine scale heterogeneities that are difficult to upscale.

3. To evaluate the performance of the proposed non-uniform quadtree grid model, in terms of accuracy, in comparison with a computationally demanding upscaling technique for uniform grid.

1.5 Thesis Outline

This thesis is laid out as follows.

In Chapter 2, we will briefly overview general equations of flow in porous media at Darcy's scale. A requirement to better explain dual-mesh approach, downscaling and multiscale methods is to describe the pressure and saturation equations which will be presented in this chapter. Also we review upscaling methods including the renormalization method, the pressure-solver method and the adaptive local-global method. These methods are hoped to cover a range of technically simple-to-advanced and computationally fast-to-slow range of upscaling methods.

Chapter 3 is dedicated to the wavelets. First we introduce the wavelet transformation and then we will present the method of operator coarsening based on Haar wavelets. Finally in this chapter we will investigate the performance of the method compared to those introduced in Chapter 2.

In Chapter 4, we investigate the methods that are designed to solve the equations in a scale-adaptive fashion to reduce the discretization error. The methods of interest are multiscale and upscaling-downscaling. For the former we only review two approaches from literature. For the latter, we present a new method of static downscaling. A results section follows showing the application of static downscaling for two and three dimensional heterogeneous cases of reservoirs. The results are compared to upscaling without downscaling, upscaling with dynamic downscaling and a multiscale method.

In Chapter 5, we use the static downscaling presented in Chapter 4 for a number of enhanced oil recovery processes. The processes are polymer, surfactant and thermal flooding. For each we validate the numerical simulation at the fine scale with Buckley-Leverett analysis. Moreover for increasing the accuracy of numerical simulation in the presence of solutes, we use the scheme of segregation-in-flow.

In Chapter 6, we will describe a quad-tree grid generation based on criteria of permeability and flow. We will compare the results of differently constructed non-uniform grids with uniform upscaling. However, in order to separate the errors of upscaling and discretization, we will apply downscaling on all the uniform and non-uniform methods used in this chapter.

Finally, in Chapter 7, conclusions will be summarized and recommendations for the future works will be given.

2 Upscaling Flow in Porous Media

This chapter presents a brief overview of the literature on upscaling approaches. First, a brief account of the physics and equations for flow in porous media will be provided in Section 2.1, followed by an overview of the literature on upscaling, Section 2.2. The methodologies introduced will be investigated and applied in the next chapters. Most importantly renormalization upscaling, wavelet upscaling and adaptive local-global upscaling are our objectives for comparisons and assessments.

2.1 General Flow Equations

2.1.1 Darcy's Law

Darcy's law originates from experiments conducted by Henry Darcy in 1856 with the flow of water in vertical sand beds (Darcy, 1856). He observed that the velocity of filtration of a fluid through porous media is proportional to a combination of the gradient of the fluid pressure and pull-down effects due to gravity. More precisely, the volumetric flow density $\mathbf{v}$ is related to pressure p and gravity forces through the following gradient law:

$$\mathbf{v} = -\frac{\mathbf{K}}{\mu}(\nabla p + \rho g \nabla z). \tag{2.1}$$

where $\mathbf{K}$ is the tensorial permeability, μ is the viscosity, g is the gravitational acceleration and z is the spatial coordinate in the upward vertical direction.

The continuity (flow) equation for the process of filtration states mass conservation:

$$\frac{\partial \varphi \rho}{\partial t} + \nabla \cdot (\rho v) = Q, \tag{2.2}$$

where $\rho\mathbf{v}$ is the mass flow per unit area per unit time, $\rho\varphi$ is the accumulation of mass per volume due to compressibility, φ the porosity, and Q models sources and sinks, that is, outflow and inflow per volume at designated well locations. By combining Darcy's law with the conservation of flow for an incompressible fluid, that is constant density, with no gravity and unit viscosity, we get:

$$\nabla \cdot \mathbf{v} = -\nabla \cdot [\frac{\mathbf{K}}{\mu}(\nabla p + \rho g \nabla z)] = \frac{Q}{\rho} \tag{2.3}$$

In the case of a homogeneous medium, where $\frac{\mathbf{K}}{\mu}$ is a constant, this reduces to Laplace's equation for pressure and a solution can be found just by specifying the required boundary conditions. In the general case, however, approximate numerical methods can be employed to find a solution, such as finite difference or finite element schemes.

2.1.2 Multiphase Flow

For single phase flow, permeability is assumed to be a rock property and independent of the fluids present. This is only true in the case where the rock is completely saturated with a specific fluid. In the case where two fluids are present, it is necessary to define phase specific permeabilities which are defined as the product of the absolute permeability of the rock and a function of saturation of the phase considered:

$$k_l = \mathbf{K} k_{rl}\left(S_l\right), \tag{2.4}$$

where the subscript l stands for one of three possible phases, oil water or gas, and k_l is the specific permeability of phase l, $\mathbf{K}$ is the rock permeability that was defined for single-phase, and $k_{rl}\left(S_l\right)$ is relative permeability of phase l. Relative permeabilities are functions of saturation, implying that in the presence of more than one phase in the rock, an equation for saturation will also be needed.

Assuming that a generalization of Darcy's law to multiphase flow is valid (Bear, 1972), we need to formulate equations for the flow of each phase (l) using relative permeabilities:

$$\mathbf{v}_l = -\frac{\mathbf{K}k_{rl}\left(S_l\right)}{\mu_l}(\nabla p_l + \rho_l g \nabla z). \tag{2.5}$$

Following Aziz & Settari (1979), we can also generalize the continuity equation to more than one phase:

$$\frac{\partial m_l}{\partial t} + \nabla \cdot \dot{\mathbf{m}}_l = Q_l, \tag{2.6}$$

where m_l is the mass of component l in the unit volume and $\dot{\mathbf{m}}_l$ is the corresponding mass flux. We will limit the discussion to "black-oil" models. The model refers to the assumption that the hydrocarbons may be described as two components: a heavy hydrocarbon component called "oil" and a light hydrocarbon component called "gas". The two components can be partially or completely dissolved in each other depending on the pressure and the temperature, forming either one or two phases (liquid and gaseous). In general black-oil models, the hydrocarbon components are also allowed to be dissolved in the water phase and the water component may be dissolved in the two hydrocarbon phases. However, for further simplifications we assume immiscibility that enforces no mixing between phases. Moreover, the thermodynamic equilibrium between the hydrocarbon phases is modeled via the solubility of the gas in the oil phase.

By introducing saturation S_l as the fraction of the pore volume occupied by phase l, the mass conservation equations for three-phase black-oil model are:

$$\frac{\partial}{\partial t}[\varphi \rho_w S_w] + \nabla \cdot (\rho_w \mathbf{v}_w) = Q_w, \tag{2.7a}$$

$$\frac{\partial}{\partial t}[\varphi \rho_o S_o] + \nabla \cdot (\rho_o \mathbf{v}_o) = Q_o, \tag{2.7b}$$

$$\frac{\partial}{\partial t}[\varphi(R_s \rho_o S_o + \rho_g S_g)] + \nabla \cdot (R_s \rho_o \mathbf{v}_o + \rho_g \mathbf{u}_g) = Q_{fg} + R_s Q_o, \tag{2.7c}$$

where the subscript fg in the first source term of Equation 2.7c stands for free gas, and R_s represents the solubility of gas in oil. Expressions of the following form can be obtained by substituting Darcy's law for each phase in Equation 2.7b:

$$\frac{\partial}{\partial t}[\varphi \rho_o S_o] - \nabla \cdot [\rho_o \lambda_o (\nabla p_o + \rho_o g \nabla z)] = Q_o, \tag{2.8}$$

where we have defined mobility as $\lambda_l = kk_{rl}/\mu_l$.

Additional relationships are provided besides the the fluid flow equations to equate numbers of equations with number of unknown properties. These relationships include:

$$\begin{aligned} S_o + S_w + S_g &= 1, && \text{(2.9a)} \\ P_{cwo} &= p_o - p_w = f(S_w, S_o), && \text{(2.9b)} \\ P_{cog} &= p_g - p_o = f(S_o, S_g), && \text{(2.9c)} \end{aligned}$$

where P_{cwo} and P_{cog} are capillary pressures arising from immiscibility between phases. For increasing readability, the flow equations are usually rewritten into a *pressure equation* and a *saturation equation*.

The pressure equation

The pressure equation is derived by using Equation 2.8 and substituting Equation 2.9a in the time derivatives and introducing the rock and phase compressibilities. Assuming only oil and water, and summing up Equation 2.8 with its water counterpart:

$$\begin{aligned} c_r \varphi \frac{\partial p_t}{\partial t} - \sum_{l=o,w} \nabla \cdot [\mathbf{K}\lambda_l \nabla(p_l + \rho_l g \nabla z)] \\ - \sum_{l=o,w} c_l \left[\nabla p_l \cdot \mathbf{K}\lambda_l \nabla(p_l + \rho_l g \nabla z) - \varphi S_l \frac{\partial p_l}{\partial t} \right] = Q_t, \end{aligned} \tag{2.10}$$

where $c_r = -\left(\partial\varphi/\partial p_t\right)/\varphi$ and $c_l = -\left(\partial\rho_l/\partial p_l\right)/\rho_l$ are rock and phase compressibilities respectively. Other variables, p_t and $Q_t = Q_w/\rho_w + Q_o/\rho_o$ are total pressure and total volumetric flow rates respectively. In the case of incompressible rock and fluid phases, that is, $c_r = c_w = c_o = 0$, Equation 2.10 reduces to:

$$\begin{aligned} \mathbf{v}_t &= \sum_{l=o,w} \mathbf{v}_l = -\sum_{l=o,w} \left[\mathbf{K}\lambda_l \nabla(p_l + \rho_l g \nabla z)\right], \\ \nabla.\mathbf{v}_t &= Q_t. \end{aligned} \tag{2.11}$$

In this equation, to eliminate p_w to have only p_o as unknown, we use the relationship for P_{cwo} (Equation 2.9b). This elimination leads to:

$$\mathbf{v}_t = -\mathbf{K}(\lambda_o + \lambda_w)\nabla p_o - \lambda_w \mathbf{K} \nabla P_{cwo} + (\lambda_o \rho_o + \lambda_w \rho_w) g \mathbf{K} \nabla z, \tag{2.12}$$

where by introducing $\lambda_t = \lambda_o + \lambda_w$ and $\lambda_G = \lambda_o \rho_o + \lambda_w \rho_w$, the final form of pressure

equation for two-phase incompressible black-oil model is:

$$-\nabla\cdot[\mathbf{K}\lambda_t\nabla p_o-\lambda_w\mathbf{K}\nabla P_{cwo}+\lambda_G g\mathbf{K}\nabla z]=Q_t. \tag{2.13}$$

This equation is completed by prescribing some boundary conditions, e.g. no-flow boundary conditions.

The saturation equation

The saturation of each phase is calculated by deriving phase velocity from total velocity and substituting it into the corresponding phase flow equation. For example, for our two-phase flow case, one can derive water phase velocity as:

$$\mathbf{v}_w=\frac{\lambda_w}{\lambda_o+\lambda_w}\mathbf{v}_t-\frac{\lambda_w\lambda_o}{\lambda_o+\lambda_w}\mathbf{K}\nabla P_{cwo}+\frac{\lambda_w\lambda_o}{\lambda_o+\lambda_w}\mathbf{K}(\rho_w-\rho_o)g\nabla z, \tag{2.14}$$

introducing the *fractional flow* function, $f_w=\lambda_w/(\lambda_w+\lambda_o)$, that measures the water fraction of the total flow, for water saturation we have:

$$\varphi\frac{\partial S_w}{\partial t}+\nabla\cdot\left(f_w\left[\mathbf{v}_t-\lambda_o\mathbf{K}\nabla P_{cwo}+\lambda_o\mathbf{K}(\rho_w-\rho_o)g\nabla z\right]\right)=\frac{Q_w}{\rho_w}. \tag{2.15}$$

This equation is completed by assuming boundary conditions, e.g., no-flow conditions, and initial conditions $S_w(x,0)=S_w^0(x)$.

2.1.3 The Finite Difference Discretization

The pressure and saturation equations, in this work, are solved on a Cartesian structured grid using a finite-difference discretization scheme and an IMPES (IMplicit Pressure, Explicit Saturation) solution strategy. A very brief description of this algorithm is given here. More details can be found in References such as Aziz & Settari (1979). For the discretization of the pressure equation, we start with a *two-point flux approximation*. This approximates the flow between two grid cells, i and j over interface of two cells, namely $\gamma_{ij}=\partial\Omega_i\cap\partial\Omega_j$, where Ω_i and Ω_j represent the volume of gridcells in the domain of reservoir Ω.

In finite difference and finite volume schemes, pressures are considered cell-wise constant, so if we rewrite Equation 2.13 as:

$$-\nabla\cdot\boldsymbol{\lambda}\nabla p=r, \tag{2.16}$$

where for notational simplification $p=p_o$, $\boldsymbol{\lambda}=\mathbf{K}\lambda_t(S)$ and $r=Q_t-\nabla\cdot[\lambda_w\mathbf{K}\nabla P_{cwo}]+\nabla\cdot[\lambda_G g\mathbf{K}\nabla z]$, then the flux over interface γ_{ij} by

two-point flux approximation is:

$$v_{ij} = -\int_{\gamma_{ij}} (\boldsymbol{\lambda}\nabla p) \cdot n d\nu, \tag{2.17}$$

where n denoted the outward-pointing unit normal on $\partial\Omega_i$ defined as the the side of gridcell i. In a Cartesian grid layout, with grid sizes of cells i and j denoted by Δx_i and Δx_j, we can use the gradient approximation: $\nabla p_{ij} \approx \delta p_{ij} = \frac{2(p_i - p_j)}{\Delta x_i + \Delta x_j}$. This leads to:

$$v_{ij} = \frac{2(p_i - p_j)}{\Delta x_i + \Delta x_j} \int_{\gamma_{ij}} \boldsymbol{\lambda} \cdot n d\nu. \tag{2.18}$$

Regarding the fact that $\boldsymbol{\lambda}$ is a function of saturation, $\int_{\gamma_{ij}} \boldsymbol{\lambda} \cdot n d\nu$ is replaced by a distance-weighted harmonic average of $\boldsymbol{\lambda}_i$ and $\boldsymbol{\lambda}_j$:

$$\boldsymbol{\lambda}_{ij} = \frac{\Delta x_i + \Delta x_j}{\frac{\Delta x_i}{\boldsymbol{\lambda}_j} + \frac{\Delta x_j}{\boldsymbol{\lambda}_j}}. \tag{2.19}$$

Hence $v_{ij} = -|\gamma_{ij}|\boldsymbol{\lambda}_{ij}\delta p_{ij} = 2|\gamma_{ij}|(\frac{\Delta x_i}{\boldsymbol{\lambda}_i} + \frac{\Delta x_j}{\boldsymbol{\lambda}_j})^{-1}$, where $|\gamma_{ij}|$ is the length (in 2D) or area (in 3D) of the interface. To simplify, *transmissibility* between cells i and j are defined as:

$$t_{ij} = 2|\gamma_{ij}|(\frac{\Delta x_i}{\boldsymbol{\lambda}_i} + \frac{\Delta x_j}{\boldsymbol{\lambda}_j})^{-1}, \tag{2.20}$$

where t_{ij} relates the flow from one block, i to an adjacent block j , in terms of the pressure difference between the blocks.

Integrating Equation 2.17 and summing up the fluxes over all interfaces of cell i, we can write:

$$\sum_j t_{ij}(p_i - p_j) = \int_{\Omega_i} r dx, \quad \forall \Omega_i \subset \Omega. \tag{2.21}$$

The sum is taken over all non-degenerate interfaces. i.e., over all i such that $\partial\Omega_j \cap \partial\Omega_i$ has a positive measure. This gives rise to a system of equation for determining $\mathbf{P} = \{p_i\}$ as:

$$\mathbf{TP} = \mathbf{R}, \tag{2.22}$$

where $\mathbf{T} = \{t_{ij}\}$ is a symmetric, positive definite matrix of coefficients containing transmissibilities and $\mathbf{R} = \{r_i\}$ is the right hand side vector containing contributions from boundary conditions, wells and capillary and gravity effects.

Equation 2.22 is solved implicitly at time step $n + 1$ from $\mathbf{T}$ and $\mathbf{R}$ calculated at time step n. The total fluxes like v_{ij} are then computed in a straight forward substitution from measured pressures. Next, phase saturations can be calculated from a discretized

saturation equation, for example for water we have:

$$\frac{\varphi_i}{\Delta t}(S_{wi}^{n+1} - S_{wi}^{n}) + \frac{1}{|\Omega_i|}\sum_{j \neq i} \mathbf{F}_{ij}(S_w^n) = \frac{Q_i(S_{wi}^n)}{\rho_i}, \tag{2.23}$$

where φ_i is the porosity in Ω_i, Δt is the time step, S_{wi}^n is the cell-average of the water saturation at time n and $\mathbf{F}_{ij}$ is a numerical approximation of the water flux over edge γ_{ij},

$$\mathbf{F}_{ij}(S_w) \approx \int_{\gamma_{ij}} \left(f_w(S)_{ij} \Big[\mathbf{v}_t - \lambda_o \mathbf{K} \nabla P_{cwo} + \lambda_o \mathbf{K}(\rho_w - \rho_o) g \nabla z \Big]_{ij} \right) \cdot n_{ij} d\nu. \tag{2.24}$$

For calculation of the integrand in the above equation, an upstream weighting is used for fractional flow $f_w(S)_{ij}$.

The solution of the pressure equation for geological fine-scale models imposes computational difficulties for reservoir simulators. For example in a finite difference model, a model with N gridcells leads to a matrix of size $N \times N$. Inversion of such matrix can be time consuming. This fact has led to the development of upscaling methods for the pressure equation to gain computational savings. These methods will be reviewed in the next section. We also note that the solution of the saturation equation for the detailed geological model is computationally costly and numerous methods have been designed to reduce computations for this equation. We only suffice to name some of these methods, as they are not objectives of this work. Numerical approaches to solve the saturation equation at fine scale efficiently are namely a block-based overlapping Schwartz technique (Lee *et al.*, 2008) and streamline solvers (Batycky *et al.*, 1997).

2.2 Review of Upscaling Methods

For the pressure equation upscaling one approach is to upscale $\boldsymbol{\lambda}$ and r in Equation 2.16 to have a coarse-scale version of this equation to solve. For single–phase this involves assigning coarse absolute permeability to each coarse grid block where $\boldsymbol{\lambda} = \mathbf{K}$ and averaging r simply over the domain of coarse grid block. For multiphase, flow upscaling involves assigning the coarse $\mathbf{K}\lambda_t$, P_{cwo} and $\lambda_G\mathbf{K}$ to each coarse grid block. The first property includes absolute permeability and total mobility. For the second and third properties, we need to upscale capillary pressure and relative permeability curves as functions of saturation. In the following subsections we briefly review single phase and multiphase upscaling.

2.2.1 Single Phase Upscaling

For single phase permeability upscaling, the problem can be seen as a single stage averaging of absolute permeability. Other properties like density and porosity of each coarse grid block are upscaled by volume-averaging. The permeability however can not be simply volume-averaged. The coarsening process averages out features that are important for capturing the flow paths, thus a correct upscaling method must be able to preserve the connectivity of the reservoir. In upscaling of absolute permeability, two terminologies are used dominantly to refer to the upscaled or averaged permeability: one is *effective permeability* and the other is *equivalent permeability*.

The difference comes from a mathematical point of view. The upscaled permeability is an effective property of the medium when it doesn't vary with the flow conditions to which the medium is subjected. By contrast, if the larger scale does not encompass all the scales of variation of the permeability field, then the averaged permeability is referred to as an equivalent permeability (Durlofsky, 1991). Unlike effective permeability, equivalent permeability is not a constant property of the medium and under different flow conditions is typically expected to vary.

Basically if heterogeneity is on a scale small compared with size of the system, boundary conditions are unimportant and the two concepts are the same. In other words, the equivalent permeability is the same as effective permeability when the region represented by the upscaled permeability is a valid representative elementary volume (REV), or when there exist two distinct length scales of heterogeneity. In the latter case the scale of calculation of equivalent permeability is large relative to the correlation scale of heterogeneity and encompass small scale variations. Unfortunately these conditions are not satisfied for most of the heterogeneities of the reservoirs and due to presence of high variation of permeability field at all scales, we are only able to compute equivalent

permeabilities. When calculating this property, a region is chosen within which equivalent permeability is mathematically valid. If the region coincides with a simulation grid block, then this permeability is the appropriate "equivalent grid block permeability" for use in reservoir simulators.

A common expression for equivalent block permeability denoted henceforth by $\mathbf{k}^*$ for a coarse grid block E, is given by Gómez-Hernández & Journel (1990):

$$\frac{1}{|E|}\int_E \mathbf{K}(x)\nabla p dx = \frac{1}{|E|}\mathbf{k}^*\int_E \nabla p dx. \tag{2.25}$$

which basically relates the equivalent permeability of a coarse grid block to be average flux from an edge of the block divided by average pressure gradient over the block.

This equation can either be solved numerically or in special cases it has an exact analytical solution. The first step is to determine the upper and lower bounds for $\mathbf{k}^*$. The most general bound is that the equivalent permeability is always bigger than the harmonic average, $\mathbf{k}_H$, and smaller than the arithmetic average, $\mathbf{k}_A$, of fine permeability with the coarse grid block (Matheron, 1967). Another more restrictive set of bounds suggested by Cardwell & Parsons (1945) and Renard & de Marsily (1997) sets the lower bound of permeability in a certain direction to be the arithmetic mean of the harmonic means of permeabilities parallel to that directions, $\mathbf{k}_{AH}$, and the upper bound to the harmonic mean of the arithmetic means of permeabilities perpendicular to that direction, $\mathbf{k}_{HA}$.

An example of cases when upscaled permeability is actually an effective property is when permeability and its inverse have the same probability distribution. This happens for the random log-normal distribution and the chess-board configuration. The effective property in such cases is given by the geometric average (Matheron, 1967). For a two-dimensional isotropic statistically homogeneous medium $\mathbf{k}^*$ is given by :

$$\mathbf{k}^* = m_a^{\alpha} m_h^{1-\alpha}, \tag{2.26}$$

where m_a and m_h are respectively arithmetic and harmonic averages, $\alpha \in [0,1]$ is a statistical factor. This corresponds to the Landau-Lifshitz conjecture that was first proposed in terms of electromagnetic fields (Landau & Lifshitz, 1960). Journel *et al.* (1986) also proposed a generalized power average expression which simplifies to the harmonic, arithmetic and geometric means in the specific cases:

$$\mathbf{k}_p^* = \left(\frac{1}{|E|}\int_E \mathbf{K}(x)^p dx\right)^{\frac{1}{p}}. \tag{2.27}$$

The exponent p depends on type of heterogeneity, block shape and size, and the flow

condition in the block. The conditioning to flow also necessitates consideration of the direction of flow for which $\mathbf{k}^*$ is calculated. Generally permeability is tensorial but in many cases ignoring the cross-flow leads to a diagonal equivalent permeability.

Alongside the above attempts, physical theories and stochastic methods are used for calculation of $\mathbf{k}^*$. For instance, effective medium theory (EMT), percolation theory and the analogy between electric conductance and permeability of porous media are notable. For a description and review of such methods we refer the reader to King (1987) and Renard & de Marsily (1997).

Numerical pressure computation techniques

Another way to obtain an equivalent permeability of a specific block is by numerically solving Darcy's equation on the block itself and matching the flow. A numerical method commonly referred to as the *pressure solver method* (PSM) (Warren & Price, 1961; Begg *et al.*, 1989; Christie, 1996) is to obtain and invert the solution of fine pressure calculated over the domain of coarse grid block $E \in \Omega$. The solution is dependent on the choice of boundary condition. One common choice is assuming a generic axis-oriented boundary condition. For example if x is the direction of pressure gradient:

$$\begin{aligned} p(0,y) &= 1, & p(1,y) &= 0, \\ \mathbf{v}(x,0) &= 0, & \mathbf{v}(x,1) &= 0, \end{aligned}$$

From the solution, we can integrate total flow rate, $\overline{q}_x = -\int_{\Gamma_{1,y}} \mathbf{v}(1,y)dy$ by summation of outlet fluxes. Then $\mathbf{k}^*$ in the x direction is:

$$\mathbf{k}^*_{xx} = \frac{-\overline{q}_x.\Delta x}{A\Delta p} \tag{2.28}$$

where Δp is the assumed pressure gradient, Δx is the thickness of the grid block in the x direction, A is the area from which the outlet fluxes exit. By alternating the boundary condition over the sides, we can obtain $\mathbf{k}^*$ for other directions, namely, $\mathbf{k}^*_{yy}$ and $\mathbf{k}^*_{zz}$. The technique in this form yields a diagonal upscaled permeability tensor and ignores the cross terms. Furthermore, due to often an arbitrary and unrealistic boundary condition assumption the result is prone to errors. Later in this chapter, we will address this issue. An alternative, however, is application of different boundary conditions and processing of the fine grid solution so that full tensor $\mathbf{k}^*$ is calculated. For example, (Durlofsky, 1991) implemented periodic boundary condition which means that we assume that each grid block is a periodic cell in a periodic medium. This imposes full correspondence between the pressures and velocities at opposite sides of the block, e.g., to compute $\mathbf{k}_{xx}$

we impose the following boundary conditions:

$$p(1,y) = p(0,y) - \nabla p, \qquad p(x,1) = p(x,0),$$
$$\mathbf{v}(1,y) = \mathbf{v}(0,y), \qquad \mathbf{v}(x,1) = \mathbf{v}(x,0),$$

This approach yields a symmetric and positive definite tensor, and is usually more robust than the directional flow boundary conditions. This is pronounced in case of structures in porous media that may include crossflow. examples of such structures are sedimentary layers where there is either a high angle of inclination or high permeability contrasts or high and low permeability layers of approximately equal thickness (Pickup *et al.*, 1994).

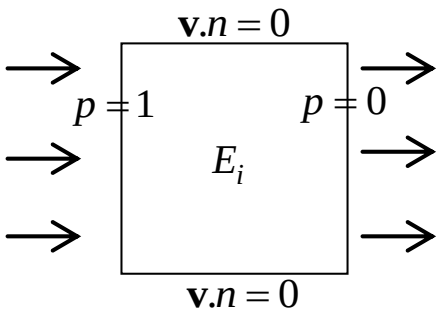

Figure 2.1: Illustration of calculating $\mathbf{k}^*$ for directional PSM for a coarse grid block and boundary conditions imposed.

Renormalization method and renormalization-based methods

Another way to calculate $\mathbf{k}^*$ is the *renormalization method*. Renormalization is a recursive algorithm. The effective properties of small regions of the reservoirs are first calculated and then placed on a coarse grid. The grid is further coarsened and the process repeated until a single effective property has been calculated (King *et al.*, 1993).

The renormalization transformation is by no means unique and many different renormalization schemes have been proposed, some inspired by an analogy between flow in porous media, percolation processes and the flow of currents through resistors (King, 1989). Here we only review examples of *Real-space transformations* as a particular case of the more general concept of the renormalization group. For further discussion and thorough review of "full" real- and momentum-space renormalization method for coarse-graining of subsurface reservoirs we refer to Hristopulos (2003) and Hristopulos

& Christakos (1999). This general treatment has confirmed the applicability of the renormalization concept to upscaling, providing a solution of the problem in all orders of perturbation, even for heterogeneous systems where large fluctuations render other methods unsound.

One of the well known applications of real-space renormalization, presented by King (1989), uses a resistor analogy of flow problem and use of a lattice on which permeability is defined at each lattice cell. In this work, successive star-triangle transformations are used analogous to electric network and finite difference formulation of flow is devised to derive a formula for $\mathbf{k}^*$. The algorithm coarsens simple Cartesian cells hierarchically, that is it coarsens from $N \times N$ to $\frac{N}{2} \times \frac{N}{2}$ to $\ldots$ to 4×4 to 2×2 to a final single value, where N is the number of fine cells. The derivation of the formula is as follows.

A cell-centred finite difference discretization is considered to solve the boundary condition problem defined over four fine cells imposed by inlet and outlet constant pressures. The boundary conditions are the same as used in directional pressure solver method. In addition, an equation is written to relate equivalent permeability $\mathbf{k}^*$ of these four cells to the same pressure difference. By combining the two equations and eliminating the pressure drop and also algebraically inverting the matrix of coefficients, with much of algebra an explicit formula for equivalent permeability is derived:

$$\begin{aligned} \mathbf{k}^* &= f(k_1, k_2, k_3, k_4), \\ f &= \frac{(2(k_1 + k_2)(k_3 + k_4)(k_{12} + k_{34}))}{3(k_1 + k_3)(k_2 + k_4) + \frac{1}{2}(k_1 + k_2 + k_3 + k_4)(k_{12} + k_{34})}, \end{aligned} \tag{2.29}$$

where k_1, k_2, k_3 and k_4 are absolute permeabilities of four constituent fine cells, and k_{12} and k_{34} are harmonic means of permeabilities of the cells with the given subscripts. This value turns out to be very close to directional pressure solver method with the obvious benefit of not having to solve any system of equations. However, the assumption of boundary conditions in the derivation are similar to that of directional pressure solver method. Therefore the same errors are encountered in upscaling by renormalization method in situations that assumed directional boundary conditions do not agree with realistic ones. As with the pressure solver method there are some suggestions to improve renormalization outputs for the equivalent permeability.

One way to improve the renormalization schemes is to use a large cell scheme rather than a small cell one. This means that a large group of cells are upscaled into multiple blocks. This aids in reducing the effects of the artificial boundary effects which are inevitable when single blocks are considered in isolation (Williams, 1992).

Another problem with the method is the discretization scheme. By construction,

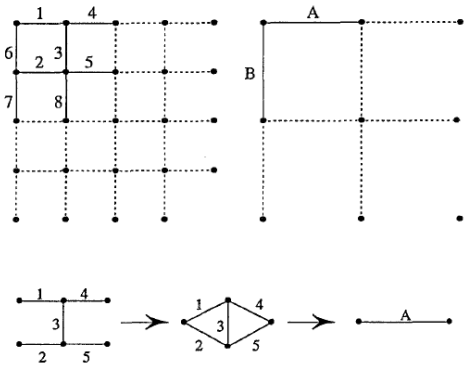

Figure 2.2: Bond renormalization from Hinrichsen *et al.* (1993).

diagonal flow is not allowed and this leads to big errors for example in the chess-board case (Yeo & Zimmerman, 2001). In this case, where sites have alternating high and low permeabilities, flow tends to follow diagonal paths joining the high permeability areas. While, renormalization by Equation 2.29 predicts that the block permeability is controlled by the low permeability value, Dykhne (1971) proved that the exact result (effective permeability) is given by the geometric average. This behaviour cannot be captured by the finite-difference discretization scheme used in the derivation of Equation 2.29. The error caused by the renormalization increases with the contrast between the high and low permeability values (Yeo & Zimmerman, 2001) .

For the method to work, each renormalization block should be bounded by isobars in the direction perpendicular to flow and this is clearly not always the case when the fluctuations in pressure are on scales comparable to the block size. Another suggestion by Gautier & Noetinger (1997) calculates the full tensor of equivalent permeability by renormalization. The modifications of the original scheme is achieved by using a periodic boundary conditions for the pressure gradient. Although the cross-flow effects are not ignored under this scheme, the upscaling still suffers from considering a small group of cells.

In order to estimate the error in renormalization, King (1996) derived another set of explicit formulae for equivalent permeability. In this work, $\mathbf{k}_{AH}$ and $\mathbf{k}_{HA}$, (respectively arithmetic-harmonic mean and harmonic-arithmetic mean of fine permeability), are used in the hierarchical setting and renormalization is used to enhance these means. Firstly, the source of error in the derivation of $\mathbf{k}_{AH}$ and $\mathbf{k}_{HA}$ for a two-dimensional 2×2-cells is studied. The error is shown to originate from the assumption that the flow is either entirely first in the x direction and then is in the y direction or vice versa. It is found that the addition of extra degrees of freedom between the cells on the edges

can cancel out this error. The renormalization procedure in this case is shown to be an approximation scheme to the inversion of a matrix. That is, the pressure differences across the direction of flow are ignored in a mean-field sense by eliminating the degrees of freedom internal to the coarse block. To illustrate this we refer to Figure 2.3. In configuration **a** and **b** if we assume no flow between points 5 and 6 is equivalent to compartmentalize the systems into two subblocks of A and B which leads to $\mathbf{k}_{AH}$ and $\mathbf{k}_{HA}$. Therefore the error arises from the assumption of no cross-directional flow. By finding the equations for this pressure difference, an expression for the error introduced can be obtained. This can be translated into an error in the estimation of the effective permeability computed by $\mathbf{k}_{AH}$ and $\mathbf{k}_{HA}$:

$$\begin{aligned}
\mathbf{k}_{MHA} &= \mathbf{k}_{HA} - \delta\mathbf{k}_{HA}, \\
\delta\mathbf{k}_{HA} &\approx \frac{(k_1k_4 - k_2k_3)^2}{s\big((k_1+k_3)(k_2+k_4) + \frac{1}{3}s(k_{12}+k_{34})\big)}, \qquad (2.30a) \\
\mathbf{k}_{MAH} &= \mathbf{k}_{AH} - \delta\mathbf{k}_{AH}, \\
\delta\mathbf{k}_{AH} &\approx \frac{k_1k_4 - k_2k_3}{4\big(3(k_1+k_3)(k_2+k_4) + \frac{1}{2}s(k_{12}+k_{34})\big)} \times \\
&\quad \left(\frac{2(k_1k_4 - k_2k_3)}{(k_1+k_3)(k_2+k_4)}(k_{12}+k_{34}) + (k_{12}-k_{34})\right), \qquad (2.30b) \\
s &= k_1 + k_2 + k_3 + k_4.
\end{aligned}$$

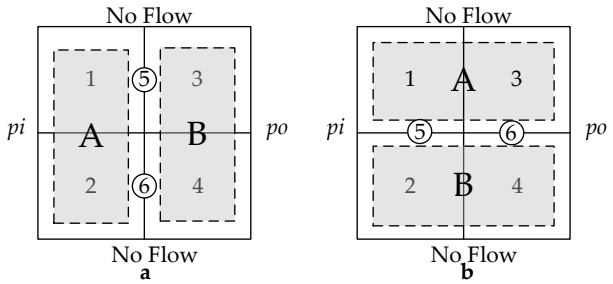

Figure 2.3: Illustration of compartmentalization by assuming no flow between points 5 and 6. This leads equivalent permeability to be $\mathbf{k}_{AH}$ and $\mathbf{k}_{HA}$ respectively in configurations **a** and **b**. The variables *pi* and *po* refer, respectively, to the input and output pressures prescribed on the boundaries.

Again as in renormalization, we have explicit forms which yield direct values for upscaled permeability for 2×2 cells, so we can hierarchically substitute in Equations 2.30a and 2.30b to the desired coarse level.

Wavelets for upscaling

As a continuation of the renormalization scheme (successive grouping of fine cells to yield an average value), here we briefly describe applications of wavelets in upscaling. Wavelets are special functions that represent data in terms of averages and fluctuations. This is a desirable feature for upscaling purposes and has been more or less fully exploited within several descriptions. The full mathematical details of wavelet functions and upscaling formalism will be given in the next chapter, however here we only review the literature and discuss the similarities of wavelet upscaling to the renormalization.

The basic idea underlying wavelets is to decompose a function or a set of data (either continuous or discrete), into basic components and their relative coefficients. In this sense it is very similar to a Fourier transform, where the basic components are sines and cosines and the coefficients are given by their amplitude. Wavelet transforms, however, offer both spatial and frequency resolution (Pancaldi, 2007). For this reason, they have been particularly successfully applied to the analysis of signals where it is necessary to capture both underlying periodic functions and specific localized features, which are almost impossible to represent with periodic components.

There are two distinct wavelet-based upscaling approaches in the literature. First, wavelets can be used to compress information in terms of reducing the number of data points with a filtering procedure. This has been applied in the context of upscaling by Sahimi *et al.* (1983), where a filtering process reduces the number of permeability values in the system without compromising the statistics. This approach leads to *quadtree* or *octree* Cartesian upscaled permeability grids. Another is to apply a wavelet transformation on the flow equations themselves so that we have a coarsened pressure equation. This approach has been extensively applied by Pancaldi *et al.* (2006) and Pancaldi *et al.* (2009) and will be thoroughly analyzed in Chapter 3.

At this point we leave the technical discussion of wavelets to Chapter 3 and it only suffices to mention that the use of wavelets as in the second approach is quite similar to the renormalization group in terms of the hierarchical elimination of permeability fluctuations.. This reveals the basic principle underlying renormalization methods for upscaling.

Local and global upscaling

As shown in Equation 2.25, the problem of averaging for obtaining equivalent permeability, is defined solely on a local domain, for example on the domain of a coarse grid block. This holds for the derivation of $\mathbf{k}^*$ by pressure solver and renormalization methods. As a consequence of this local averaging, we are not able to effectively capture the flow paths and fine grid effects. This is more pronounced when a high correlation

length exists in porous media and connectivities stretch along an area larger than a single coarse block, (see Figure 2.4 for examples of such cases). This limitation leads to errors in upscaling performed *locally*. For reducing the error, there are some suggestions in the literature.

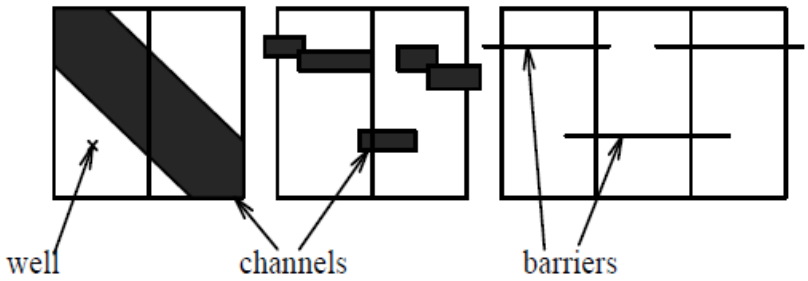

Figure 2.4: Typical coarse grid blocks where local upscaling methods may fail.

The improvements mainly come from considering information obtained non-locally or globally. To define terminologies of local and global upscaling, we refer to the review by Farmer (2002). The upscaling process is subdivided into two phases: *fine-grid experiment* and *coarse grid calibration*. In the first phase, the fine-grid pressure solution is calculated. This can be performed either in the local region that incorporate a single coarse grid block or in the global domain, where the solution is calculated over large portions of the system. The global solution is what upscaling is devised to avoid, since it is computationally demanding. However, as we will discuss later, in multiphase flow upscaling, the global solution of the fine scale pressure equation, only once, requires negligible computations compared to the whole costs of simulation. The second phase, can also be performed locally or globally and it involves finding values for the coarse properties from the fine grid solution. A set of different schemes arise from local and global treatments for each of the two phases: local-local, global-local, global-global and local-global.

Generally local-local methods are exact in $d = 1$, where the flow patterns are trivial. In higher dimensions, though, the flow pattern is non-trivial and depends on boundary conditions and care is needed in applying local-local upscaling methods. An improvement can be made with the use of "jackets", also called oversampling, that is, the value at one specific block is calculated based on an area surrounding it. Another approach to improve the results of local-local methods is to upscale transmissibility rather than permeability itself and this can be combined with oversampling. Later we will discuss transmissibility upscaling in more detail.

In the case of global-local methods, the solution is known for the entire fine grid and

fine scale flux can be integrated to obtain values for the coarsened local permeability. The case of the global-global method is the most demanding and a method suggested by Holden & Nielsen (2000) is based on the minimization of the difference between the fine and coarse scale solutions. The idea is similar to history matching (data assimilation) but uses results from fine scale calculations rather than physical measurements (Farmer, 2002).

For the case of the local-global method, upscaling is performed from the fine grid only in a subregion of the system. The remaining coarse values are interpolated. It reduces processing times considerably. Durlofsky (2005b) also presents an "extended local" approach, which corresponds to the oversampling previously discussed, and suggests it for use on systems where the coarse grid is not aligned with the fine one.

A different local-global method, termed "quasi-global" is defined by Durlofsky (2005b). This upscaling method is performed by an iteration loop to correct the assumed boundary condition used to compute upscaled values. Here, we explain and later will use a version in which a correction is used to upscale transmissibilities. For a coarse scale representation, under the assumption of two point flux approximation, the upscaled transmissibilities, denoted henceforth by $\mathbf{T}^*$ of the interface between two coarse blocks can be computed from the local or extended local problems. The solution of these local problems provides the values of upscaled transmissibilities by:

$$T^*_{m,n} = \frac{\overline{q}_{m,n}}{< p >_m - < p >_n}, \tag{2.31}$$

where $\overline{q}_{m,n} = -\int_{\Gamma_{m,n}} (\mathbf{k}\nabla p).\mathbf{n}dl$ is the total flux obtained by summation of fine grid flow (shown as arrows in Figure 2.5) across the coarse block interface $\Gamma_{m,n}$ between two coarse blocks that contain subblocks m and n. The quantities $< p >_m = \frac{1}{|E_m|}\int_{E_m} \nabla p dx$ and $< p >_n = \frac{1}{|E_n|}\int_{E_n} \nabla p dx$ are the volume averages of the fine scale pressure over subblocks $E_m \subset E_{i,j}$ and $E_n \subset E_{i\pm1,j\pm1}$, respectively. The transmissibility upscaling avoids the secondary error otherwise encountered in calculation of coarse transmissibilities based on upscaled permeabilities (Chen *et al.*, 2003).

If all upscaled transmissibilities T^*_{ij} are positive, then the two point flux approximation scheme for coarse scale will be used for the global solution of coarse pressure p^c as:

$$\sum_{j:\partial E_i \cap \partial E_j \neq \varnothing} T^*_{ij}(p^c_i - p^c_j) = \int_{E_i} Q^c dx, \tag{2.32}$$

where Q^c denotes coarse scale source and sink. In the next iteration, the values of the surrounding coarse scale pressures $p^c_{i\pm1,j\pm1}$ (or global solution) are used to improve the boundary conditions in local upscaling. With new values of upscaled transmissibility a

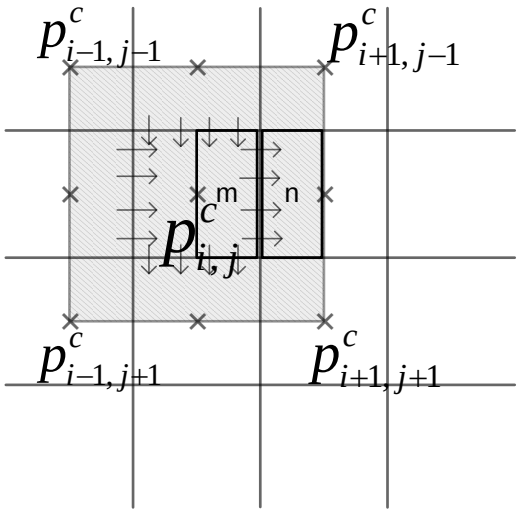

Figure 2.5: An illustration of the application of global information in terms of surrounding coarse pressure that defines boundary conditions for local solvers in transmissibility upscaling. The gray square is the extended region or jacket around coarse target block and thick rectangles represent the area in which volume average pressures are calculated for upscaling.

new iteration is carried out to reach a consistent pressure field and transmissibility set.

The derivation of boundary conditions from global flow is rather a non-trivial task. One approach is to use a bilinear (in 2-D) and trilinear (in 3-D) interpolation of coarse pressure values, $p^c_{i\pm1,j\pm1}$, to provide the local Dirichlet-type boundary conditions. Moreover, the global information obtained by solving coarse scale problem depends on flow scenarios. In Chen *et al.* (2003), authors employed directional generic axes-oriented flows, while in a later version in Chen & Durlofsky (2006), the global information is derived from specific flow scenario. This choice provides coarse scale parameters that are *adapted* for any type of global flow.

2.2.2 Multiphase Upscaling

As was mentioned earlier, for upscaling multiphase flow, in addition to absolute permeabilities, relative permeabilities and capillary pressure should be upscaled. Therefore, it is necessary to express the saturation equation in coarse scale. One way to write an upscaled saturation equation is by assuming that the functional form of these properties does not change with scale. In this case the same relative permeability and capillary pressure curves from fine to coarse scale are used. Unfortunately this suggestion fails in the presence of non-local heterogeneities similar to failure in the case of absolute permeability upscaling. In these circumstances, a multiphase upscaling technique is generally required (Barker & Thibeau, 1997).

Pseudo-function generation

A common approach is to use an averaging technique to generate relative permeability and capillary pressure curves similar to global-local upscaling. For instance, for calculating an upscaled mobility of phase l, denoted by λ_l^*, a fine scale global solution, provides the flow rate between the grid blocks, the pore volume weighted average saturation and viscosity inside the grid block and the pressure gradient across the grid block. To match the phase flow rates between coarse grid blocks E_i and E_j in x direction the following must hold:

$$\sum_{k=1}^{N}(f_l)_k = \overline{f}_l, \tag{2.33}$$

Substituting in Darcy's law for multiphase flow, Equation 2.5 (ignoring gravity), gives:

$$-\sum_{k=1}^{N}\left(t\lambda_l(S)\nabla p\right)_k = -\left(T^*\lambda_l^*(\overline{S})\nabla\overline{p}\right)_{ij}, \tag{2.34}$$

where t and T^* denote fine and coarse transmissibilities. From this expression, some fictitious functions between λ_l^* and S_l can be derived which give rise to generation of *dynamic pseudo relative permeability functions*. The dynamic term refers to the pseudofunctions that are derived from simulated saturation distribution. In contrast, when the flow is dominated by gravity or capillary effects, the saturation distribution may be determined by assuming capillary/gravity equilibrium and *vertical equilibrium* pseudos may be calculated. There are several methods to define pseudofunctions (see Guzman *et al.*, 1999; Kyte & Berry, 1975; Stone, 1991; Jacks *et al.*, 1973). The methods vary in the way they factor the fine grid flow into the product of average quantities, T^*, λ_l^* and $\nabla\overline{p}$. Similarly, the *pseudo capillary pressure curve* is calculated by assigning volume average capillary pressure to the average saturation in the column of grid cells from a reference datum.

Implementation of new functions of relative permeability at coarse scale, leads to an upscaled saturation equation:

$$\frac{\partial\overline{S_w}}{\partial t} + \nabla\cdot F^*(x,\overline{S_w}) = Q_w, \tag{2.35}$$

where $F^*(x,\overline{S}) = \overline{v}f_w^*$, $\overline{v}$ is the upscaled velocity field obtained from coarse scale pressure equation. Here the variation of F_i^* with x appears because the pseudofunctions are in general different for each block in the coarse grid. Finally, $f_w^* = \left\{f_{w,i}^*\right\} = \frac{\{\lambda_{w,i}^*\}}{\{\lambda_{w,i}^*\}+\{\lambda_{o,i}^*\}}$ is the pseudo fractional function for water specifically only for coarse grid block E_i.

Unfortunately pseudofunction generation has several drawbacks. It is computation-

ally expensive in cases that we have to redefine the functions throughout the simulation due to changes in mobilities. The functions are also generally dependent on flow conditions (Aarnes & Efendiev, 2006; Barker & Thibeau, 1997) and they may only be valid for the exact conditions for which they were derived. This is due to the fact that pseudofunctions depend, not only on the heterogeneous porous media structures, but also on the saturation distribution within the grid block and on the reservoir flow history, which in turn depends on well locations and global boundary conditions. Furthermore, from a practical point of view, there are very many such functions as they will differ from one coarse grid block to another.

Volume averaged equations

This approach is an alternative to pseudofunction generation and tries to derive an expression for relating volume average quantities in the saturation equation with some locally calculated fluctuation terms (Durlofsky, 1998). In this idea, S, $\mathbf{v}$ and f_w are expressed in terms of averages ($\overline{S}$, $\overline{\mathbf{v}}$ and $\overline{f_w}$) which are constant within the averaging region and spatial fluctuations ($\tilde{S}$, $\tilde{\mathbf{v}}$ and $\tilde{f_w}$) that have zero mean in the averaging region. By means of averaging an expansion of the saturation equation with $S = \overline{S} + \tilde{S}$, $\mathbf{v} = \overline{\mathbf{v}} + \tilde{\mathbf{v}}$ and $f_w = \overline{f_w} + \tilde{f_w}$, one obtains:

$$\overline{\varphi}\frac{\partial \overline{S}}{\partial t} + \overline{\mathbf{v}} \cdot \nabla \overline{f_w} + \overline{\tilde{\mathbf{v}} \cdot \nabla \tilde{f_w}} = 0, \tag{2.36}$$

$$\overline{\varphi}\frac{\partial \tilde{S}}{\partial t} + \overline{\mathbf{v}} \cdot \nabla \tilde{f_w} + \tilde{\mathbf{v}} \cdot \nabla \overline{f_w} + \tilde{\mathbf{v}} \cdot \nabla \tilde{f_w} = \overline{\tilde{\mathbf{v}} \cdot \nabla \tilde{f_w}}. \tag{2.37}$$

The equation for the fluctuating component can be used to generate equations for various moments of the fine scale saturation equation, see e.g., Durlofsky (1997). Assuming a unit mobility ratio, Efendiev *et al.* (2000) and Efendiev & Durlofsky (2002) derived a single coarse-grid equation from Equation 2.36 on the form:

$$\overline{\varphi}\frac{\partial \overline{S}}{\partial t} + \nabla \cdot G(x, \overline{S}) = \nabla \cdot D(x,t) \nabla \overline{S}, \tag{2.38}$$

where $G(x, \overline{S}) = \overline{\mathbf{v}} f(\overline{S})$ and $D(x,t)$ is a history dependent function that models $\overline{\tilde{\mathbf{v}} \cdot \nabla \tilde{f_w}}$. In fact, compared to the fine scale saturation equation, $D(x,t)$ is an extra *history-dependent* diffusion term that incorporates local fluctuation into a coarse scale saturation equation. The first observation of this formulation is that the coarse scale saturation equation unlike the pressure equation does not take a similar form to the fine continuous scale.

In later developments, Efendiev & Durlofsky (2003), eliminated the history-dependence of Equation 2.38 and corrected $G(x, \overline{S})$ to include convective contributions

resulting from scales larger than the coarse block. The results show reasonable performance in the case of two-phase flow with varying boundary conditions and mobility ratios. To conclude, the methodology is a more process-independent development for coarse scale saturation equation compared to pseudofunction generation. However, in the literature, there is a lack of investigation to extend this approach to include capillary and gravity effects.

Transmissibility upscaling for multiphase

Previously we introduced transmissibility upscaling as an alternative to permeability upscaling in single-phase. We can simply generalize this scheme to multiphase flow upscaling, only if the single transmissibility, T^*_{ij}, is changed to multiphase transmissibility, $\mathbf{T}^*_{ij} = \lambda_t(S)T^*_{ij}$. This requires that we modify transmissibility upscaling problems of the form of Equation 2.31 to:

$$\mathbf{T}^*_{m,n} = \frac{-\int_{\Gamma_{m,n}} (\mathbf{k}\lambda_t(S)\nabla p).\mathbf{n}dl}{< p >_m - < p >_n}, \tag{2.39}$$

which obviously entails recomputation of transmissibilities throughout a dynamic multiphase flow due to changes in $\lambda_t(S)$. A suggestion (Chen & Durlofsky, 2006) is then to use a thresholding technique so in multiphase simulation, after computing a set of upscaled transmissibilities at the initial time step, at the next time step, only a portion of transmissibilities are recomputed. This recomputation is performed only for the coarse blocks where the total mobilities change significantly. A criterion to detect these coarse blocks is (Jenny *et al.*, 2005):

$$\frac{1}{1+\epsilon_\lambda} < \frac{\lambda^{n+1}_{t,i}(S)}{\lambda^n_{t,i}(S)} < 1+\epsilon_\lambda, \tag{2.40}$$

where $\lambda_{t,i}(S)$ denotes total mobility of coarse block i and $\epsilon_\lambda > 0$ is a user-defined threshold value. If any coarse block violates the inequality of Equation 2.40, the transmissibilities of that block must be recomputed.

An advantage of enforcing the thresholding in addition to computational gain is effective elimination of the number of anomalous coarse scale properties in case of local-global multiphase upscaling. Anomalous transmissibility values are encountered when global information (interpolated coarse scale pressure) is not consistent with local regions with low flow rates (Chen & Durlofsky, 2006). This inconsistency is seen when the coarse scale pressures lead to very small pressure difference ($\Delta\overline{p}$). If the integrated flow rate ($\overline{f}$) is also very small, there can be a sign difference between these two values, so the calculated transmissibility will be negative. If $\Delta\overline{p}$ is considerably smaller than $\overline{f}$, the cal-

culated transmissibility in Equation 2.39 becomes anomalously large. By enforcing the threshold, the recomputation of transmissibilities in these low flow regions is avoided.

The methodology above will be used throughout the following chapters for comparison purposes. This involves comparison with directional pressure solver method, renormalization and wavelet upscaling both in single and multiphase cases.

Multiscale and upscaling-downscaling methods

The representation of saturations at a coarse scale leads to a truncation error or numerical dissipation error due to discretization of derivatives. This smears sharp front movement of flow within a coarse block which may ultimately result in wrong predictions of production performance. In order to reduce or eliminate such error, there are mainly two groups of methods that are developed to upgrade an upscaling method: multiscale methods and upscaling-downscaling methods.

Multiscale techniques refer to numerical schemes which model physical phenomena at a coarse scale while preserving underlying fine scale features inside the coarse solution using partial differential equations and corresponding operators at different scale (Kippe *et al.*, 2008; Hesse, 2008).

Generally in most multiscale methods, by imposing different gridding on the global domain (coarse and underlying fine) a set of equations is derived for coarse scale flow calculations and the underlying fine grid. Fine grid equations are locally defined pressure equations which are imposed with special "reduced" boundary conditions (Chen & Hou, 2003). The solution of these problems leads to definition and calculation of pressure (and sometimes velocity) *basis functions*. These functions are used in linear combination to reconstruct fine scale global pressure and velocity solution.

In the multiphase flow case, basis functions must be updated to incorporate multiphase phase flow mobility-dependent variables in the upscaling. This is a major computational burden that is only resolved if adaptivity is practised to maintain the computational efficiency of the original upscaling. By acknowledging the fact that reservoir processes are phenomenologically highly local in space and time, there is a potential to switch back efficiently to fine scale only where and when needed.

As an approximate alternative to multiscale methods, a post-processing downscaling step can be implemented into an upscaling method to reconstruct fine scale velocity field. In so doing, a numerical procedure is performed on coarse velocities that map the results back into fine grid. The resulting fine velocity field is then employed for fine scale saturation calculation (Guérillot & Verdière, 1995).

A detailed technical description of these two approaches will be given in Chapter 4. Moreover, for the upscaling-downscaling method we will suggest and implement tech-

niques for qualitative improvements and computational savings. The application mainly focuses the multiphase flow, however, error reduction for single phase flow upscaling will also be investigated.

3 Wavelets-based Upscaling

In this chapter an upscaling method for absolute permeability, based on Haar wavelets and operator coarsening, will be proposed. The method draws on the application of the Haar transform to Darcy's equation for pressure in single-phase flow in a porous medium. The main idea is to use the Haar wavelet basis to separate the average pressure from the fluctuations in pressure. To a zeroth order approximation, all fluctuations can be neglected, giving a mean-field type result for the average pressure. In the formalism introduced, this can be translated into a very simple upscaling rule for permeability and transmissibility that is inserted into a hierarchical renormalization scheme.

The chapter is laid out into three sections, In Section 3.1 we present an introduction to the mathematics of wavelet transformation. In Section 3.2 the methodology of the pressure equation upscaling with wavelets is described and in Section 3.3 we will use this method in a comparison study with group of single phase upscaling described in the previous chapter.

3.1 Introduction to Wavelets

The wavelet transformation of a function is a localized version of Fourier transform (Daubechies, 1992). This transform has special basis functions that are shifted or technically speaking, translated in the physical domain. As well as translation, "scale" is also considered, which is the main desirable property of wavelet transformation for upscaling. We can either lower or increase the resolution by changing the scale. Based on basis functions of the new scale and their shifts the transformation of the function is carried out repeatedly. These transforms are called wavelets since they behave like localized waves throughout the domain.

Each step of the transformation consists of taking the *averages* (trends) and *differences* (fluctuations) of a function or a dataset. The average coefficients are obtained by scaling functions while the difference coefficients (or wavelet coefficients) are obtained by wavelet functions. The coefficients can be used to retrieve the original function in an inverse transform. The purpose of transformation is that, in image processing for example (where wavelets are very popular), the coefficients of transformation can be filtered out by a threshold. Then with an inverse step, the new approximate image is obtained that contains the same trend but fewer defining points and so requires less storage size.

The simplest scaling (averaging) and wavelet (differencing) functions that are also used in this work are the so-called box or Haar scaling and wavelet functions (Haar, 1909):

$$\phi(x) = \begin{cases} 1 & \text{if } 0 \leq x < 1 \\ 0 & \text{if elsewhere} \end{cases}, \qquad \psi(x) = \begin{cases} 1 & \text{if } 0 \leq x < 1/2 \\ -1 & \text{if } 1/2 \leq x < 1 \\ 0 & \text{if elsewhere} \end{cases}, \tag{3.1}$$

Considering particular function $f(\mathbf{x})$ defined on interval of $[0, 1]$:

$$f(\mathbf{x}) =< f, \phi > \phi(\mathbf{x}) + < f, \psi > \psi(\mathbf{x}), \tag{3.2}$$

where $< f, \phi >= \int f(\mathbf{x})\phi(\mathbf{x})d\mathbf{x}$ and $< f, \psi >= \int f(\mathbf{x})\psi(\mathbf{x})d\mathbf{x}$ respectively determine the coefficients of average and difference basis functions. We can translate or shift scaling and wavelet functions, tile the domain, and perform integrations to determine coefficients over all the tiles. It is noticeable that the mean value of $\psi(\mathbf{x})$ over the entire space is zero whereas the mean value of $\phi(\mathbf{x})$ is unity.

In discrete form the Haar scaling and wavelet functions can be written as $\phi = \frac{1}{n}[1\ ,1\ ,0\ ,0\ ,\cdots]$, and $\psi = \frac{1}{n}[1\ ,-1\ ,0\ ,0\ ,\cdots]$ where n is a normalizing constant.

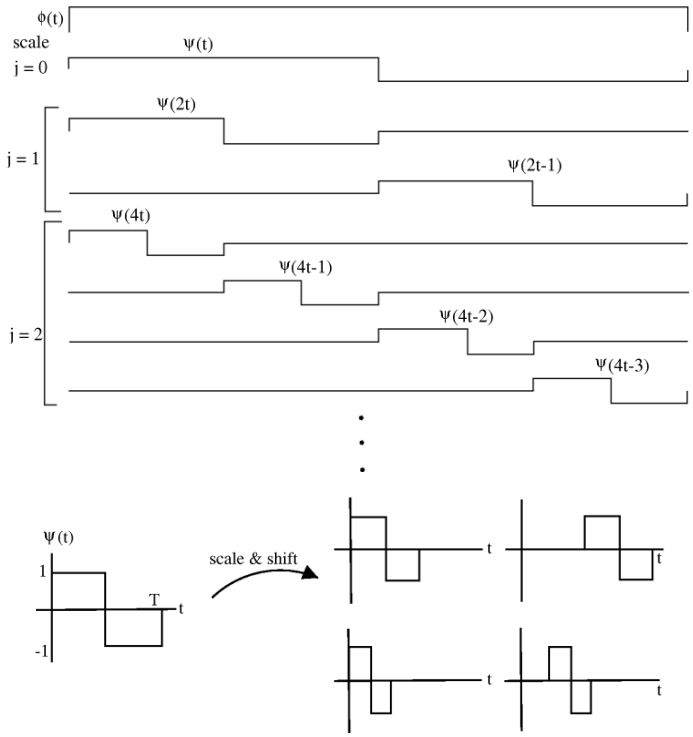

Figure 3.1: Haar scaling ϕ and wavelet ψ functions: shifting and scaling.

We shift nonzero entries of these vectors successively throughout the domain. Instead of integration, inner products will evaluate the coefficients for averages and differences.

For example, for a vector $f = [f_1\ f_2]$, the averages and differences coefficients are obtained by $< f.\phi >= \frac{f_1+f_2}{\sqrt{2}}$ and $< f.\psi >= \frac{f_1-f_2}{\sqrt{2}}$, where $\phi = [1\ 1]$ and $\psi = [1\ -1]$. This can be shown by the following matrix multiplication:

$$f^* = \mathbf{W}f,$$

where $\mathbf{W}$ is a *wavelet matrix* and contains vectors of scaling and wavelet functions, in this case: $\mathbf{W} = 1/\sqrt{2}\begin{bmatrix} 1 & 1 \\ 1 & -1 \end{bmatrix}$ and f^* is the vector containing both the averages and differences coefficients.

Properties of scaling and wavelet functions

For any scaling and wavelet function, one can define scale-controlled and shift-controlled scaling and wavelet functions by the co-called multiresolution formulation (Burrus *et al.*,

1998) or two-scale relation (Sheng, 2000):

$$\phi_{j,k}(\mathbf{x}) = 2^{j/2}\phi(2^{j/2}\mathbf{x} - k), \tag{3.3a}$$
$$\psi_{j,k}(\mathbf{x}) = 2^{j/2}\psi(2^{j/2}\mathbf{x} - k), \tag{3.3b}$$

where j represents the scale factor (or zooming) and k the translation (or shifting). Scaling and wavelet functions have the following important properties:

1. Any continuous real function can be approximated by linear combinations of $\phi(\mathbf{x})$,$\phi(2\mathbf{x})$,$\phi(4\mathbf{x})$, $\cdots$ $\phi(2^j\mathbf{x})$ and their shifted functions.

2. Orthonormality (like sines and cosines for Fourier transform) for both scaling and wavelet functions holds.

3. Wavelet/scaling functions with different scale j have a functional relationship, for Haar wavelets: $\phi(\mathbf{x}) = \phi(2\mathbf{x}) + \phi(2\mathbf{x} - 1)$ and $\psi(\mathbf{x}) = \phi(2\mathbf{x}) - \phi(2\mathbf{x} - 1)$. Therefore we can obtain the same relationships for every pair of a fine resolution, j, by adjacent translations of $2k, 2k + 1$ for a scaling and wavelet functions at coarser resolution, $j + 1$ as:

$$\phi_{j+1,k}(\mathbf{x}) = (\phi_{j,2k}(\mathbf{x}) + \phi_{j,2k+1}(\mathbf{x}))/\sqrt{2}, \tag{3.4a}$$
$$\psi_{j+1,k}(\mathbf{x}) = (\phi_{j,2k}(\mathbf{x}) - \phi_{j,2k+1}(\mathbf{x}))/\sqrt{2}, \tag{3.4b}$$

   These two formulae are very important for a hierarchical transformation. That is, by knowing any fine resolution transformation coefficients, one can calculate scaling (average) and wavelet (difference) coefficients at coarser resolution as:

$$< f, \phi_{j+1,k} > = (< f, \phi_{j,2k} > + < f, \phi_{j,2k+1} >)/\sqrt{2}, \tag{3.5a}$$
$$< f, \psi_{j+1,k} > = (< f, \phi_{j,2k} > - < f, \phi_{j,2k+1} >)/\sqrt{2}, \tag{3.5b}$$

   If the average coefficients, $< f, \phi_{j,k} >$ of f at scale j are denoted by $a_{j,k}$, and the difference coefficients $< f, \psi_{j,k} >$ are denoted by $d_{j,k}$, computing the coefficients can be represented by the *pyramid scheme* shown in Figure 3.2. The reconstruction on the other hand can also be illustrated with an *inverse pyramid scheme* shown in Figure 3.3.

   This representation shows that an original function f at an assumed fine resolution of j, can be transformed to three coarse levels of $j + 1, j + 2, j + 3$. It is possible to represent this transformation with average coefficients at the coarsest level $j + 3$ and difference (detail) coefficients at all three levels as $f_j \rightarrow a_{j+3}|d_{j+3}|d_{j+2}|d_{j+1}$.

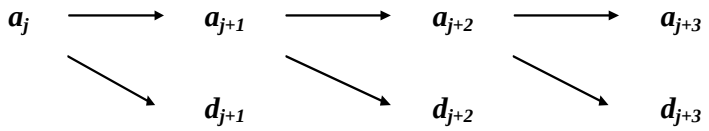

Figure 3.2: The pyramid tree for hierarchical forward transformation.

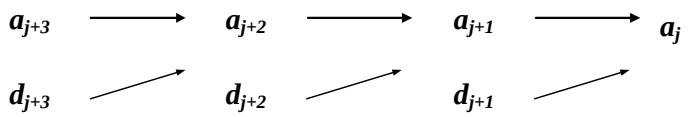

Figure 3.3: The pyramid tree for hierarchical inverse transformation.

To generalize, any function $f(\mathbf{x})$ can be expressed hierarchically in terms of scaling and wavelet functions as:

$$f(\mathbf{x}) = \sum_{k\in\mathbb{Z}} a_{J,k}\phi_{J,k}(\mathbf{x}) + \sum_{j=J}^{j_0}\sum_{k\in\mathbb{Z}} d_{j,k}\psi_{j,k}(\mathbf{x}), \tag{3.6}$$

where j_0 is the finest and $J = j_0 + n$ is the coarsest scale in the ladder of scales.

4. The main purpose for any transformation is the analysis of data. In the context of wavelets the fluctuation or differences can be interpreted as noise to get rid of. We can specify some threshold value which any noise with absolute value lower than that can be removed. In this way we can compress data into efficient averages, that is, first apply the transform, then by threshold remove the noise and finally by an inverse transform retrieve the data to a reasonable approximation.

The extension of wavelets to higher space dimensions is generally carried out by taking the tensor product of one dimensional basis functions to cover multidimensional domain of an original data. That is, we tessellate the space with new higher dimension basis functions. In two dimensions for example we have $\phi_{j,k}(\mathbf{x}) = 2^{j/2}\phi(2^j\mathbf{x} - k)$ for the x direction and $\phi'_{j,k'}(\mathbf{y}) = 2^{j/2}\phi(2^j\mathbf{y} - k')$ for the y direction. These two sets form an orthogonal basis in $L^2(R^2)$:

$$\Phi_{j,k,k'}(\mathbf{x},\mathbf{y}) = \phi_{j,k}(\mathbf{x})\phi'_{j,k'}(\mathbf{y}) = 2^{j/2}\Phi(2^j\mathbf{x} - k, 2^j\mathbf{y} - k'), k, k' \in Z$$

To obtain orthogonal wavelets we use permutation of tensor products:

$$\Psi^h_{j,k,k'}(\mathbf{x},\mathbf{y}) = \phi_{j,k}(\mathbf{x})\psi'_{j,k'}(\mathbf{y}), \tag{3.7a}$$

$$\Psi^v_{j,k,k'}(\mathbf{x},\mathbf{y}) = \psi_{j,k}(\mathbf{x})\phi'_{j,k'}(\mathbf{y}), \tag{3.7b}$$

$$\Psi^d_{j,k,k'}(\mathbf{x},\mathbf{y}) = \psi_{j,k}(\mathbf{x})\psi'_{j,k'}(\mathbf{y}), \tag{3.7c}$$

where h stands for horizontal, v for vertical, and d for diagonal. The reason is the attribution of each of these subspaces to the directions of differences: $\Psi^h_{j,k,k'}$, $\Psi^v_{j,k,k'}$, and $\Psi^d_{j,k,k'}$.

In this case, for hierarchical expansion of function $f(x,y)$ we have:

$$f(\mathbf{x},\mathbf{y}) = \sum_{k,k'\in\mathbb{Z}} a_{J,k,k'}\Phi_{J,k,k'}(\mathbf{x},\mathbf{y}) + \sum_{\mu=h,v,d}\sum_{j=J}^{j_0}\sum_{k,k'\in\mathbb{Z}} d_{j,k,k'}\Psi^\mu_{j,k,k'}(\mathbf{x},\mathbf{y}). \tag{3.8}$$

For the Haar discrete scaling and wavelet functions, one may show that:

$$\Phi = [1 \quad 1] \otimes \begin{bmatrix} 1 \\ 1 \end{bmatrix} = \begin{bmatrix} 1 & 1 \\ 1 & 1 \end{bmatrix},$$

$$\Psi^h = [1 \quad 1] \otimes \begin{bmatrix} 1 \\ -1 \end{bmatrix} = \begin{bmatrix} 1 & 1 \\ -1 & -1 \end{bmatrix},$$

$$\Psi^v = [1 \quad -1] \otimes \begin{bmatrix} 1 \\ 1 \end{bmatrix} = \begin{bmatrix} 1 & -1 \\ 1 & -1 \end{bmatrix},$$

$$\Psi^d = [1 \quad -1] \otimes \begin{bmatrix} 1 \\ -1 \end{bmatrix} = \begin{bmatrix} 1 & -1 \\ -1 & 1 \end{bmatrix},$$

where $\otimes$ is the tensor product. These arrays show the direction of calculating differences over a square. The wavelet matrix in this case can be constructed by vectorization of above functions and placing them row-wise into the matrix. For example for a 2×2 data, $f = \begin{bmatrix} f_1 & f_2 \\ f_3 & f_4 \end{bmatrix}$, one can write:

$f^* = \mathbf{W}f$, $\mathbf{W} = \frac{1}{\sqrt{2}} \begin{bmatrix} 1 & 1 & 1 & 1 \\ 1 & -1 & 1 & -1 \\ 1 & 1 & -1 & -1 \\ 1 & -1 & -1 & 1 \end{bmatrix}$, then $f^* = \frac{1}{\sqrt{2}} \begin{bmatrix} f_1+f_2+f_3+f_4 \\ f_1-f_2+f_3-f_4 \\ f_1+f_2-f_3-f_4 \\ f_1-f_2-f_3+f_4 \end{bmatrix}$.

The first row is the average coefficient and other three rows are respectively horizontal, vertical and diagonal differences coefficients.

For higher dimensions we can extend the analogy, basically we have

$\Phi = \phi(x^1)\phi(x^2)\cdots\phi(x^d)$ as the scaling function and one can show that there are $2^d - 1$ way to write different permutation of ϕ and ψ, leading to $2^d - 1$ different directions of calculating differences or in another word $2^d - 1$ wavelet basis functions. For example for three dimensional data, there are seven wavelet functions.

Hierarchical matrix representation of transforms

It is always very useful to represent inner products by matrix operations. For discrete wavelet transforms the same stands. Here, we start with Haar wavelets applied to a sample vector $f_0 = [a_{0,1}, a_{0,2}, a_{0,3}, \cdots, a_{0,8}]^T$, where the superscript T denotes transpose. The first step is to obtain averages and differences coefficients of the basis functions. This step can be described as the matrix-vector multiplication, $f_1 = \mathbf{W}_1 f_0$, where $\mathbf{W}$, is:

$$\mathbf{W}_1 = 1/n \begin{bmatrix} 1 & 1 & 0 & 0 & 0 & 0 & 0 & 0 \\ 0 & 0 & 1 & 1 & 0 & 0 & 0 & 0 \\ 0 & 0 & 0 & 0 & 1 & 1 & 0 & 0 \\ 0 & 0 & 0 & 0 & 0 & 0 & 1 & 1 \\ 1 & -1 & 0 & 0 & 0 & 0 & 0 & 0 \\ 0 & 0 & 1 & -1 & 0 & 0 & 0 & 0 \\ 0 & 0 & 0 & 0 & 1 & -1 & 0 & 0 \\ 0 & 0 & 0 & 0 & 0 & 0 & 1 & -1 \end{bmatrix},$$

where $n = \sqrt{2}$. In this matrix the first four rows applying correspond to $\phi_{j=1,k=1:4}$. The last four rows correspond to the basis vectors $\psi_{j=1,k=1:4}$. These coefficients are:

$$f_1 = \mathbf{W}_1 f_0 = 1/n \begin{bmatrix} a_{0,1} + a_{0,2} \\ a_{0,3} + a_{0,4} \\ a_{0,5} + a_{0,6} \\ a_{0,7} + a_{0,8} \\ a_{0,1} - a_{0,2} \\ a_{0,3} - a_{0,4} \\ a_{0,5} - a_{0,6} \\ a_{0,7} - a_{0,8} \end{bmatrix} = \begin{bmatrix} a_{1,1} \\ a_{1,2} \\ a_{1,3} \\ a_{1,4} \\ d_{1,1} \\ d_{1,2} \\ d_{1,3} \\ d_{1,4} \end{bmatrix}.$$

One can write f_0 in following expansion on basis of scaling and wavelet functions as: $f_0 = 1/n \left[\sum_{j,k} a_{j,k}\phi_{j,k}^T + \sum_{j,k} d_{j,k}\psi_{j,k}^T\right], j = 1, k = 1:4.$

From the orthonormality of the basis functions , $\phi_{j,k} \times \phi_{j,k'}^T = \psi_{j,k} \times \psi_{j,k'}^T = 1, \text{if } k = k'$ and $\phi_{j,k} \times \phi_{j,k'}^T = \psi_{j,k} \times \psi_{j,k'}^T = 0, \text{if } k \neq k'$, it follows that $\mathbf{W} \times \mathbf{W}^T = \mathbf{I}$, where $\mathbf{I}$ is the identity matrix. So $\mathbf{W}^T = \mathbf{W}^{-1}$.

This relation makes it possible to calculate the inverse discrete wavelet transform.

For example, the inverse transform of the above is $f_0 = (\mathbf{W}_1)^T f_1$. This relation holds for any stage and any wavelets.

To obtain the averages and differences coefficients of second stage coarsening we only work with the first four entries. This is to keep the difference coefficients of first stage and transform the average coefficients only. This stage is carried out by:

$$\mathbf{W}_2 = \begin{bmatrix} 1/n & 1/n & 0 & 0 & 0 & 0 & 0 & 0 \\ 0 & 0 & 1/n & 1/n & 0 & 0 & 0 & 0 \\ 1/n & -1/n & 0 & 0 & 0 & 0 & 0 & 0 \\ 0 & 0 & 1/n & -1/n & 0 & 0 & 0 & 0 \\ 0 & 0 & 0 & 0 & 1 & 0 & 0 & 0 \\ 0 & 0 & 0 & 0 & 0 & 1 & 0 & 0 \\ 0 & 0 & 0 & 0 & 0 & 0 & 1 & 0 \\ 0 & 0 & 0 & 0 & 0 & 0 & 0 & 1 \end{bmatrix},$$

and the transformed vector is:

$$f_2 = \mathbf{W}_2 f_1 = 1/n \begin{bmatrix} 1/n(a_{0,1} + a_{0,2} + a_{0,3} + a_{0,4}) \\ 1/n(a_{0,5} + a_{0,6} + a_{0,7} + a_{0,8}) \\ 1/n(a_{0,1} + a_{0,2} - a_{0,3} - a_{0,4}) \\ 1/n(a_{0,5} + a_{0,6} - a_{0,7} - a_{0,8}) \\ a_{0,1} - a_{0,2} \\ a_{0,3} - a_{0,4} \\ a_{0,5} - a_{0,6} \\ a_{0,7} - a_{0,8} \end{bmatrix} = \begin{bmatrix} a_{2,1} \\ a_{2,2} \\ d_{2,1} \\ d_{2,2} \\ d_{1,1} \\ d_{1,2} \\ d_{1,3} \\ d_{1,4} \end{bmatrix}.$$

This stage is rearranged as $f_2 = \mathbf{W}_2 f_1 = \mathbf{W}_2 \mathbf{W}_1 f_0$ where

$$\mathbf{W}_2\mathbf{W}_1 = \begin{bmatrix} 1/n^2 & 1/n^2 & 1/n^2 & 1/n^2 & 0 & 0 & 0 & 0 \\ 0 & 0 & 0 & 0 & 1/n^2 & 1/n^2 & 1/n^2 & 1/n^2 \\ 1/n^2 & 1/n^2 & -1/n^2 & -1/n^2 & 0 & 0 & 0 & 0 \\ 0 & 0 & 0 & 0 & 1/n^2 & 1/n^2 & -1/n^2 & -1/n^2 \\ 1/n & -1/n & 0 & 0 & 0 & 0 & 0 & 0 \\ 0 & 0 & 1/n & -1/n & 0 & 0 & 0 & 0 \\ 0 & 0 & 0 & 0 & 1/n & -1/n & 0 & 0 \\ 0 & 0 & 0 & 0 & 0 & 0 & 1/n & -1/n \end{bmatrix}.$$

This matrix holds two stages of transformation at the same time, it calculates the

coefficients of scaling functions by the first two rows corresponding to $\phi_{2,1}, \phi_{2,2}$, the third and fourth rows corresponding to $\psi_{2,1}, \psi_{2,2}$ and finally the last four rows corresponding to $\psi_{1,1}, \psi_{1,2}, \psi_{1,3}, \psi_{1,4}$. With coefficients obtained, we can write

$$f_0 = 1/n \left[\sum_{j=2,k=1:2} a_{j,k}\phi^T_{j,k} + \sum_{j=2,k=1:2} d_{j,k}\psi^T_{j,k} + \sum_{j=1,k=1:4} d_{j,k}\psi^T_{j,k} \right].$$

We can continue in a same fashion for the transformation to another coarser level:

$$\mathbf{W}_3 = \begin{bmatrix} 1/n & 1/n & 0 & 0 & 0 & 0 & 0 & 0 \\ 1/n & -1/n & 0 & 0 & 0 & 0 & 0 & 0 \\ 0 & 0 & 1 & 0 & 0 & 0 & 0 & 0 \\ 0 & 0 & 0 & 1 & 0 & 0 & 0 & 0 \\ 0 & 0 & 0 & 0 & 1 & 0 & 0 & 0 \\ 0 & 0 & 0 & 0 & 0 & 1 & 0 & 0 \\ 0 & 0 & 0 & 0 & 0 & 0 & 1 & 0 \\ 0 & 0 & 0 & 0 & 0 & 0 & 0 & 1 \end{bmatrix},$$

where and $f_3 = \mathbf{W}_3 f_2 = \mathbf{W}_3\mathbf{W}_2\mathbf{W}_1 f_0$. We have:

$$\mathbf{W}_3\mathbf{W}_2\mathbf{W}_1 = \begin{bmatrix} 1/n^3 & 1/n^3 & 1/n^3 & 1/n^3 & 1/n^3 & 1/n^3 & 1/n^3 & 1/n^3 \\ 1/n^3 & 1/n^3 & 1/n^3 & 1/n^3 & -1/n^3 & -1/n^3 & -1/n^3 & -1/n^3 \\ 1/n^2 & 1/n^2 & -1/n^2 & -1/n^2 & 0 & 0 & 0 & 0 \\ 0 & 0 & 0 & 0 & 1/n^2 & 1/n^2 & -1/n^2 & -1/n^2 \\ 1/n & -1/n & 0 & 0 & 0 & 0 & 0 & 0 \\ 0 & 0 & 1/n & -1/n & 0 & 0 & 0 & 0 \\ 0 & 0 & 0 & 0 & 1/n & -1/n & 0 & 0 \\ 0 & 0 & 0 & 0 & 0 & 0 & 1/n & -1/n \end{bmatrix}.$$

From above example, it is obvious that for any transform we can construct a *hierarchical transforming matrix*, denoted by $\mathbf{H}$, which holds some given level of coarsening ℓ as:

$$\mathbf{H}^\ell = \mathbf{W}^\ell\mathbf{W}^{\ell-1}\cdots\mathbf{W}^1. \tag{3.9}$$

It is possible to show that $\mathbf{H}$ matrices are also orthogonal matrices. The procedure for construction of $\mathbf{H}$ for higher dimensions is similar to one dimension. Only that we have to account for the multiple ways of calculating the differences as for $\mathbf{W}$ in higher dimensions.

Calculating a hierarchy of coefficients from an original dataset, we can carry out an

inverse transform. This is exactly what we exploit as an advantage of average-difference decomposition, that is, one can refine the detail coefficients through some arbitrary value for threshold and ignore insignificant details for inverse transformation. This is what is used in denoising or refining the data in signal processing and image compression.

In the next section, we will describe an upscaling procedure based on the use of **W** and **H** matrices and in Chapter 6 we will use a direct transformation on permeability fields by wavelets in order to construct non-uniform grids.

3.2 Upscaling of the Pressure Equation by Haar Wavelets

Pancaldi *et al.* (2006) illustrated the feasibility of transmissibility upscaling by means of wavelet-coarsening of the pressure equation itself, supporting the idea of operator-based upscaling of transmissibilities. They examined the ability of coarse representation of pressure equation to provide approximate solutions without the need of solving the fine problem.

The problem with their developed algorithm was computational difficulties in constructing the hierarchical matrices, undermining the computational gains in finding the approximate solution for pressure. Nonetheless, by the fundamentals provided in the previous section, we have developed a very fast and efficient algorithm to generate large hierarchical matrices for Haar scaling and wavelet functions. The algorithm is generally based on the fractal self-repetitive patterns of such matrices, therefore we extend the application of operator-coarsening to investigate possible pros and cons for this line of upscaling.

The approach starts with exploitation of the unitary matrix $\mathbf{W}^{-1} = \mathbf{W}^{\mathbf{T}}$ Equation 2.22:

$$\mathbf{TP} = \mathbf{R}, \quad \mathbf{TW}^{\mathbf{T}}\mathbf{WP} = \mathbf{R}. \tag{3.10}$$

To complete the equation transformation, we multiply by $\mathbf{W}$ on both sides to obtain a new transmissibility matrix and a new boundary condition vector applied to the transformed pressure:

$$\left(\mathbf{WTW}^{\mathbf{T}}\right)\mathbf{WP} = \mathbf{WR}. \tag{3.11}$$

Defining the transformed variables,

$$\mathbf{T}' = \mathbf{WTW}^{\mathbf{T}}, \tag{3.12a}$$

$$\mathbf{P}' = \mathbf{WP} = \begin{bmatrix} \mathbf{P}_a \\ \mathbf{P}_d \end{bmatrix} \tag{3.12b}$$

$$\mathbf{R}' = \mathbf{WR} = \begin{bmatrix} \mathbf{R}_a \\ \mathbf{R}_d \end{bmatrix}. \tag{3.12c}$$

where $\mathbf{P}_a$ and $\mathbf{R}_a$ are average coefficients of the transformed pressure and right-hand-side vector and $\mathbf{P}_d$ and $\mathbf{R}_d$ are difference coefficients. From there equations we have:

$$\mathbf{T}'\mathbf{P}' = \mathbf{R}'. \tag{3.13}$$

Up to this point, the transformation has been completely reversible; in fact, we have simply changed the variables with which we represent the system. Now we approximate

Equation 3.13 by ignoring the fluctuations of the system to preserve the large scale behaviour.

To illustrate the mechanism, let us consider a $1 \times N$ system, with $N = 4$, that we want to coarsen by a factor $n = 2$ by transforming a 1×4 group of cells into a 1×2 group of blocks. To approximate Equation 3.13, we define new variables $\boldsymbol{P}$ and $\boldsymbol{R}$, composed of the first $(N/2) = 2$ elements of $\mathbf{P}'$ and $\mathbf{R}'$ respectively, and $\boldsymbol{T}$ as the $(N/2) \times (N/2)$ upper left corner of $\mathbf{T}'$.

If we assume unit viscosity, unit block sizes and areas, and constant pressure at two boundaries, the fine-scale, the transformed and the coarse-scale transmissibilities ($\mathbf{T}, \mathbf{T}'$and$T$) are:

$$\mathbf{T} = \begin{bmatrix} 2k_1 + t_{12} & -t_{12} & 0 & 0 \\ -t_{12} & t_{12} + t_{23} & -t_{23} & 0 \\ 0 & -t_{23} & t_{23} + t_{34} & -t_{34} \\ 0 & 0 & -t_{34} & t_{34} + 2k_4 \end{bmatrix},$$

$$\mathbf{T}' = \begin{bmatrix} 2k_1 + t_{23} & -t_{23} & 2k_1 - t_{23} & -t_{23} \\ -t_{23} & t_{23} + 2k_4 & t_{23} & t_{23} - 2k_4 \\ 2k_1 - t_{23} & t_{23} & 2k_1 + t_{23} + 4t_{12} & t_{23} \\ -t_{23} & t_{23} - 2k_4 & t_{23} & 4t_{34} + 2k_4 + t_{23} \end{bmatrix},$$

$$\mathbf{T}' = \begin{bmatrix} \mathbf{A} & \mathbf{B} \\ \mathbf{B}^T & \mathbf{C} \end{bmatrix}; \tag{3.14a}$$

$$\boldsymbol{T} = \mathbf{A} = \begin{bmatrix} 2t_1 + t_{23} & -t_{23} \\ -t_{23} & t_{23} + 2t_4 \end{bmatrix}. \tag{3.14b}$$

where t_{ij} is the transmissibility between cells i and j.

To determine the coarse pressure, we invert the renormalized transmissibility matrix $\boldsymbol{T}$ solving for pressure. In the mean-field approximation we can write:

$$\boldsymbol{TP} = \boldsymbol{R}, \tag{3.15}$$

$$\boldsymbol{P} = \boldsymbol{T}^{-1}\boldsymbol{R}. \tag{3.16}$$

Using $\boldsymbol{T}$, $\boldsymbol{P}$, and $\boldsymbol{R}$ corresponds to assuming that fluctuations of pressures are negligible. In other words, we represent the system in a mean-field approximation where only the average behaviour is considered. Hence, exploiting the orthonormal property of $\mathbf{W}$, an expression for the coarse transmissibility can be derived operating on Darcy's equation on the fine–scale, leading to a mean-field pressure solution. The general principle

underlying this method can be applied in any dimension and to all problems which require coarsening.

It would be interesting to find what effect the terms that we have just discarded have on the pressure solution. This can be attempted in one dimension by retaining the full $\mathbf{T}'$ matrix in Equation 3.14a and solving simultaneous equations in $\mathbf{P}_a$ and $\mathbf{P}_d$, eliminating $\mathbf{P}_d$ leads to:

$$\left(\mathbf{A} - \mathbf{B}\mathbf{C}^{-1}\mathbf{B}^T\right)\mathbf{P}_a = (\mathbf{R}_a - \mathbf{B}\mathbf{C}^{-1}\mathbf{R}_d). \tag{3.17}$$

This looks like a new equation of the type $\mathbf{T}''\mathbf{P}_a = \mathbf{R}''$. This form suggests methods to solve for pressure solution beyond the mean-field approximation and has also led to developments of wavelet-based multigrid solvers (see De Leon, 2008). The main problem here is to calculate $\mathbf{C}^{-1}$ in an efficient way. Application of wavelets, however, proves to have an advantage because of the sparsity of this matrix. One can also impose thresholds in $\mathbf{C}^{-1}$ and add non-zero entries. This approach leads to a truncated multigrid method. Another application of the above formulation is in wavelet-based homogenization procedure (see Dorobantu & Engquist, 1998). For our upscaling purposes, however, in the following, only the mean-field approximation will be considered, where $\mathbf{B}$ and $\mathbf{C}$ are set to zero.

Explicit formula for wavelet upscaled permeability and transmissibilities

The above formalism can be used to derive an explicit formula for renormalization group upscaling of transmissibilities and permeabilities by wavelets. This requires a small collection of cells to be replaced successively. In Pancaldi (2007), a 4×4 system is selected to be replaced by 2×2 system. The fine-scale transmissibility matrix in this case is 16×16. When transformed with $\mathbf{W}$ and $\mathbf{W}^{\mathbf{T}}$, the matrix obtained is still 16×16, but taking the first four rows and columns only, we get a 4×4 matrix. This can be compared to the transmissibility matrix of a 2×2 system to deduce the relation between the permeabilities at cell and block level.

Consider the transmissibility matrix $\mathbf{T}$ for a 4×4 system with flow from left to right and no flow top and bottom:

$$\mathbf{T} = \begin{bmatrix} 2k_1 + t_{12} + t_{15} & -t_{12} & 0 & 0 & -t_{15} & 0 & ... & 0 \\ -t_{21} & 2k_2 + t_{23} + t_{25} & -t_{23} & 0 & 0 & -t_{25} & ... & 0 \\ \cdots & \cdots & \cdots & \cdots & \cdots & \cdots & \cdots & -t_{1516} \\ 0 & 0 & 0 & 0 & 0 & \ldots & -t_{16,15} & 2k_{16} + t_{1615} + t_{1612} \end{bmatrix},$$

where t_{ij} is the transmissibility between cells i and j, and k_i is the permeability of cell i.

The upper corner $\boldsymbol{T}$ of the transformed matrix $\mathbf{T}' = \mathbf{WTW}^{\mathbf{T}}$:

$$\boldsymbol{T} = \begin{bmatrix} k_1 + k_2 + \frac{t_{23}+t_{67}}{2} + \frac{t_{59}+t_{610}}{2} & -\frac{t_{23}+t_{67}}{2} & -\frac{t_{59}+t_{610}}{2} & 0 \\ -\frac{t_{23}+t_{67}}{2} & k_3 + k_4 + \frac{t_{23}+t_{67}}{2} + \frac{t_{711}+t_{812}}{2} & 0 & -\frac{t_{711}+t_{812}}{2} \\ -\frac{t_{59}+t_{610}}{2} & 0 & k_{13} + k_{14} + \frac{t_{59}+t_{610}}{2} + \frac{t_{1011}+t_{1415}}{2} & -\frac{t_{1011}+t_{1415}}{2} \\ 0 & -\frac{t_{711}+t_{812}}{2} & -\frac{t_{1011}+t_{1415}}{2} & k_{15} + k_{16} + \frac{t_{711}+t_{812}}{2} + \frac{t_{1011}+t_{1415}}{2} \end{bmatrix}.$$

The transmissibility matrix for a 2×2 system, $\mathbf{T_{2\times 2}}$ is:

$$\mathbf{T_{2\times 2}} = \begin{bmatrix} 2k_1' + t_{12}' + t_{13}' & -t_{12}' & -t_{13}' & 0 \\ -t_{21}' & 2k_2' + t_{21}' + t_{24}' & 0 & -t_{24}' \\ -t_{13}' & 0 & 2k_3' + t_{31}' + t_{34}' & -t_{34}' \\ 0 & -t_{24}' & -t_{34}' & 2k_4' + t_{24}' + t_{34}' \end{bmatrix}.$$

We can now compare the elements of the two matrices one by one, $\mathbf{T}_{2\times 2}[i,j]$ and $\boldsymbol{T}[i,j]$. For example:

$$\begin{aligned} \mathbf{T}_{2\times 2}[1,2] &= -t_{12}', \\ \boldsymbol{T}[1,2] &= -\frac{t_{23}+t_{67}}{2}, \\ \mathbf{T}_{2\times 2}[1,3] &= -t_{13}', \\ \boldsymbol{T}[1,3] &= -\frac{t_{59}+t_{610}}{2}, \\ \mathbf{T}_{2\times 2}[1,1] &= 2k_1' + t_{12}' + t_{13}', \\ \boldsymbol{T}[1,1] &= k_1 + k_2 + \frac{t_{23}+t_{67}}{2} + \frac{t_{59}+t_{610}}{2}, \end{aligned}$$

and hence, for consistency:

$$t_{12}' = \frac{t_{23}+t_{67}}{2}, \tag{3.19a}$$

$$t_{13}' = \frac{t_{59}+t_{610}}{2}, \tag{3.19b}$$

$$k_1' = \frac{k_1+k_2}{2}. \tag{3.19c}$$

This identification of the correspondence of terms from fine–scale to coarse–scale is only possible because the structure of the upper left block in the transform of the matrix at the fine–scale is the same as the structure of the matrix for the smaller system. This means that, provided we discard the pressure fluctuations, the operator acting on the coarse–scale is still Darcy's law but with different values for permeability. To illustrate this Figure 3.4 shows how an original transmissibility matrix is transformed in the two-dimensional case.

The relationship between permeability and transmissibility in the upscaled system

$(k'_i,\, t'_{ij})$ and in the fine–scale system $(k_i,\, t_{ij})$ is shown in Figure 3.5. For a 4×4 system, the block permeability is the average of the permeability of the cells which are in direct contact with the boundary condition. The block transmissibilities are the average of the cell transmissibilities across faces.

The dependence of the coarse values on the type of boundary condition is evident. If this method were applied in this form to a large system most of the information apart from the values at the boundaries would be lost. To avoid losing too much information at each upscaling step the procedure is always performed on a 4×4 subset of fine–scale cells.

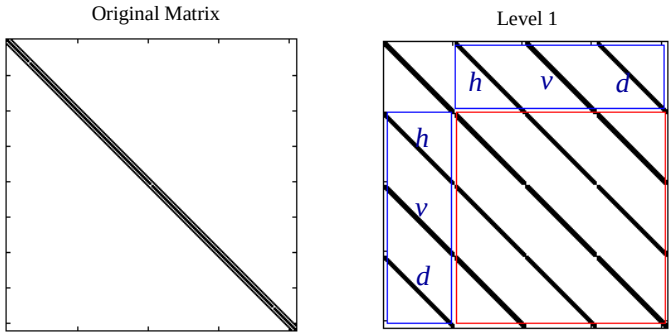

Figure 3.4: A transformation of transmissibility matrix. Left: original fine-scale matrix for a 32×32 system, $\mathbf{T}$, right: $\mathbf{T}' = \mathbf{WTW}^{\mathbf{T}}$. The red box represents $\mathbf{C}$, and blue boxes are $\mathbf{B}$ and $\mathbf{B}^{\mathbf{T}}$. The top left corner is $\boldsymbol{T}$. It is interesting to notice that $\mathbf{B}$ and $\mathbf{C}$ matrices each include bands of horizontal, vertical and diagonal differences.

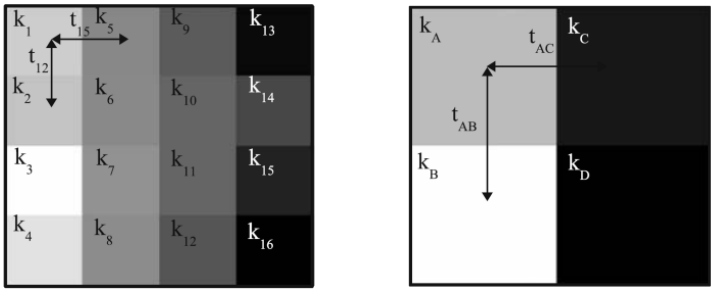

Figure 3.5: A schematic representation of the relation between cell and block permeabilities and transmissibilities. Left: fine-scale permeabilities and right: coarse-scale permeabilities and transmissibilities (Pancaldi *et al.*, 2006).

Hierarchical transformation and multilevel wavelet upscaling

The application of wavelets described above was a single level upscaling and led to derivation of an explicit formula for the upscaled properties. The role of boundary conditions is clear in any attempt to derive a formula (Pancaldi, 2007). In another format of wavelet upscaling, Pancaldi *et al.* (2009) applied the hierarchical transformation (with the aid of **H**-matrices) to the pressure equation. This format will lead to higher than one level of upscaling but offers no explicit formula. Further, the effects of boundary conditions in the right-hand-side vector are transformed and upscaled in a similar multilevel fashion.

To illustrate this approach to operator upscaling, assume a one-dimensional system. In Figure 3.6, the sparsity pattern of the original transmissibility matrix and three levels of upscaled operators are shown. It is interesting to notice that the pattern of sparsity for transformed matrix follows the same ladder of transformation as Equation 3.6. That is, we have an averaging operator corresponding to the coarsest level on the top left, and a ladder of differencing operators for the finest to coarsest levels.

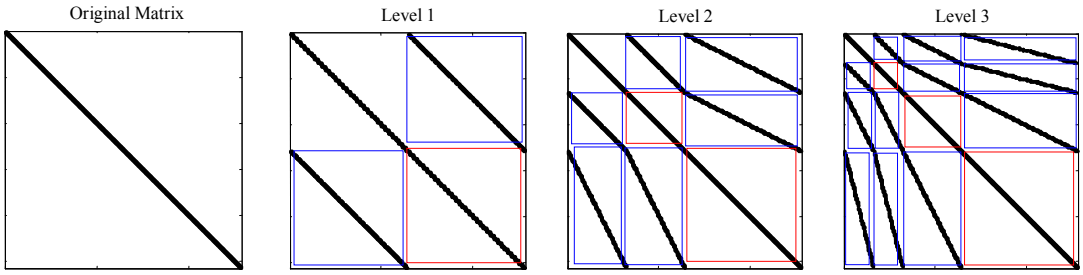

Figure 3.6: Three levels of multiscale projection of transmissibility matrix of a one-dimensional $N_x = 256$ system. The red boxes show $\mathbf{C}$ submatrices while blue boxes are $\mathbf{B}$ and $\mathbf{B}^{\mathbf{T}}$.

Again equivalent to the application of **W**-matrices, the averaging operator has a similar sparsity pattern to the original matrix. Hence, one can extract the coarse transmissibilities from bands of the $\boldsymbol{T}$ matrix and use it for the upscaled model.

Moreover, there are suggestions in Pancaldi *et al.* (2009) about how to extend the method to nonuniform coarsening. The algorithm, however, is an *a posteriori* procedure in determining the coarse grain within which the pressure distribution is governed by the global boundary conditions (again a constant pressure gradient). For such coarse grids, the coarse operator produces satisfactory solution. However in very heterogeneous coarse grids in which subgrid effects can not be ignored, the case is different and we have to use an operator which includes submatrices that give the differences. In this case we need to predict where or at what scales the deviation of pressure from the

homogeneous case will be more severe, so that we can arbitrarily choose to keep only the corresponding elements in the calculation of the new solution. This leads to savings in computational time, because the matrix that needs to be inverted is reduced in size as rows and columns not required for the solution are deleted.

The solution for $\mathbf{P_d}$ is then integrated with the previously determined average values, $\mathbf{P_a}$, to give a nonuniformly coarse grained solution (Pancaldi *et al.*, 2009). Nonetheless for making an *a priori* algorithm, authors have practiced strategies to decide the position of coarse gridcells where elements should be kept. This led to taking the permeability gradients as an indicator of heterogeneities. However in this reference Pancaldi *et al.* (2009) the discussions are limited only to the calculation of the pressure in a single time step for problems with a constant pressure gradient boundary condition. Further, there is no study on the effects of upscaling on the saturation equation and final outputs of a simulation. Also it is questionable whether the pressure solution can actually cover dynamic evolution of saturation throughout the simulation.

Regarding the above problems, in the next section for comparison studies we completely ignore the differencing submatrices in $\mathbf{T}'$. Nevertheless significant numerical improvements in constructing $\mathbf{H}$-matrices have been implemented in upscaling. We took advantage by looking at the sparsity pattern of such matrices so that for large systems the construction, multiplication and reduction in obtaining $\boldsymbol{T}$ should be efficient.

Multiphase flow upscaling by wavelets

A multiphase application of the wavelet upscaling technique was used in Pancaldi (2007) to preserve the average pressure of a chosen phase while reducing the number of grid cells in the system. The structure of the algorithm is identical to the single phase case, the only difference being that instead of absolute permeability we now have total mobility values for each cell.

The algorithm is to extract upscaled transmissibilities from fine values based on the formalism presented in Equations 3.11 and 3.12 applied to the multiphase version of the pressure equation (Equation 2.13). This leads to an upscaling rule for total mobility which is the same as the averaging scheme for absolute permeability. Using this rule we do not need to perform any matrix operations to obtain the coarse–scale mobility values. Once these values are known, the pressure of the reference phase can be calculated at the coarse–scale.

There are also considerations about the coarse representation of capillary pressure and gravity. The direct approach is to include these effects on the right hand side vector and consequently upscale them by extracting $\boldsymbol{R}$ from either $\mathbf{R}' = \mathbf{WR}$ or $\mathbf{R}' = \mathbf{HR}$.

The important factor here is updating the upscaled transmissibilities and that needs an efficient algorithm in extracting $\boldsymbol{T}$ from either $\mathbf{T}' = \mathbf{WTW^T}$ or $\mathbf{T}' = \mathbf{HTH^T}$. This also requires fine–scale total mobility values to update $\mathbf{T}$. One approach is to transfer the coarse pressure solution onto the fine grid by way of linear weighted interpolation. Then a fine–scale flux is calculated to be used for the fine–scale transport equation solution.

In the next section we will assess the quality of multiphase wavelet upscaling.

3.3 Numerical Results for Wavelet Upscaling

In this section we compare the wavelet method described in the previous section with a selection of upscaling methods. We perform comparisons for single phase and multiphase flow in the following subsections.

3.3.1 Single Phase Flow

First we start with the checkerboard pattern for upscaling. In this case we are able to assess permeability wavelet upscaling with an exact solution for upscaled permeability of the medium. The next case is a synthetic realization of heterogeneity and the final case is a realistic example of heterogeneity viewed as a benchmark in the reservoir simulation community.

The checkerboard pattern

One of the most difficult cases of heterogeneity for upscaling and simulation is a case with large contrast in permeabilities of fine cells. For the simplest case of high contrast, one test is to consider the checkerboard configurations shown in Figure 3.7. In the analysis of renormalization, King (1996) examined the two configurations, case **a** and case **b**, with permeability ratio 1000:1 between the high permeability (k_1) cells and the low permeability (k_2) cells.

While case **a** has a large contrast, it does not have great implications for upscaling as flow occurs almost entirely in the high permeability cells and the interface between these cells are connected by a finite difference scheme. Therefore, the upscaled permeability obtained by pressure solver method is a reliable value and can be looked at as a reference solution.

In contrast, for case **b**, the finite difference solution has problems at interface. The flow path between large permeability cells are not compatible with the two point flux approximation scheme's assumption that fluid flows from the centre of one cell to the centre of the adjacent cell. The upscaled permeability, on the other hand, for the case of constant pressure gradient in one direction, is exact and has been proved to be the geometric mean of permeabilities while we have a uniform checkerboard configuration with equal distribution of phases k_1 and k_2 (Yeo & Zimmerman, 2001; Farmer, 2002; Matheron, 1967). Hence, we assume systems with configurations in Figure 3.7 with $k_1 = 1000, k_2 = 1$ and upscale them to a single value.

In Table 3.1 we have compared the values obtained by different methods for *upscaled permeability*. For this special case of boundary condition, as obtained by Equation 3.19, the wavelet-based upscaled permeability is equal to the arithmetic mean. For case **a**, the

Method	case (a) in Figure 3.7	case (b) in Figure 3.7
Geometric Mean	177	**31**
Pressure Solver Method	**534**	2.66
Harmonic Arithmetic Mean	667	500
Arithmetic Harmonic Mean	501	2.00
Modified Harmonic Arithmetic Mean	534	2.66
Modified Arithmetic Harmonic Mean	501	2.66
Renormalization Method	534	2.66
Wavelet Method	500	500

Table 3.1: The results for checkerboard pattern simulations. The reference solutions are bold-faced.

value obtained by wavelet method is close to the reference value obtained by pressure solver method. In contrast, for case **b**, the value obtained by wavelet method is an order of magnitude different from the reference value obtained by geometric mean. This is not far from expectation as wavelet method is based on coarsening an operator discretized by two point flux approximation scheme. The table also shows that correction for modified harmonic arithmetic mean and modified arithmetic harmonic mean has brought these means very close to pressure solver and renormalization method.

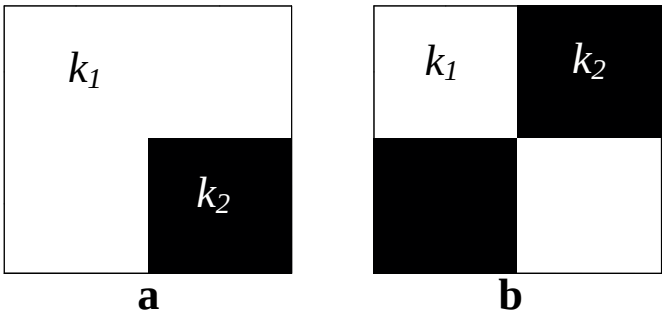

Figure 3.7: Checkerboard patterns used in comparison studies.

For the case of transmissibility upscaling, we compare the reference and upscaled values for outflux. The system is originally 32×32 dridcells populated by configuration of case **a**. We impose a constant pressure gradient in the x direction and upscale the system to 4×4 coarse grid cells. Further, in this case, we are able to add adaptive local global transmissibility upscaling to the list of methods compared. We note that for case **b**, the finite difference fine solution is not reliable for comparison. In the simulation here

we impose *passive tracer flow* assumptions. In passive tracer flow, we have an injected fluid which has the same properties as the initial fluid in place and there is no reaction or absorption. This is equivalent to using a linear flow function $f(S)$ for a waterflooding and a viscosity ratio of $M = \mu_w/\mu_o = 1$ and relative permeability curves as:

$$k_{rw} = S \quad \text{and} \quad k_{ro} = 1 - S, \tag{3.20}$$

where S is the saturation of injected tracer (here water). These assumptions provide a constant the total mobility and constant $\mathbf{k}\lambda_t$ throughout the simulation. Consequently the upscaling is a single phase upscaling.

The error for total outflux is measured by:

$$\epsilon_r = \frac{\|Q^c - Q^f\|}{Q^f} \tag{3.21}$$

where Q^f and Q^c are the total outflow in fine and coarse scales respectively. By a single time step calculation of total outflux from the system, the relative error for different methods are $\epsilon_{r,PSM} = 0.50\%$, $\epsilon_{r,ALG} = 0.01\%$ and $\epsilon_{r,wavelet} = 6.10\%$.

The outflux of the initial fluid in-place computed by different methods is shown in Figure 3.8. It can be seen observed that wavelet transmissibility upscaling by hierarchical transformation overestimated the flow. Two methods of pressure solver and adaptive local global upscaling match the result of the fine scale solution. However due to the inherent error of coarse representation of saturation, there is a considerable diffusion error affecting the production after breakthrough. Reducing the numerical diffusion error will be our objective in Chapter 4.

Correlated log-normal permeability realizations

Here, we consider upscaling of correlated log-normal fields for permeability. In generating log-normal permeabilities, the values of mean and standard deviation of underlying random normal distribution with which the correlated model is built, can represent the degree of heterogeneity of the system. For each of these statistical properties (mean and standard deviation), 50 realizations of size 256×256 are simulated by using the *moving average technique*. The algorithm is described in detail in Wallstrom *et al.* (1999b) and later in Pancaldi (2007). The spatial correlation lengths are the same in both directions. The value is 10 grid cells equivalent to a dimensionless value of $10/256 = 0.0391$. Table 3.2 shows the statistical properties of the realizations and Figure 3.9 shows permeability fields of one random realization for the first considered set.

The permeabilities obtained are allocated to the centres of a 256×256 Cartesian system of a unit area with uniform gridding. Then a constant pressure gradient is

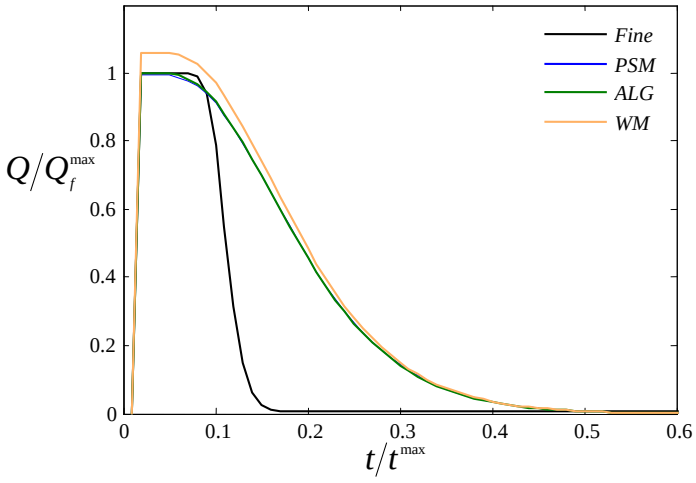

Figure 3.8: The outflux of fluid in-place in tracer flow computed by different upscaling method and the fine reference solution.

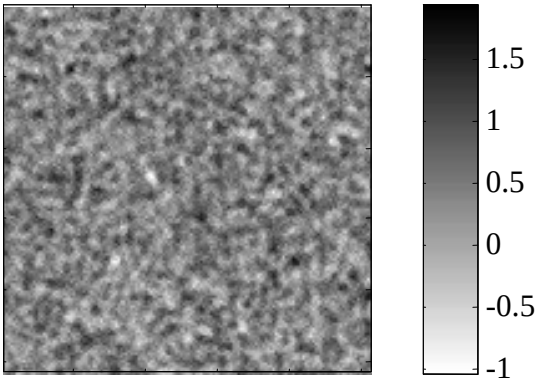

Figure 3.9: The logarithm of permeability for a random realization for the sets $\sigma = 5$.

μ	σ	$< \ln k_{min} >$	$< \ln k_{max} >$	$\ln < M >$	$\ln < S >$
1	5	-3.54	5.75	1.59	2.12
1	10	-8.03	10.4	3.33	5.18
1	15	-9.10	11.6	3.86	5.86
1	20	-12.4	15.2	6.28	9.79

Table 3.2: Statistical properties of of correlated log-normal distributions used for calculation of outflow in fine and coarse models. μ and σ are the mean and standard deviation of uncorrelated random normal distributions that are used as background for correlated field. M and S are the mean and standard deviation of correlated fields.

imposed on each realization in the x direction and fine and different coarse outflows are calculated. The coarse models contain 32×32 grid cells corresponding to an upscaling factor of 8×8 or three levels of hierarchical coarsening.

Figure 3.10 shows the relative error in outflux computed by Equation 3.21 for three methods of pressure solver, adaptive local global and wavelet. Here, we do not show the results of renormalization method, modified harmonic arithmetic mean and modified arithmetic harmonic mean, because they essentially produce almost identical results compared to pressure solver method even when there is more than one level of upscaling. It is observed that wavelet hierarchical transmissibility upscaling has performed poorly compared to pressure solver method. On the other hand, corrections of transmissibilities by adaptive local global algorithm by means of 3 iterations, have effectively reduced ϵ_r.

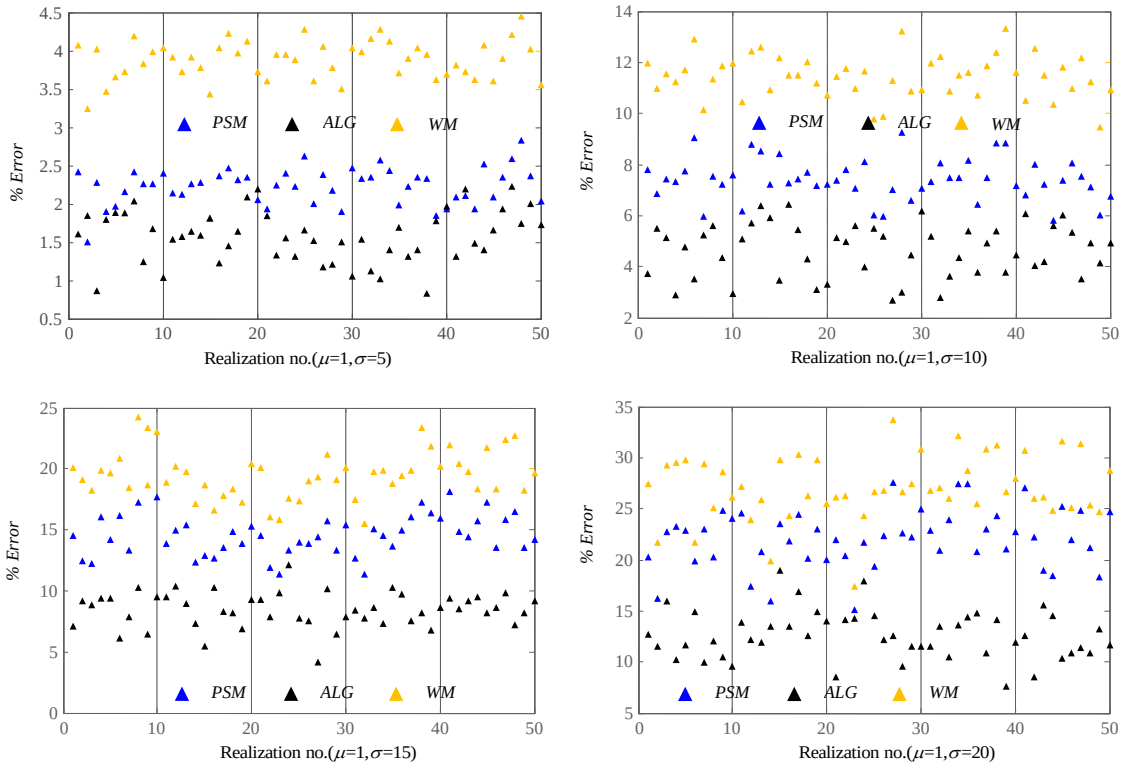

Figure 3.10: The relative error in outflows in four sets of 50 realizations of porous media.

Tenth SPE comparative solution project, model 2

Now we repeat the constant pressure gradient, single-phase flow on a sequence of two-dimensional models with permeability data from Model 2 of the 10th SPE Comparative Solution Project (Christie & Blunt, 2001), henceforth simply referred to as *the SPE10 model*. This model consists of $60 \times 220 \times 85$ cells, each of size $20 \times 10 \times 2ft$. The top 35 layers represent a prograding near-shore environment, with quite smooth variation in the coefficients from one grid cell to the next. The bottom 50 layers model a fluvial formation with narrow high-flow channels. Long correlation length structures, such as the high-flow non-local channels in the lower part of the SPE10 model, are generally difficult to model using conventional upscaling methods (Kippe *et al.*, 2008).

In order to carry out hierarchical upscaling, we first extrapolated the permeabilities of the layers from 60×220 to 64×256, hence we were able to upscale the model to 8×32 coarse system. The extrapolations are performed with the help of MATLAB built-in programme `interp2`. This function determines the output by a "bicubic interpolation" within the two-dimensional input function, which in our case is the permeability in 60×220 layout.

A pressure gradient as in previous examples was applied in the x direction with no flow from the other sides. We plot the fine outflow against the coarse outflows in all 85 layers in Figure 3.11, and as we observe, there is an improvement by adaptive local global upscaling. The arithmetic harmonic mean, renormalization method and pressure solver method, all underestimated the of flow ($Q^c < Q^f$). Harmonic arithmetic mean on the other hand overestimated the flows but are much closer to the 45^o line. The results obtained by modified harmonic arithmetic and arithmetic harmonic have not been plotted due to their proximity to the results of the pressure solver method. The wavelet method performs very poorly for most of the bottom heterogeneous layers and it yields overestimated results that are just better than arithmetic mean which gives a large overestimation.

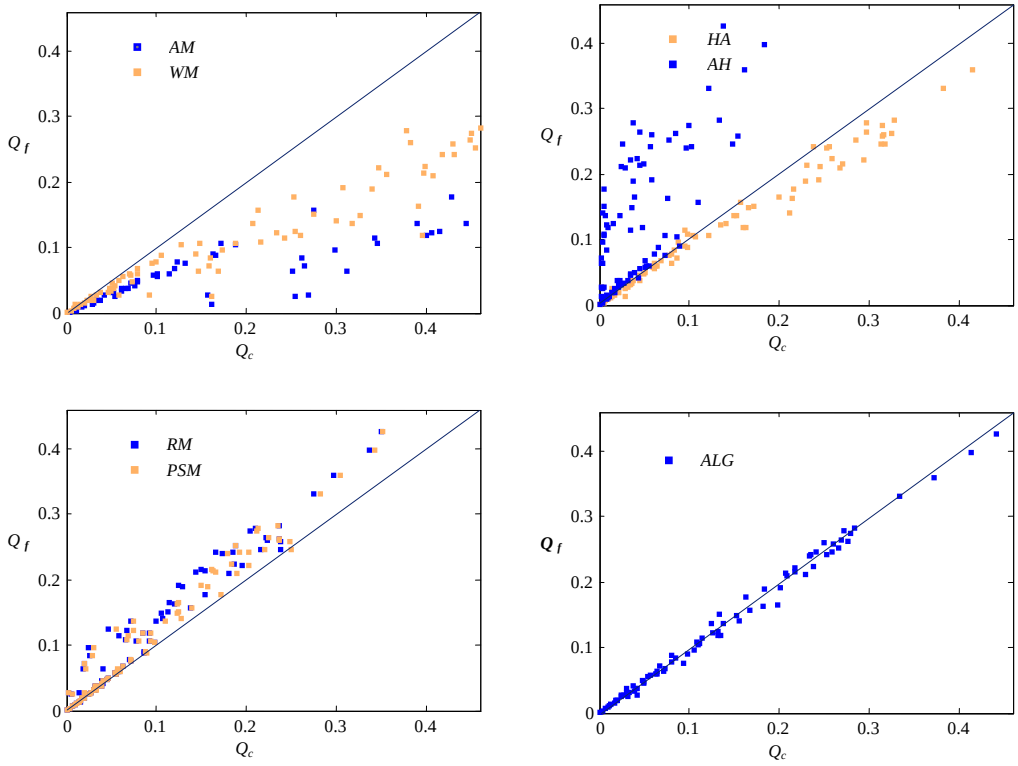

Figure 3.11: Fine scale compared to the coarse scale results for SPE10 layers, the closer the marks to the 45^o line, the more accurate results for upscaling.

3.3.2 Multiphase Flow

Here, for multiphase water flooding we assume a reservoir initially saturated with oil. Water is injected to displace the oil with similar boundary condition as for single phase tracer flow simulation. The only difference is relative permeabilities:

$$k_{rw} = S^2 \quad \text{and} \quad k_{ro} = (1 - S)^2, \tag{3.22}$$

where S is the water saturation. Also we used unit viscosity values for both oil and water. Two permeability fields (**a** and **b**) were taken as 32×32 subsets from SPE10 model shown in Figure 3.12.

A constant pressure gradient was imposed on the boundaries in the x direction and similar outflux calculation as for previous examples were performed and results for the outflux of oil were shown in Figure 3.13. For the adaptive local global transmissibility upscaling we used a 3-iteration limit. The figure shows strong overestimation of flow by wavelet method, strong underestimation of flow by pressure solver method and marginal underestimation of flow by adaptive local global.

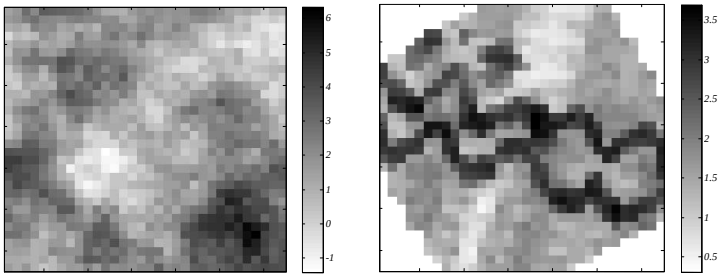

Figure 3.12: The logarithm of 32×32 subset permeability fields (left **a**, and right **b**) from SPE10 model.

3.3.3 Summary of Results

In our numerical experiments we observed that the results for wavelet upscaling of either permeability or transmissibility, are not reasonable. In fact the transformation operator can be seen as simple averaging that produces a mean-field approximation and consequently the results are found to be only just better than simple arithmetic mean. However, there should be improvements in performance if one can include the details ignored by coarse operator. This would amount to implementing a multigrid method and the cost of calculation of an enriched coarse operator and its application can negate

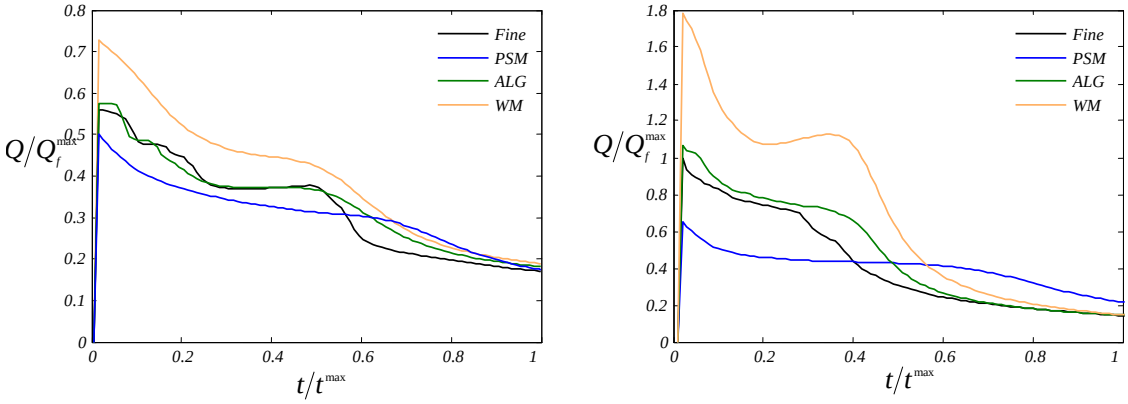

Figure 3.13: The outflux of fluid in-place in multiphase flow computed by different upscaling methods and the fine reference solution for media **a**, left and **b**, right.

the advantage gained by upscaling. To this end, we were not able to devise an efficient yet high-performance coarse wavelet operator. Hence, we turned our attention towards the investigation and possible improvements of adaptive local global upscaling in the following chapters.

4 Multiscale and Upscaling-Downscaling

In this chapter, we will describe an upscaling-downscaling method and show an application of its use. We will introduce some modifications and improvements to an existing upscaling-downscaling technique and will compare its performance with a multiscale method and conventional upscaling method. The purpose of developing upscaling-downscaling and multiscale methods is to resolve the solutions of either the pressure or the saturation equation, or both the equations, to avoid the problem of conventional upscaling that averages out the detailed complexities of flow. The key issue remains to keep such methods efficient and computationally viable.

The chapter is laid out as follows, In Section 4.1 we describe two of the most important and widely cited multiscale methods. The first one (multiscale finite volume method) resembles to the upscaling-downscaling technique in refining the coarse velocity. The second one (multiscale mixed finite element method) will be used for comparison. In Section 4.2 the modified upscaling-downscaling technique as the main achievement of this work will be presented. Finally in Section 4.3 the results for a wide range of test cases will be given.

4.1 Multiscale Methods

4.1.1 Multiscale Finite Volume Method (MSFV)

This method uses linear superposition of local solutions of pressure and velocity as basis functions and was first suggested by Jenny *et al.* (2003). The coarse scale solution is used as weights in superpositions to provide mass-conservative fine fluxes at the fine scale. Consequently, the fine fluxes can be used to solve transport equation at the fine scale to reduce numerical diffusion error. The fact that the method is a finite volume scheme means that instead of two-point flux approximation scheme, a multipoint flux approximation scheme is used to derive transmissibilities and to discretize the pressure equation. Here, we describe procedures for the calculation of basis functions for pressure and velocity.

The pressure basis functions

The derivation of pressure basis functions is a localization of the pressure equation to regions such R shown in Figure 4.1. For each such region (henceforth referred to as interaction region), we solve a set of homogeneous boundary-value problems of the form:

$$-\nabla \cdot \mathbf{K}\lambda\nabla\Theta_i^k = 0 \ \text{ in } \ R, \ \ \Theta_i^k = \nu_i^k, \ \text{ on } \ \partial R, \tag{4.1}$$

where ν_i^k are boundary conditions to be specified below. The subscript i in Θ_i^k denotes a coarse point in the coarse grid $\mathscr{T}_H$. The superscript k runs over all corner points of the region. The above set of equations provide local solutions for each region. The global solution of pressure, then, is obtained by linear superposition:

$$p = \sum_k p^k \Theta^k = \sum_{i,k} p^k \Theta_i^k, \tag{4.2}$$

where p^k is a given set of pressure values at $\mathscr{T}_H$ and Θ_i^k will serve as building blocks to construct a global continuous pressure solution. The boundary condition for Equation 4.1, ν_i^k satisfies $\nu_i^k(x^l) = \delta_{kl}$, where δ_{kl} is the Kronecker delta function. For boundaries over the edges one approach is to use linear interpolation to extend the coarse point values $\nu_i^k(x^l)$ to provide a linear pressure distribution.

The role of boundary condition is very crucial to mimic the fine scale behaviour. Wallstrom *et al.* (1999a) found that a constant pressure condition of the sub-domain boundary tends to overestimate flow contributions from high permeability areas. Instead Hou & Wu (1997) proposed a so-called oscillatory boundary condition so that for each

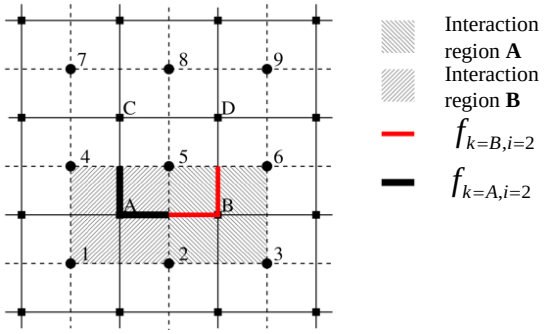

Figure 4.1: Coarse gridblock $i = 5$ with nine adjacent coarse volumes (solid lines). Also shown are two interaction regions $k = A, B$ around coarse gridblock and their flow contribution on this block (Jenny *et al.*, 2005).

face F (a line in 2D) of the interaction region, we solve:

$$-\partial_x(\mathbf{K}\lambda\partial_x\nu_i^k) = 0 \ \text{ in } \ F, \tag{4.3}$$

where x denotes the component parallel to the boundary. The possible oscillations in values of $\mathbf{K}$ render such boundary conditions oscillatory. This choice is reported to lead to uniform flow along the boundary and better results than a constant or linear pressure condition (Hou & Wu, 1997). By assembling the flux contributions across the grid block boundaries, a multi-point finite volume stencil is derived:

$$\begin{aligned}\sum_k p^k f_{k,i} &= \int_{E_i} q dx, \\ f_{k,i} &= -\int_{\partial_{E_i}} \mathbf{n}\cdot\mathbf{K}\lambda\nabla\Theta^k ds,\end{aligned} \tag{4.4}$$

where $f^{k,l}$ is the total flux out of grid block E_i induced by Θ^k and are in fact the effective transmissibilities for a 9-point stencil of the multipoint flux approximation in 2D.

The velocity basis functions

For the velocity reconstruction, a set of secondary basis functions is defined. For each pressure basis function Θ^k, one associates a reconstruction basis function $\tilde{\Theta}^k$ with each cell in the coarse mesh. This is achieved by computing the fine scale flux q from the global pressure field. This is used in turn as a boundary condition to solve an elliptic

equation for coarse grid block E_i:

$$\nabla \cdot \mathbf{K}\lambda\nabla p = f' \text{ on } E_i, \quad f' = \frac{\int_{\partial E_i} q d\Gamma}{\int_{E_i} dE_i}. \tag{4.5}$$

In two dimensions, each coarse grid block is overlapped by four interaction regions, so for determination of q for a coarse grid block (for example the coarse grid block $i = 5$ in Figure 4.1), we have to insert $p_i = 1, \{i = 1 : 9\}$ and use the relevant pressure basis function to have q alongside the faces of the coarse grid block $i = 5$. This means that for the 2D case, we have to solve 9 equations of the form of Equation 4.5 for each coarse grid block to cover all possible contributions of the surrounding coarse blocks and their constituent interaction regions. The fine scale velocity field is obtained by linear superposition of these 9 solutions with weights being again the coarse pressure values at $\{i = 1 : 9\}$. In 3D the number of solutions for linear superposition is 27.

The calculation and definition of two sets of pressure and velocity basis functions are now complete at the initial time. One can restore these functions to use them throughout the simulation. However, when the total mobility is not constant as in multiphase flow, the solution of local problems and consequently the transmissibilities and the velocity basis functions undergo changes that should be accounted for in regions of dynamic change. This can be implemented both temporally and spatially, in an adaptive way as in Jenny *et al.* (2005).

The high number of velocity basis functions for reconstruction may become an undermining factor in efficiency of the algorithm. Alternatively, Jenny *et al.* (2006) suggested the use of an algorithm that does away with the use of a secondary set of basis functions. This algorithm will be used in this work under the framework of upscaling-downscaling technique and will be described in more detail later.

4.1.2 Multiscale Mixed Finite Element Method (MSMFE)

The main idea behind the mixed finite element method is to consider both the pressure and the velocity as unknowns and express them in terms of basis functions (Aarnes, 2004). This is unlike the finite volume or the finite difference method where the velocities are derived from the pressure solution. For each variable (pressure and velocity), different approximation spaces are considered. Hence, the continuity equation ($\nabla \cdot \mathbf{v} = Q$) and the Darcy equation ($\mathbf{v} = -\mathbf{K}\nabla p$) are approximated by finite element functions for pressure and velocity, respectively, belonging to their pertinent spaces.

The common choice of the approximation spaces for the pressure is piecewise-constant scalar for the element areas and for the velocity is piecewise-linear over the element interfaces. The mathematical details and the discrete forms of the equations in the

mixed finite element method are fully described in many references like Aarnes (2004).

The multiscale generalization is to design a multiscale approximation space for the velocity that accounts for the subgrid variations in permeability. This is achieved by letting the interface-associated basis function be numerical simulations of local pressure equations restricted to a pair of coarse grid blocks with source terms specified in such a way that unit flow is forced across the element interface (Hou & Wu, 1997). Specifically, if E_i and E_j denote two coarse gridblocks with a common interface $\Gamma_{ij} = \partial E_i \cap \partial E_j$, the multiscale velocity basis functions Ξ_{ij} are defined by use of pressure local basis function, Θ_{ij}, as:

$$\Xi_{ij} = -\mathbf{K}\lambda\nabla\Theta_{ij}, \quad \text{in} \quad E_i \cup E_j, \tag{4.6}$$

$$(\nabla \cdot \Xi_{ij})|_{E_i} = \ell(x) / \int_{E_i} \ell(x)dx, \quad (\nabla \cdot \Xi_{ij})|_{E_j} = -\ell(x) / \int_{E_j} \ell(x)dx, \tag{4.7}$$

with no-flow boundary conditions along the edges $\partial E_i \cup \Gamma_{ij} \cup \partial E_j$. The choice of specification of $\ell(x)$ is important to ensure mass conservation in the coarse mesh. To model the flow around the wells more accurately on the subgrid, Aarnes (2004) and Aarnes *et al.* (2006) proposed the use of $\ell(x) = 1$ away from the wells and $\ell(x) = Q$ in gridblocks penetrated by wells. The definition of $\ell(x)$ completes the definition of the multiscale velocity basis functions Ξ_{ij}. The solutions for Equation 4.6 are time-dependent since they depend on the total mobility of the underlying grid. Therefore we need to regenerate them adaptively in time and space similar to multiscale finite volume method. We will use a multiscale mixed finite element method for the comparison purposes in the results section with the upscaling-downscaling method that will be described in the next section.

4.2 Upscaling-Downscaling Methods

In this approach we solve for the pressure distribution in the upscaled grid and include the fine-scale heterogeneities in the computation of the phase saturations. In other words we solve the saturation is a grid nested inside the coarse grid, hence the name, *nested gridding*. Other common terminology used is simulation on a *dual-mesh* framework. The result of performing this procedure, is similar to the multiscale methods in that the saturation equation is solved in the fine scale grid.

The dual mesh method was first used by Ramé & Killough (1992) to model a single-phase miscible flow. They used a finite element method to solve the pressure field on the coarse scale. This solution is then projected by a spline interpolation procedure to the fine grid. A finite difference scheme was used for the saturation equation that was solved on the fine grid. Meanwhile, a restriction operation is performed periodically to rescale the coefficient matrix for the discretized pressure equation on the coarse grid. This operation will inform the coarse grid about the total mobility changes occurring at fine grid.

To avoid the artifacts of a non-physical interpolation, Guérillot & Verdière (1995) introduced a dual-mesh method where the velocity field was reconstructed within each coarse-grid block by solving the pressure using approximate boundary conditions. For the boundary conditions Gautier *et al.* (1999) assumed constant fine fluxes across each coarse face, while Chen *et al.* (2003), Audigane & Blunt (2004) and Niessner & Helmig (2009) used fine-scale inter-block transmissibility.

4.2.1 Incompressible Flow with no Capillarity-Gravity

The description of nested gridding from Gautier *et al.* (1999) is as follows. First we decouple the pressure problem into a set of smaller problems on two scales: we consider a coarse grid superimposed on a fine grid. We assume that the initial petrophysical properties are defined on the fine grid. The first step of the nested gridding method is to upscale porosity and permeability on the coarse scale. Any method of upscaling at this stage can be used. The pressure equation is solved on the coarse scale. The next step is to go back to the fine grid, solving a set of "velocity reconstruction" local problems within each coarse grid block using boundary conditions derived from the previous step.

As shown in Figure 4.2, the main equation for reconstructing velocity in each coarse gridblock, E_j, is:

$$\begin{aligned} \mathbf{v}_{E_j} &= -\mathbf{K}_{E_j}\nabla p, \quad \nabla.\mathbf{v}_{E_j} = q \;\; in \;\; E_j, \\ \mathbf{v}_{E_j}\cdot\mathbf{n}|_\Gamma &= q^c_\Gamma.\frac{t_{\gamma i}}{\sum_{\gamma i\subset\Gamma} t_{\gamma i}} \;\; on \;\; \partial E_j, \end{aligned} \tag{4.8}$$

where $\mathbf{v}_{E_j}$ is the total velocity field for the coarse gridblock, E_j; q_Γ^c is the coarse scale flux across the coarse edge, Γ, calculated from the upscaling stage, and $t_{\gamma i}$ is the fine-scale transmissibility of interface, $\gamma_i \subset \Gamma$. We have N_c (coarse gridblocks) such equations to solve. A global reconstructed velocity field is obtained simply by union of the patches of velocities:

$$\mathbf{v}^{rec} = \bigcup_{j=1}^{Nc} \mathbf{v}_{E_j} \quad in \quad \Omega. \tag{4.9}$$

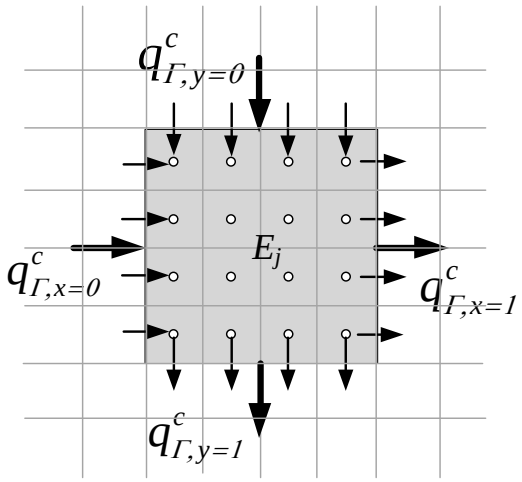

Figure 4.2: An illustration of downscaling: distributing coarse scale velocity values (bigger arrows) into fine scale velocities (smaller arrows) as Neumann boundary condition

We note that the technique described above is used instead of the application of the velocity basis functions in the framework of later version of multiscale finite volume method (Jenny *et al.*, 2006) to reconstruct the fine velocities.

4.2.2 Modified Static Downscaling

In the following, we will describe some modifications to improve accuracy and efficiency of the downscaling procedure. These modifications constitute our main contributions to the upscaling-downscaling field.

The first modification comes with the vector $t_{\gamma i}/(\sum_{\gamma i \subset \Gamma} t_{\gamma i})$ in Equation 4.8 that is in fact a partitioning vector for attributing a higher share of coarse flow to high permeability boundary fine cells and similarly a lower share to less permeable cells. This proportionality is purely local and would be wrong when a high permeable single fine cell is unconnected to high flow paths. To enhance the proportionality, we try to use a better partitioning vector. Hence, we change the proportion to $|v_{\gamma_i}|/(\sum_{\gamma i \subset \Gamma} |v_{\gamma_i}|)$,

where v_{γ_i} is the fine scale velocity over interface γ_i. This change obviously requires the original fine velocity distribution. As an approximate alternative, we use distributions obtained by solving for extended local problems in the local-global upscaling stage. These solutions provide velocity fields over the extended region to detect a better picture for connection of flow paths than that provided by the use of the transmissibilities. The indices for prolongation can be easily calculated once for an incompressible case in the first iteration of local-global upscaling. In this case, we change Equation 4.8 to:

$$\begin{aligned} \mathbf{v}_{E_j} &= -\mathbf{K}_{E_j}\nabla p, \quad \nabla\cdot\mathbf{v}_{E_j} = q \;\; in \;\; E_j, \\ \mathbf{v}_{E_j}\cdot\mathbf{n}|_{\Gamma} &= q^c_{\Gamma}.\frac{|v^{app.}_{\gamma_i}|}{\sum_{\gamma i\subset\Gamma}|v^{app.}_{\gamma_i}|} \;\; on \;\; \partial E_j, \end{aligned} \tag{4.10}$$

where $\mathbf{v}^{app.} = \{v^{app.}_{\gamma_i}\}$ represents an approximated velocity field from local-global upscaling stage.

The second suggestion is to improve the computational efficiency. This is achieved by elimination of the constraint to reconstruct the fine pressure distribution. In Gautier *et al.* (1999) the central fine grid block is assumed known and equal to the pressure of the coarse gridblock. The specification of pressure in this technique is necessary to make Equation 4.8 solvable. However, in our experience, the reconstructed pressure field contains several peculiarities and is not of a comparable quality to the fine reference model.

If we neglect the emphasis on having a fine scale pressure distribution, instead we can try to reconstruct only a mass conservative velocity field. This allows us to decompose the problem into four equations in two dimensions (as shown in Figure 4.3) and six in three dimensions (number of coarse edges) plus particular solutions for wells. The solvability is this case is achieved by an arbitrarily fixing the pressure in one cell, e.g. equating the pressure of the first cell to the pressure of the coarse gridblock l ($p_1 = P_c$). The pressure solution, in this fashion, is non-physical but its gradient provides useful velocity distributions.

For each decomposed equation we impose Neumann boundary conditions, derived from partitioning of a unit-value coarse scale flux over the corresponding coarse edge. For example for a coarse gridblock, E, we compute a distribution function denoted by $\mathbf{v}_{\Gamma i}$ for edge $\Gamma i \subset \partial E$, obtained by boundary condition assumed as $\mathbf{v}_{\Gamma i}.\mathbf{n}|_{\Gamma i} = 1 \times \left(|v^{app.}_{\gamma_i}|/\sum_{\gamma i\subset\Gamma}|v^{app.}_{\gamma_i}|\right)$ on Γ_i and open flow over the other edges. Henceforth, we refer to these distributions as basis functions.

After calculating the distribution basis functions, we can generate the same velocity distribution of Equation 4.9 by means of a linear superposition for coarse gridblocks

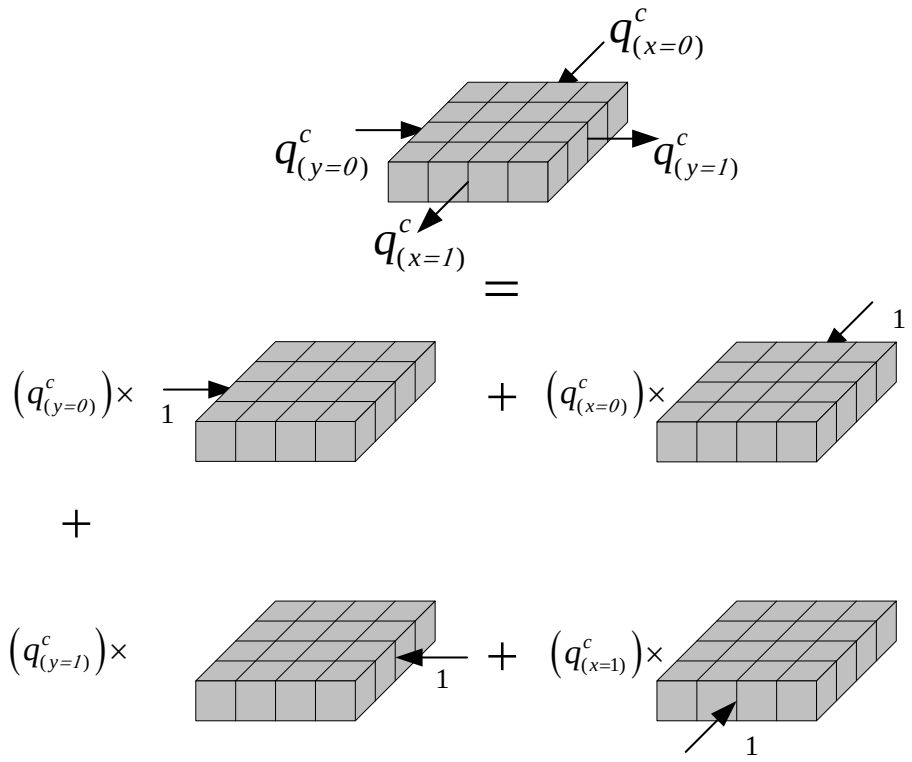

Figure 4.3: Illustration of the decomposition of nested-gridding problem in two-dimensions into four equations that determine velocity distribution basis functions.

and a union for the global domain:

$$\mathbf{v}^{\text{rec}} = \bigcup_{j=1}^{Nc} \left(\sum_{i=1}^{M} q_{\Gamma i}^{c} . \mathbf{v}_{\Gamma i} \right)_{j} + \mathbf{v}_{p}, \quad in \ \ \Omega, \tag{4.11}$$

where Nc is number of coarse gridblocks, M is space dimension, $q_{\Gamma i}^{c}$ is coarse velocity over coarse edge, $\Gamma i \subset \partial E$, and $\mathbf{v}_p$ is a particular solution only for well coarse gridblocks calculated as:

$$\mathbf{v}_p = -\mathbf{K}_E \nabla p, \quad \nabla \cdot \mathbf{v}_p = q. \quad on \quad E_{well}. \tag{4.12}$$

The calculation of $\mathbf{v}_{\Gamma i}$ and $\mathbf{v}_p$ are performed only for the initial time step so that the downscaling does not require the solution of Equation 4.8 for the rest of the simulation, furthermore, such calculations are obviously parallelizable. These factors can be exploited for computational gains. Moreover, aiming only at constructing a conservative velocity field, different global boundary conditions can be simply incorporated into this framework. The schematic of application of this technique is given in Figure 4.4.

The step by step description of our upscaling-static-downscaling (adaptive local global upscaling coupled by static modified nested gridding or ALG-MNG–) is as follows:

1. Determine the size of the coarse grid blocks.

2. At initial time $t = 0$, two procedures are performed: Firstly, the upscaled transmissibilities $\mathbf{T}^*$ are calculated for all coarse grid block edges by adaptive local global upscaling. The procedure is as follows: First for a single phase flow, we calculate upscaled transmissibilities by extended local method. This procedure is performed by assuming an extended region around the coarse grid block with the target coarse edge that we are trying to calculated the upscaled transmissibilities for. The size of extended regions for our tests will be the target coarse grid block plus half of the length of the neighbouring coarse gridblocks. The bigger the size, the better the global features will be incorporated into local upscaling, however with the expense of higher computations.

   Then we run the model with the upscaled values to determine coarse pressures in the coarse grid block centres. Now we perform the iterative procedure of adaptive local global method described in Section 2.2 to correct the upscaled transmissibilities. The iterations continue until values of the transmissibilities no longer change. We save the upscaled transmissibilities ($\{\mathbf{T}^*\}$).

3. Secondly, the velocity basis functions are calculated for each coarse grid block by Equation 4.10 and for wells by Equation 4.12. For better quality basis functions in partitioning of coarse fluxes into boundaries of Equation 4.10, we use approximate

velocity fields obtained in extended regions in the stage of adaptive local global upscaling. These velocities come form pressure solved at the extended regions similar to what is shown in Figure 2.5, grey square, with boundary conditions from bilinear or trilinear interpolation of coarse pressure values. We save the basis functions ($\{v_{\Gamma i}\}$) and we refer to them as *static* basis functions because they are calculated at initial time.

4. Here we start the actual simulation. First by upscaled transmissibilities, $\mathbf{T}^*$, we calculate implicitly, from the pressure equation, the coarse pressure and the coarse fluxes.

5. Then the coarse fluxes are processed by static downscaling to have a reconstructed fine scale velocity field (v^{rec}) by Equation 4.11.

6. The fine scale fluxes are input into the upstream explicit saturation solver and one time step is run. We have now the fine scale saturation solution.

7. The saturation solution is used to calculate the total mobilities.

8. If we have a single phase tracer flow simulation, the total mobilities are constant, otherwise, we detect regions with high change of the total mobilities via Equation 2.40 in order to update the upscaled transmissibilities of coarse blocks located in such regions.

9. In the detected regions the permeability at fine scale is multiplied by the total mobilities and with the new mobility-included permeability we update upscaled transmissibilities. This is done by a single-stage use of the coarse pressure as Dirichlet-type boundary condition for solving pressure at extended local problems. The solution is used for new transmissibilities calculated from Equation 2.39.

10. We go back to step 3, for the second time step of the coarse scale pressure calculation.

The use of the basis functions to reconstruct fine scale distributions has also been examined in the context of multiscale finite volume method and multiscale mixed finite element method. In the multiscale finite volume method (Jenny *et al.*, 2003) the *pressure basis functions* are used to derive effective upscaled transmissibilities. For fine scale velocity reconstruction, this algorithm uses 9 local problems (in 2D) and 27 local problems (in 3D) to construct and store a secondary set of functions as velocity basis functions. Also, in multiscale mixed finite element method (Aarnes, 2004) an additional set of basis functions for velocity are considered in addition to the usual basis functions

for pressure considered in conventional finite element methods. The role of these basis functions is similarly to incorporate the effect of total mobility change and underlying subgrid heterogeneities.

Applying a static velocity field (obtained only at the initial time), Aarnes & Efendiev (2006) used homogenization theory to prove that under some assumptions, the two-phase flow velocity, can be approximated by a static part that does not depend on saturation, times a time dependent function in each coarse block. Also Khoozan *et al.* (2011) replaced the time-consuming reconstruction step in the dual mesh method with a fast analytical solution. However, in deriving the analytical solution, the subgrid heterogeneity of each coarse gridblock is replaced with a homogeneous upscaled value. This can be an undermining factor. Instead we use a numerical solution for deriving the static part of the velocity field at fine scale and we use the coarse velocity field as weights to compute the global reconstructed velocity field. In the results section, we will apply and compare this algorithm with the fine reference model for different cases of flow simulation and various heterogeneous media and boundary conditions.

4.2.3 Developing Frameworks for Inclusion of Capillarity-Gravity and Compressibility

Capillarity and gravity

The addition of capillarity and gravity requires extra measures in upscaling-downscaling. These two additional effects can undermine the robustness of static downscaling, because the velocity field undergoes changes from time to time due to the evolution of saturation. Here, we implement a simple *operator splitting* procedure to separate the effects of capillarity and gravity from viscous force. The splitting allows us to still use the velocity reconstruction basis functions for the viscous effects. The operator splitting, following references like Bratvedt *et al.* (1996) and Lie *et al.* (2012), uses Equation 2.13 to obtain:

$$-\nabla \cdot \left[\mathbf{K}\lambda_t \nabla p_o^{visc}\right] = Q_t, \tag{4.13}$$

$$-\nabla \cdot \left[\mathbf{K}\lambda_t \nabla p_o^{cap-grav}\right] = -\lambda_w(S)\mathbf{K}\nabla P_{cwo} + \lambda_G(S) g \mathbf{K}\nabla z, \tag{4.14}$$

$$p_o = p_o^{visc} + p_o^{cap-grav}. \tag{4.15}$$

The first equation determines the velocity in the absence of capillarity and gravity. The second equation determines the velocity including these effects. The treatment of these two equations for the upscaling-downscaling is different. First, for the upscaling stage, we perform the adaptive local global iteration and transmissibility updating only for the first equation (Equation 4.13). Then we use the transmissibilities for the coarse scale capillarity-gravity equation (Equation 4.14). Due to the existence of a

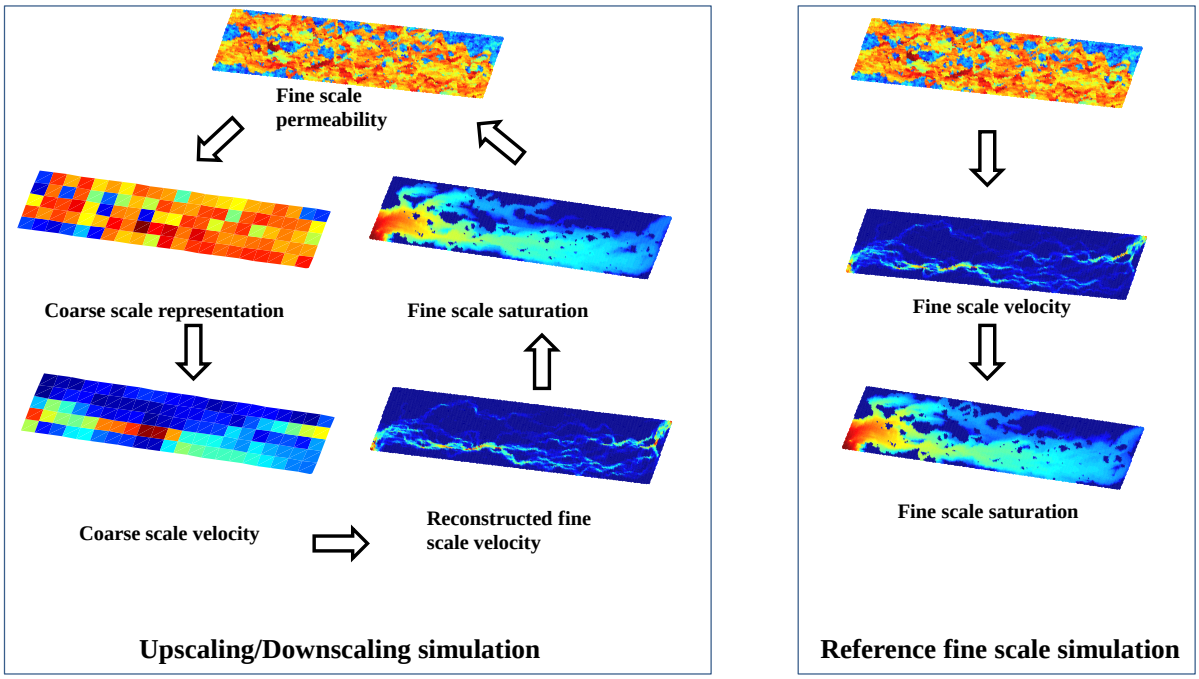

Figure 4.4: Switching the scales via upscaling-downscaling algorithm compared with the reference algorithm used in the numerical section.

non-constant right hand side in the second equation, the reconstruction procedure for this equation should be revised. That is because velocities arising from capillarity and gravity may change more frequently, we have to use a secondary set of velocity-reconstruction basis functions that are updated frequently throughout the simulation. These basis functions are calculated by static downscaling again. The coarse fluxes obtained form solution of the second equation are used as weights. Then depending on level of dominance of gravity or capillarity, every several time steps, the basis functions should be recalculated.

Compressibility

The compressibility of rock and fluids complicates the algorithm of upscaling-downscaling mainly because the rock porosity and fluid densities are often strong functions of pressure and consequently the pressure equation should be solved iteratively. The intrinsic requirement of iteration in this case, however, justifies the use of ALG transmissibility correction in the same iteration loop of the pressure equation solution.

Here, we present the fine scale equations and suggest the upscaling-downscaling formalism, extending static downscaling to the compressible case. The purpose is to separate effects of compressibility from an incompressible case in order to be able to handle the compressibility-induced velocities adaptively. Starting from the mass balance equation for a compressible phase l:

$$\frac{\varphi^{n+1}\rho_l^{n+1}S_l^{n+1}-\varphi^{n}\rho_l^{n}S_l^{n}}{\Delta t}-\nabla\cdot\left(\rho_l^{n+1}\lambda_l\cdot(\nabla p^{n+1}-\rho_l^{n+1}g\nabla z)\right)=Q_l, \tag{4.16}$$

taking the sum over all phases l resulting in:

$$\frac{\varphi^{n+1}}{\Delta t}-\frac{\varphi^{n}}{\Delta t}\sum_l B_l^{n+1}\rho_l^{n}S_l^{n}-\sum_l B_l^{n+1}\nabla\cdot\left(\rho_l^{n+1}\lambda_l\cdot(\nabla p^{n+1}-\rho_l^{n+1}g\nabla z)\right)=Q_t, \tag{4.17}$$

where $B_l=1/\rho_l$ is the volume formation factor. Linearization of this equation results in the iterative linear pressure equation:

$$\begin{aligned}\frac{C}{\Delta t}(p^{\nu+1}-p^{\nu})-\sum_l B_l^{\nu}\nabla\cdot(\rho_l^{\nu}\lambda_l\cdot\nabla p^{\nu+1}) = &-\frac{\varphi^{\nu}}{\Delta t}\\ &+\frac{\varphi^{n}}{\Delta t}\sum_l B_l^{\nu}\rho_l^{\nu}S_l^{\nu}+Q_t\\ &-\sum_l B_l^{\nu}\nabla\cdot\left((\rho_l^{\nu})^2\lambda_l g\cdot\Delta z\right),\end{aligned} \tag{4.18}$$

which converges to Equation 4.17 as $\nu\to\infty$. The superscripts ν and $\nu+1$ denote

quantities at the old and new iteration levels, respectively, and

$$C = \frac{\partial \varphi}{\partial p}\bigg|^{\nu} - \varphi^{n} \sum_{l} \frac{\partial B_l}{\partial p}\bigg|^{\nu} \rho_l^n S_l^n, \tag{4.19}$$

is the compressibility coefficient. Based on Hajibeygi & Jenny (2009), the convective term can be modified as:

$$\sum_{l} B_l^{\nu} \nabla \cdot (\rho_l^{\nu} \lambda_l \cdot \nabla p^{\nu+1}) \approx \nabla \cdot (\lambda_t \cdot \nabla p^{\nu+1}) - \nabla \cdot (\lambda_t \cdot \nabla p^{\nu}) + \sum_{l} B_l^{\nu} \nabla \cdot (\rho_l^{\nu} \lambda_l \cdot \nabla p^{\nu}). \tag{4.20}$$

Finally, the convergent iterative scheme for the fine scale compressible pressure equation is:

$$\frac{C}{\Delta t}(p^{\nu+1} - p^{\nu}) - \nabla \cdot (\lambda_t \cdot \nabla p^{\nu+1}) = RHS^{\nu} + Q_t, \tag{4.21}$$

where

$$\begin{aligned} RHS^{\nu} = &-\frac{\varphi^{\nu}}{\Delta t} + \frac{\varphi^{n}}{\Delta t} \sum_{l} B_l^{\nu} \rho_l^{\nu} S_l^{\nu} - \sum_{l} B_l^{\nu} \nabla \cdot \left((\rho_l^{\nu})^2 \lambda_l g \cdot \Delta z \right) \\ &- \nabla \cdot (\lambda_t \cdot \nabla p^{\nu}) + \sum_{l} B_l^{\nu} \nabla \cdot (\rho_l^{\nu} \lambda_l \cdot \nabla p^{\nu}). \end{aligned} \tag{4.22}$$

For the upscaling-downscaling, the above equation is split at the coarse scale:

$$\left(\frac{C}{\Delta t} \mathbf{I} - \mathbf{T}^{*} \right) p^{inc.} = Q_t, \tag{4.23}$$

$$\left(\frac{C}{\Delta t} \mathbf{I} - \mathbf{T}^{*} \right) p^{cmp.} = (RHS^{\nu} + \frac{C}{\Delta t} p^{\nu}), \tag{4.24}$$

where $\mathbf{I}$ is the identity matrix and $\mathbf{T}^{*}$ is the matrix populated with transmissibilities obtained by adaptive local global upscaling. $p^{inc.}$ and $p^{cmp.}$ are incompressible and compressible pressure solutions. By this decomposition we bound the iterations to the compressible component only. Following the convergence on the second equation, the velocity field from the first equation can be downscaled as before by only the difference of having to add $C/\Delta t$. We note that $\mathbf{T}^{*}$ in this formalism is, similar to the incompressible case, calculated initially globally and updated after then adaptively. As argued in Hajibeygi & Jenny (2009), the values of C will not affect the solution of the first equation, because on convergence of the second equation, the first term on the left-hand side of Equation 4.21 cancels out.

The downscaling of the velocity induced by the compressible part, is not straightforward due to the existence of a pressure-dependent right-hand-side part. In this case similar to gravity-induced velocity we have to employ the conventional nested gridding

or design a downscaling procedure that its functions are frequently updated.

4.3 Numerical Results, Comparisons and Discussions

In this section we compare the algorithms defined in the previous section with different boundary conditions and different heterogeneous media. For boundary conditions we assume a quarter five-spot pattern as well as flow induced by constant injection rate on one end and constant pressure at the other end.

Two cases are considered in the following subsections. The first one is a passive tracer (linear) flow simulation in which the fluids act as a single phase flow specification. The second scenario is an incompressible waterflood. For each scenario, a range of combinations of upscaling and downscaling methods are compared with each other. The description and denotation of these techniques are given in Table 4.1.

Table 4.1: Upscaling-downscaling methods used in comparison study.

Method	Description
PSM-NG	Conventional nested-gridding on pressure solver method
PSM-MNG	Modified nested-gridding on pressure solver method
ALG-NG	Conventional nested-gridding on adaptive local-global upscaling in single phase
ALG-MNG−	Static (with application of basis function) modified nested-gridding on adaptive local-global upscaling in multiphase
ALG-MNG+	Dynamic (without application of basis functions) modified nested-gridding on adaptive local-global upscaling in multiphase

For the assessment of each model, a comparison to the fine scale reference solution is performed. The following error measures are considered:

1. The saturation error (Hauge *et al.*, 2012):

$$\zeta(s_{\text{rec}}) = \frac{\|s_{\text{rec}}(.,t) - s_{\text{ref}}(.,t)\|_2}{\|s_{\text{ref}}(.,t)\|_2}, \quad \delta(s_{\text{rec}}) = \frac{1}{T}\int_0^T \zeta(s_{\text{rec}})dt, \tag{4.25}$$

   where s_{ref}, or s, is the saturation calculated from reconstructed velocity field of the model under consideration and s_{ref} is the saturation from the fine scale reference model. Further, t is time measured in pore-volumes injected (PVI) and T is the final simulation time. Finally $\|\cdot\|_2$ represents Euclidean norm or L^2 norm.

2. The reconstructed velocity error (Kippe *et al.*, 2008):

$$\delta(v_{rec}) = \frac{\left\|v_x - v_x^{\text{ref}}\right\|_2}{\left\|v_x^{\text{ref}}\right\|_2} + \frac{\left\|v_y - v_y^{\text{ref}}\right\|_2}{\left\|v_y^{\text{ref}}\right\|_2}, \tag{4.26}$$

where v_x and v_y are reconstructed velocity components in x and y directions and v^{ref} is the fine scale reference velocity field. This error illustrates the quality of reconstructed velocity and indirectly examines the accuracy of the coarse velocity of certain model used in the downscaling procedure.

3. The water cut versus PVI obtained from each model. Water cut is measured by the fraction of the water mobility divided by the total mobility. In the case of constant total mobility this fraction is equal to the water saturation of producing cell. The value is in any case (tracer or multiphase flow) a function of the single cell's saturation. Clearly, these values are local in contrast to the previous global norms. Furthermore, we have to note that, for all the methods, the water cut values are obtained based on the fine scale saturation results.

4. In addition to water cut, similar to Castellini (2001) and He (2005), we consider comparison of $Q_o/\Delta P$ curves, where $Q_o = wc\lambda_o(S)(P_j - P_{bh})$ is the oil flow rate measured at the production gridblock, wc is the well constant, P_j is the pressure of the production grid block, P_{bh} is the bottom-hole pressure and $\Delta P = P_i - P_j$ is the pressure difference between the injection and production grid blocks. This quantity is considered to assess the upscaling quality in terms of pressure in addition to flow rate. This quantity is calculated only at the production cell. For the coarse-scale pressure error estimation, we will use:

$$\delta(P^c, P^f, t) = \frac{\left\|P^f(.,t) - P^c(.,t)\right\|_{L^2}}{\|P^f(.,t)\|_{L^2}}, \tag{4.27}$$

where P^c is coarse pressure from various upscaling methods and P^f is volume-averaged pressure from fine scale reference method.

4.3.1 Tracer Flow

Here, the upscaling is for single phase flow. Hence, the static and dynamic downscaling are identical schemes, and the comparison is limited to the use of $\mathbf{v}^{app.}$ only, or in other words improvements by using modified nested gridding compared to conventional nested gridding.

For boundary conditions we assume a source and a sink respectively in the top left and bottom right corners of layers 10, 37, 47 and 68 of SPE10 model. Layers 37, 47 and 68 are highly channelized and heterogeneous where the permeability in the system undergoes a wide variation from 0.004 to 20,000 millidarcy. Layer 10 is a non-channelized layer. Nonetheless it also shows high variation of permeability. Figure 4.5 shows the logarithm of permeability for these layers. We assume a constant porosity for the layers and the

Table 4.2: Comparison of $\delta(s_{\text{rec}})$ error from different reconstruction schemes for tracer flow through layers 10, 37, 47 and 68 of SPE10 model.

Layer	$\delta(s_{\text{rec}})$ of PSM-NG	$\delta(s_{\text{rec}})$ of ALG-NG	$\delta(s_{\text{rec}})$ of PSM-MNG	$\delta(s_{\text{rec}})$ of ALG-MNG
10	0.13	0.09	0.19	0.07
37	0.48	0.29	0.47	0.25
47	0.64	0.37	0.61	0.30
68	0.47	0.38	0.47	0.30

coarse model is 6×22 upscaled from original 60×220 gridcells. For the solution of the saturation equation we implemented a sequential implicit scheme, that is, the pressure equation is first solved, and based on a fixed total velocity, the saturation equation is implicitly solved via an iteration loop in a decoupled sequence.

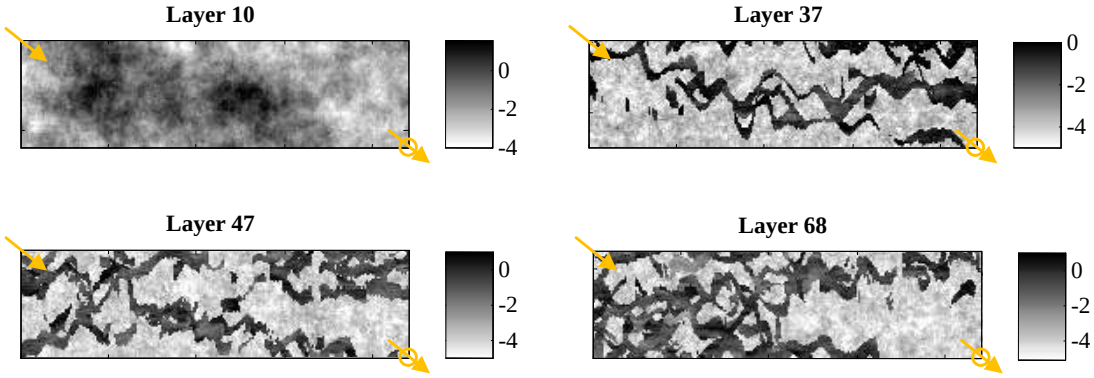

Figure 4.5: Logarithm of permeability fields for layers 10, 37, 47 and 68, from Model 2 from the 10th SPE Comparative Solution Project (Christie & Blunt, 2001). Inlet and outlet are also shown by arrows for the case of corner-to-corner flow.

Table 4.2 gives $\delta(s_{\text{rec}})$ over 1.5 PVI of simulation. Interestingly, MNG has improved the quality of saturation profiles for adaptive local global upscaling better than for pressure solver method. Applied on adaptive local global upscaling the improvement by MNG relative to NG at 1.5 PVI for the layers 10, 37, 47 and 68 are respectively 22.2, 9.06, 22.8 and 17.0 percent. Table 4.3 gives $\delta(v_{\text{rec}})$. The decrease in the values by modified algorithm for adaptive local global upscaling is even more emphatic for this error norm.

Figure 4.6 shows the tracer cut curves obtained for different layers at production cell.

Table 4.3: Comparison of $\delta(v_{\text{rec}})$ error from different reconstruction schemes for tracer flow through layers 10, 37, 47 and 68 of SPE10 model.

Layer	$\delta(v_{\text{rec}})$ of PSM-NG	$\delta(v_{\text{rec}})$ of ALG-NG	$\delta(v_{\text{rec}})$ of PSM-MNG	$\delta(v_{\text{rec}})$ of ALG-MNG
10	0.71	0.60	0.47	0.22
37	1.28	1.05	1.21	0.91
47	1.25	1.17	1.02	0.71
68	1.40	1.02	1.39	0.86

For layer 10, as we expect from heterogeneity pattern, PSM-NG is within a satisfying range. However, the other layers display the importance of correcting the transmissibilities by using the adaptive local global upscaling scheme. For these layers the error of homogenization through upscaling exceeds the one from the coarse representation of the saturation.

Although downscaling of the velocity field for the heterogeneous layers could not remove the error or the discrepancy with the fine scale's curve, we note that near-well upscaling can reduce such discrepancies, once the method is coupled with less accurate upscaling technique like PSM for regions away from the well. Near-well upscaling, as the name suggests, aims to specifically honour flow details around the well.

We note that the improvement by modified nested gridding downscaling of adaptive local global upscaling compared to conventional nested gridding is not reflected for the single value of saturation at the producing cell that determines the production.

4.3.2 Multiphase Flow

In this subsection, we test the modifications to a two-phase flow simulation to determine the improvement by modified nested gridding compared to conventional nested gridding and investigate the application of static downscaling algorithm. Two viscosity ratios are examined, $M = \mu_o/\mu_w = 0.1$ and $M = \mu_o/\mu_w = 10$. For $M = 0.1$ the front is sharp and piston-like while for $M = 10$, in contrast, the front lingers into the displaced fluid. From a reconstruction point of view, an unstable displacement (high viscosity ratios) is simpler to handle. The reason is that the increase of water saturation throughout the domain is more gradual due to a weak shock. This keeps the change in total mobility small enough that the coarse velocity field can take them into account more effectively. On the other hand the saturation increase is spatially abrupt and sudden for cases of sharp piston-like frontal displacements (low viscosity ratios). This gives the reconstruction oscillations and errors because the slightest of differences in locating the front in reconstruction

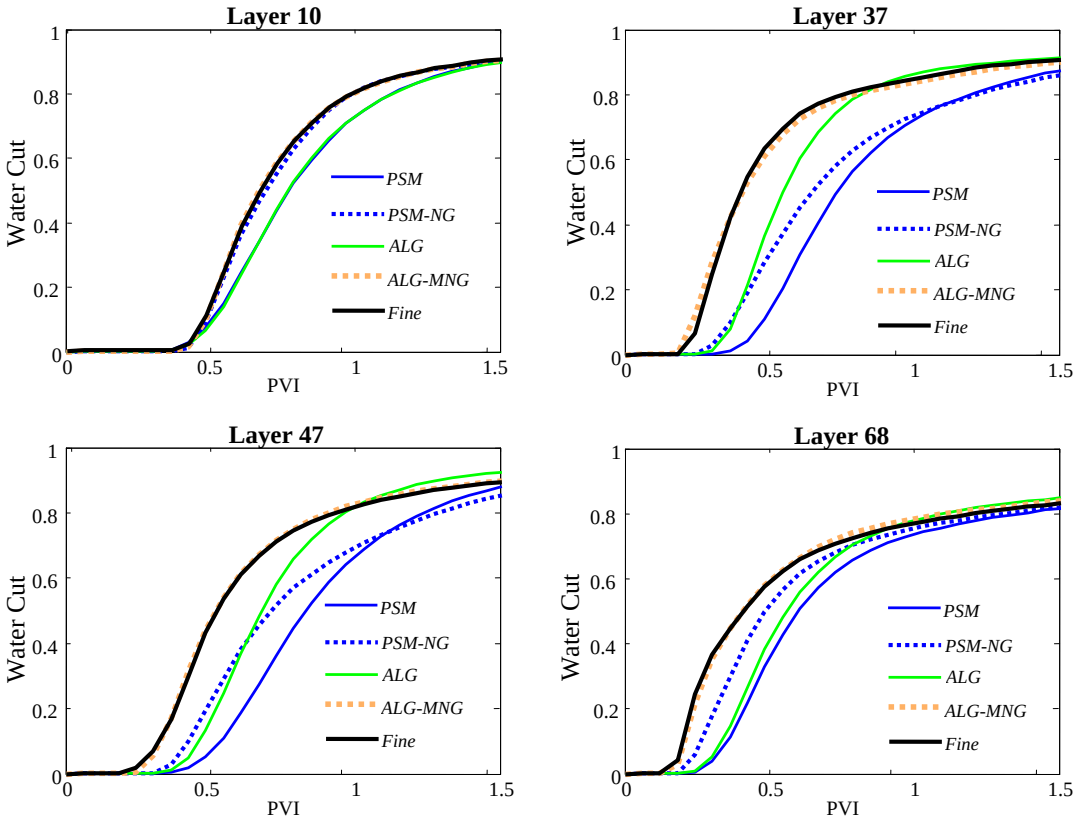

Figure 4.6: Tracer cut curves for tracer flow simulations on layers of 10, 37, 47 and 68 for reference fine model and different upscaling and upscaling-downscaling methods.

leads to large discrepancy of saturation values computed by different models.

Figure 4.7 shows the global error measured by $\zeta(s_{\text{rec}})$ for different reconstruction algorithms for multiphase flow $M = 10$ case. We observe an improvement by modified nested gridding compared to conventional nested gridding similar to tracer flow case. However, the loss of accuracy by static downscaling is visible for layer 10. In contrast, for channelized layers, the application of adaptive local global upscaling is advantageous due to high errors of pressure solver method upscaling. For these layers dynamic and static downscaling have almost similar values of error. To conclude, in any case of heterogeneity, modified nested gridding is obviously advantageous compared to conventional nested gridding, while for channelized heterogeneity static downscaling infers minimal loss of accuracy compared to dynamic downscaling.

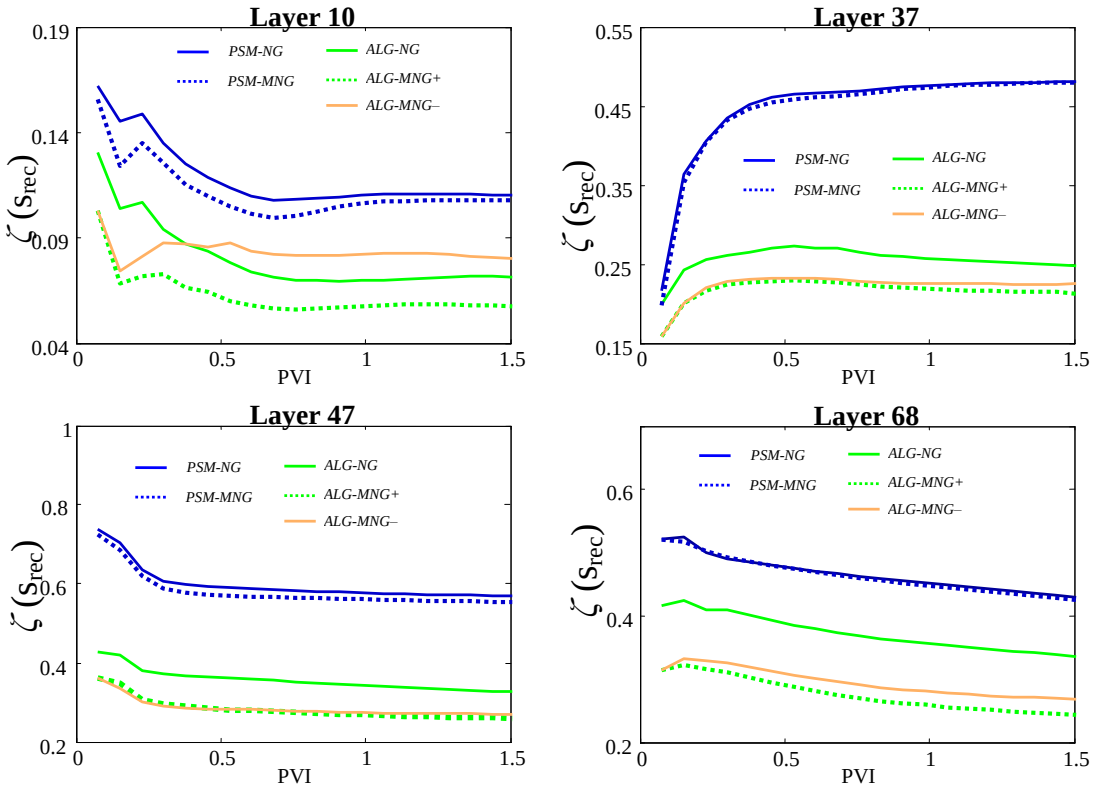

Figure 4.7: Comparison of $\zeta(s_{\text{rec}})$ from different reconstruction schemes for multiphase flow ($M = 10$) through layers 10, 37, 47 and 68 of SPE10 model.

Figure 4.8 and Figure 4.9 show the water cut curves calculated at producing cell for each layer and each viscosity ratio. In each panel, we have compared the curves obtained by ALG-MNG− to ALG-MNG+, PSM-NG and fine reference model. Only we

have spotted deterioration of ALG-MNG− curve compared to ALG-MNG+ for case of layer 10 with $M = 0.1$, while other cases confirm that non-updated basis functions for multiphase flow produce satisfying results.

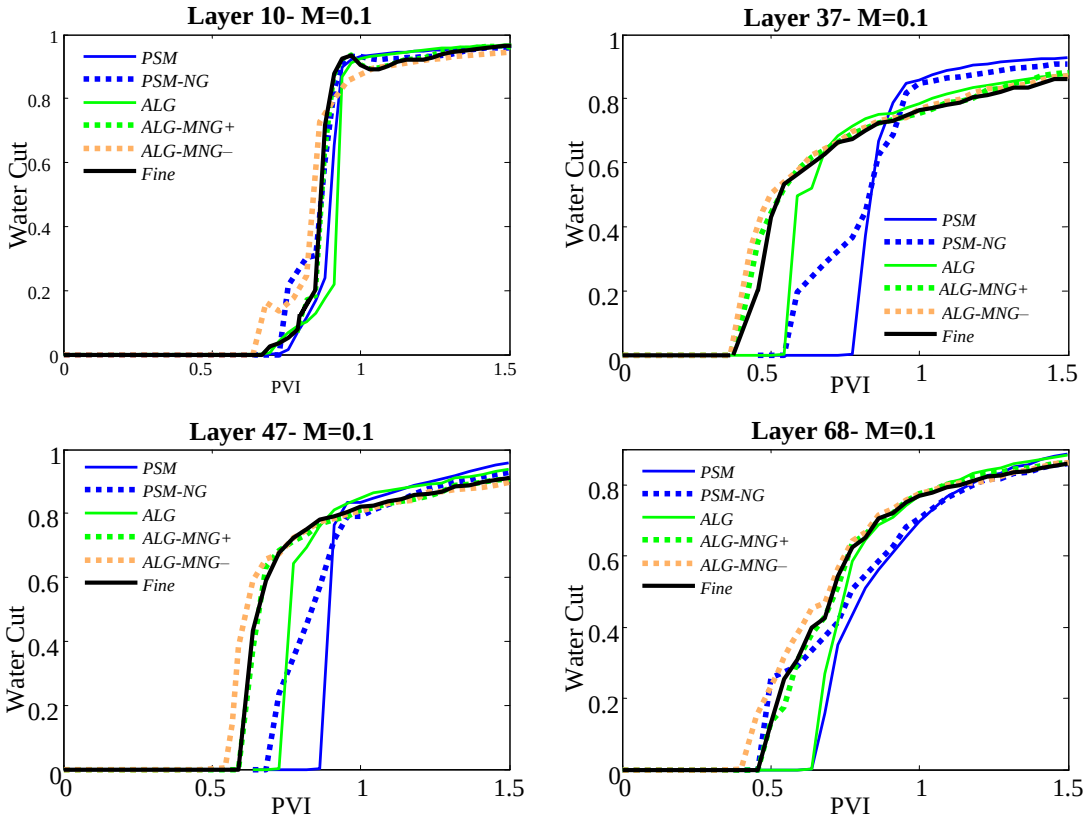

Figure 4.8: Water cut curves for multiphase flow simulations ($M = 0.1$) on layers of 10, 37, 47 and 68 for reference fine model and different upscaling and upscaling-downscaling methods.

Figure 4.10 shows fine scale saturation profiles constructed from fine reference model and three upscaling-downscaling algorithms at 1.5 PVI for layer 47. Figure 4.11 shows the absolute saturation error ($|s^{\text{ref}} - s^{\text{rec}}|$) for the layers that we considered in the comparison. Obviously the reconstruction based on PSM suffers significantly from bad upscaled values for coarse velocities due to inaccurate coarse properties and ALG-NG and ALG-MNG− have resulted similar profiles as of the fine-scale reference model.

After considering corner-to-corner flow, here, we examine the case of directional flow and constant pressure production. The boundary conditions are set as constant injection rate from one side of the reservoir and a constant pressure production at the other side. Again we upscale the fine layers (layers 37 and 47) from 60×220 grid cells to 6×22.

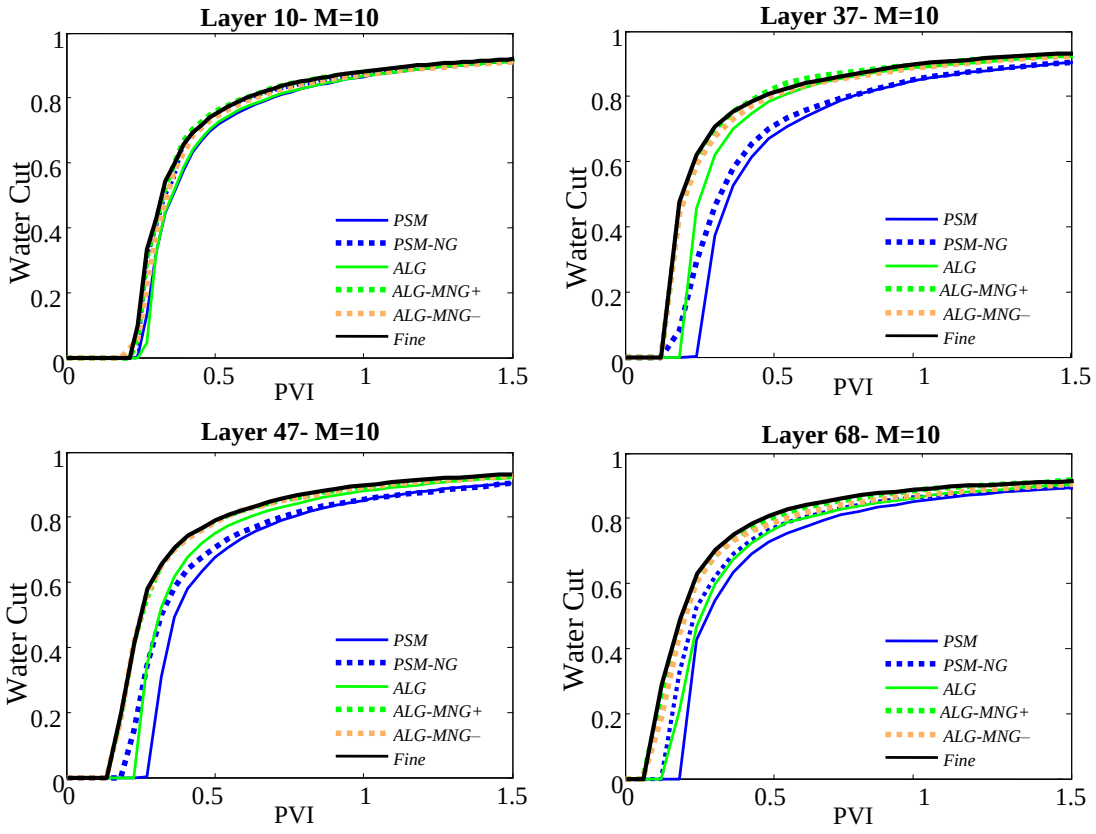

Figure 4.9: Water cut curves for multiphase flow simulations ($M = 10$) on layers of 10, 37, 47 and 68 for reference fine model and different upscaling and upscaling-downscaling methods.

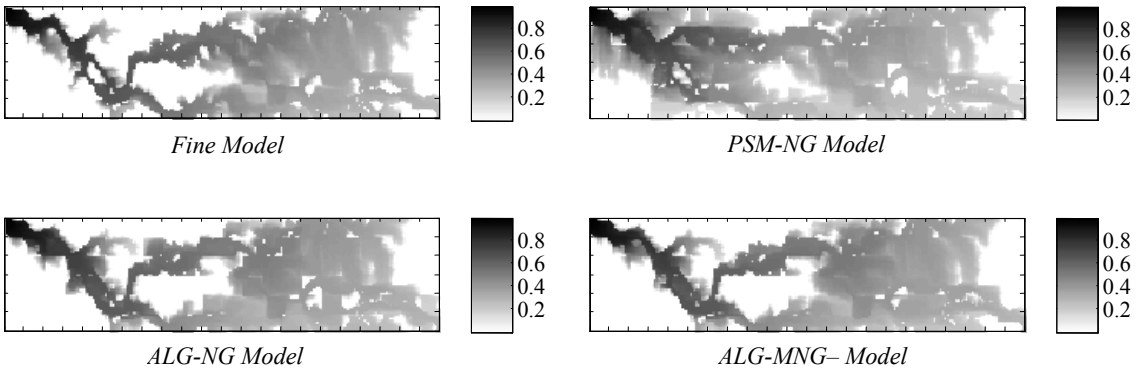

Figure 4.10: Fine scale saturation profiles obtained by different method for corner-to-corner flow, layer 47, at 1.5 PVI ($M = 10$).

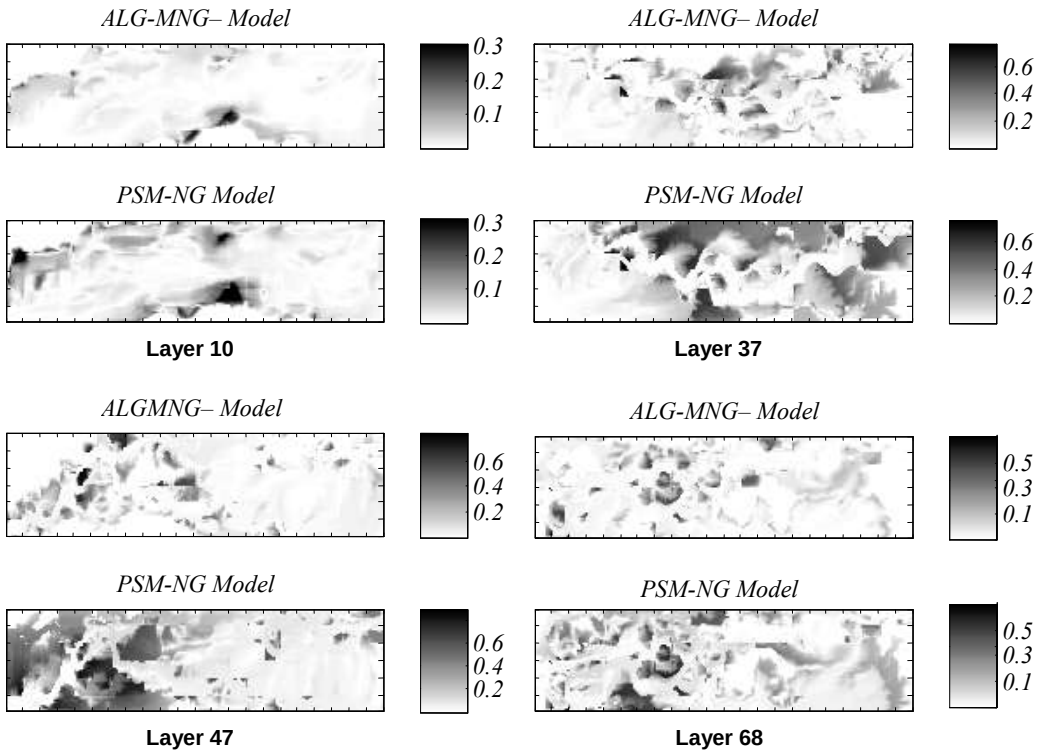

Figure 4.11: The absolute saturation error at 1.5 PVI ($M = 10$).

Table 4.4: Coarse pressure and fine saturation error for directional flow case.

Model	$\delta(P^c, P^f, t)$ of PSM	$\delta(P^c, P^f, t)$ of ALG	$\delta(s_{\text{rec}})$ of PSM-MNG	$\delta(s_{\text{rec}})$ of ALG-NG	$\delta(s_{\text{rec}})$ of ALG-MNG−
Layer 37	2.10	0.13	0.55	0.37	0.32
Layer 47	0.51	0.06	0.50	0.34	0.29

Here only the viscosity ratio of $M = 10$ is considered. For the assessment of the accuracy of the various techniques, we consider the accuracy of the pressure field and oil flow rate by calculating $Q_o/\Delta P$ versus time.

Figure 4.12 illustrates the improvement of results by ALG-NG, ALG-MNG− and ALG-MNG+ compared to PSM-NG. The improvement is mainly due to better coarse pressure values calculated by ALG upscaling. However, there is only a minimal improvement by ALG-MNG− compared to ALG-NG. Moreover, the application of distribution basis functions is completely reasonable as we observe no deterioration of results by ALG-MNG− compared to ALG-MNG+. In Table 4.4 the errors for coarse-scale pressure and fine-scale saturation are given by simulation to 2 PVI.

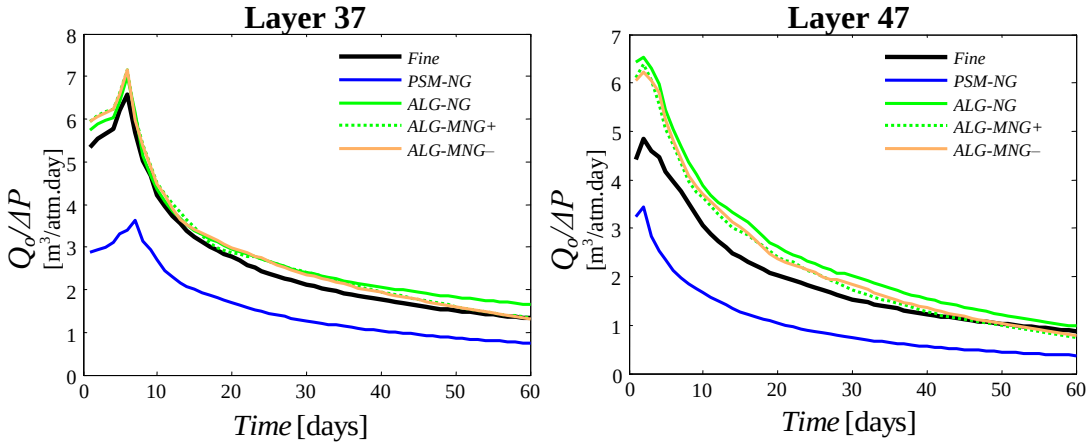

Figure 4.12: Comparison of various upscaling-downscaling techniques for directional flow case through $Q_o/\Delta P$.

The next test model, taken from Chen *et al.* (2004), is one realization of a 2D synthetic channelized system containing 100×100 grid cells on a Cartesian coordinate system. This model was generated using multi-point geostatistics (for the channels) and two-point geostatistics (for permeability distributions within each facies). This permeability model (Figure 4.13) is characterized by high variations from 0.02 to 6.5×10^7

millidarcy, a mean of 7×10^4 millidarcy and isotropic normalized correlation lengths varying from 0.05 to 0.5. In this model, the correlated permeabilities are not aligned with the Cartesian grid lines, but rotated at almost 45^o with respect to the grid. This model represents a case in which the flow solution is highly affected by grid orientation and flow conditions in the finite difference scheme, as the preferred flow paths are along high permeabilities, not the model coordinate system. The upscaling is difficult in this case due to high permeability variation, high permeability channel, and complex geometry of heterogeneities.

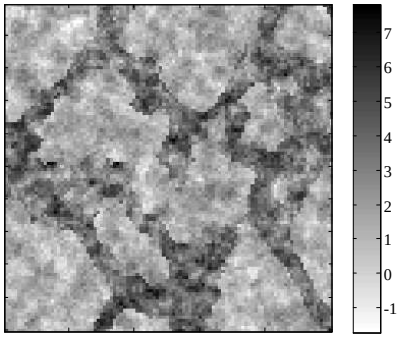

Figure 4.13: Logarithm of absolute permeability for synthetic channelized model.

We examine tracer flow induced by corner-to-corner source and sink configuration. We upscale this model to 10×10 grid blocks and test the same algorithms of reconstruction as before. In Figure 4.14 we have confirmed the performance of ALG-MNG− in lowering the fine scale saturation error compared to ALG-NG− and PSM-NG.

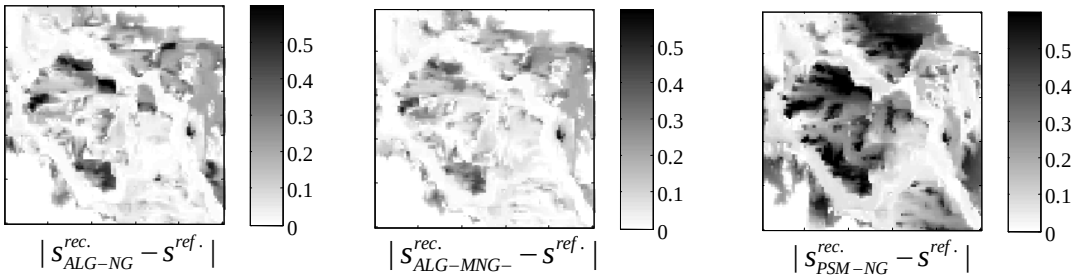

Figure 4.14: Improvement in saturation absolute error by modifications in reconstruction of velocity at 2 PVI.

To investigate the effect of the upscaling factor on performance of ALG-MNG− we have carried different coarsening levels on this test case: upscale from 100×100 to 25×25, to 10×10 and 5×5. By calculating $\zeta(s_{\text{rec}})$ vs. time, we can see in Figure 4.15

that we observe less improvement by modified nested gridding compared to conventional nested gridding for 25×25 case. That is to say for lower upscaling factors (like 25×25 case with upscaling factor of only 16) proportionality indices calculated by fine scale transmissibilities are close enough to those calculated by approximate velocity field. In comparison of ALG-MNG− and ALG-MNG+ we observe $\zeta(s_{\text{rec}})$ for ALG-MNG− only to exceed that of ALG-MNG+ after 1 PVI for upscaling factors of 400 (5×5) and 100 (10×10).

To finalize this case, we note that for a 2D upscaling factor of 100 which is a more usual case for reservoir simulation upscaling, we see a good improvement in terms of saturation error by MNG compared to NG (from 0.31 to 0.23 at 2 PVI) and small deterioration by using static downscaling algorithm (from 0.23 to 0.26 at 2 PVI).

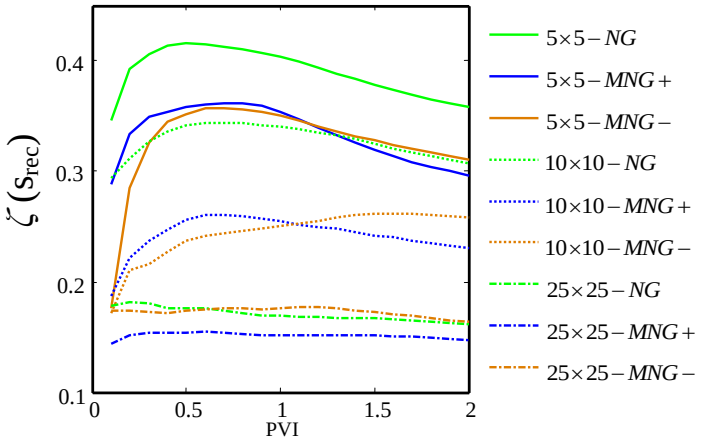

Figure 4.15: Effect of upscaling factor on performance of basis functions for downscaling.

In directional flow case, we performed similar analysis of errors for $Q_o/\Delta P$, and errors for coarse-scale pressure and fine-scale saturation. Results are respectively presented in Figure 4.16 and Table 4.5. Similar to layers 37 and 47 that were examined for directional flow, this example shows that high coarse pressure errors by PSM are removed by ALG upscaling. From downscaling point of view, there is some improvements by MNG compared to NG and no under-performance by MNG− compared to MNG+.

4.3.3 Simulation Runtime for a 3D Case

In previous tests we showed that by the upscaling-downscaling scheme we can generate a good approximation to the flow compared to a fine reference model by ALG-MNG−. However, the most important factor is to keep the efficiency of upscaling in terms of CPU gain and memory reduction. In our algorithm we only focus on pressure equation

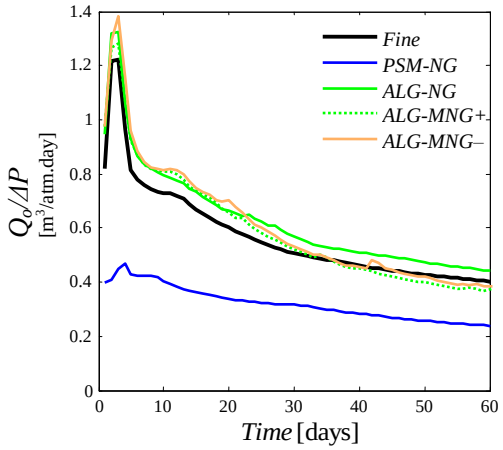

Figure 4.16: Channel case: comparison of various upscaling-downscaling techniques for directional flow case through $Q_o/\Delta P$.

Table 4.5: Channel case: coarse pressure and fine saturation error measurements for directional flow case at 6 PVI.

Model	$\delta(P^c, P^f, t)$ of PSM	$\delta(P^c, P^f, t)$ of ALG	$\delta(s_{\text{rec}})$ of PSM-MNG	$\delta(s_{\text{rec}})$ of ALG-NG	$\delta(s_{\text{rec}})$ of ALG-MNG−
Channel case	0.56	0.10	0.39	0.22	0.17

upscaling and once we reconstruct a velocity field the computation for the saturation equation is as expensive as it is for the fine model. In the calculation of CPU time, we assume that the superposition of velocity basis functions is not computationally demanding since it does not involve any equation to solve. Hence, for the downscaling part of the time for nested-gridding is not considered. For large scale reservoir models the superposition is actually a matter of optimized programming and can easily outperform linear solution of local problems.

For a three dimensional example, we take a section of SPE10 model bottom 50 layers (Upper-Ness fluvial channelized formation). The section is a 60×60×50 grid with variation of permeability between 9.63×10^{-7} to 20 millidarcy. We upscale it to 6×6×5 blocks with PSM, PSM-NG, ALG-NG− and ALG-MNG− methods as in the previous cases. The water flooding boundary conditions are corner to corner flow case with constant pressure production at one corner and constant injection rate at the other. We use a mobility ratio of M=10 and relative permeabilities from Equation 3.22 for the water and oil phases. For local-global method the computations can be costly given that in three dimensions, calculation of a corrected set of transmissibilities involves extended regions 8 times the size of their target coarse block (8,000:1,000 cells in this example). The application of local-global iteration therefore is very time consuming unless strong measures for adaptivity are enforced. Therefore we put a maximum of 2-iteration limit for updating transmissibilities.

In Figure 4.17 (left panel), $\zeta(s_{\text{rec}})$ vs. time for three algorithms of upscaling-downscaling are shown. We again observe improvement in the reconstructed saturation fields for ALG-MNG− compared to ALG-NG and PSM-NG. This confirms both corrections in the upscaling stage by adaptive local global method in three dimension as well as improvements in downscaling stage by modified nested gridding. In right panel of this figure, the oil flow rates are plotted and the curve for ALG-MNG− is in good agreement with that of fine reference model. However, the difference between curves of ALG-NG and ALG-MNG− is very insignificant. Therefore the improvements in this plot are essentially due to ALG upscaling and not modified downscaling. In Figure 4.18 the saturation profiles at 0.4 PVI are shown.

For the analysis of computational complexity, we presented CPU time for each of methods in Table 4.6. The machine used is an Intel Xeon 2.67GHz CPU processor and 4.00 GB RAM. As mentioned earlier, the CPU times are only for solution of the pressure equation so that we see a significant speed-up factor for PSM and equally for PSM-NG. In PSM we deal with solution of very small 6×6×5 systems, so that the computations drastically drop to less than a second for our machine. However this is not the case for ALG techniques. Even with adaptivity, the calculation of corrected boundary

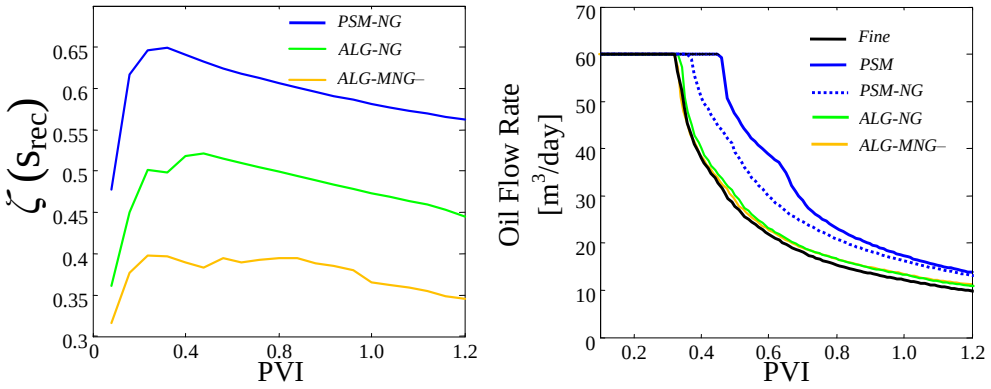

Figure 4.17: Left is $\zeta(s_{\text{rec}})$ vs. time, right is the curves for oil production rate with different methods.

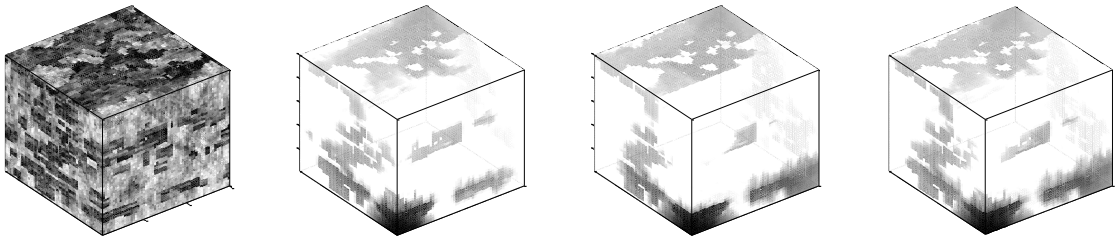

Figure 4.18: Logarithm of permeability and Saturation profiles at 0.4 PVI for different models under comparison for the 3D case.

Table 4.6: Time consumption for solution of the pressure equation by different methods for a 3D case study

Method	$\delta(P^c)$ at 1 PVI	$\zeta(s_{\text{rec}})$ at 1 PVI	Q_{oil} at 1 PVI	CPU time (sec)
Fine	–	–	12.17	331.8
PSM	0.34	–	17.30	0.037
PSM-NG	0.34	0.56	16.23	0.037
ALG-NG	0.12	0.44	13.35	54.42
ALG-MNG−	0.12	0.35	13.35	54.42

conditions for dynamic coarse grid blocks and following iterations have undermined upscaling speed-up. Nonetheless for three dimensions Wen *et al.* (2006) have shown that optimized programming in addition to modifications in the size of the extended region can lead to reasonable speed-up factors for ALG upscaling. Our emphasis however in three dimensional cases like previous examples still remains on the reduction of nested gridding error by MNG and application of MNG−.

4.3.4 Comparison of Upscaling-Static-Downscaling (ALG-MNG–) with Multiscale Mixed Finite Element (MSMFE)

Here, we use a code developed by Lie *et al.* (2011) to compare the performance of multiscale mixed finite element (MSMFE) with upscaling-static-downscaling (ALG-MNG–). The objective is to investigate if a simplistic upscaling-downscaling can provide the accuracy of a more algorithmically complex multiscale method. In our comparison, we will not consider the computational aspect of either of the methods because the MSMFE code, similar to our ALG-MNG− code, has been currently developed only for theoretical and small-scale reservoir cases. However, it suffices to refer to a computational comparison study presented by Kippe *et al.* (2008) between ALG-NG and three multiscale methods. The conclusion there is that, ALG-NG is the least computationally efficient method. This may not be always the case as in their study, they point out two drawbacks for ALG-NG. First, they consider that the velocity reconstruction should be performed globally everywhere and at all times for ALG-NG. Second, they did *not* enforce adaptivity for the upscaling stage of the algorithm in order to avoid possible deterioration of performance of the algorithm. These two factors, however, were negated by the use of basis functions for the reconstruction stage and we also observed consistency of the results by adaptivity in the upscaling stage. Unfortunately at this stage, we are unable to perform a proper study on computational efficiency of ALG-MNG− compared to existing multiscale methods and keep the comparison very simplistic.

We consider the performance of methods for corner-to-corner multiphase flow simu-

Table 4.7: Saturation error, $\delta(s_{\text{rec}})$, for MSMFE and ALG-MNG−.

Layer	MSMFE	ALG-MNG−	Layer	MSMFE	ALG-MNG−
10	0.07	0.06	47	0.28	0.27
37	0.26	0.26	68	0.46	0.30

lation ($M = 10$) of layers 10, 37, 47 and 68 of SPE10. Table 4.7 is a report of global $\delta(s_{\text{rec}})$ error for these layers. Figure 4.19 shows water cut curves obtained by different methods. It is clear that ALG-MNG− has a better performance and this is most pronounced in the case of layer 68. For this layer, $\delta(s_{\text{rec}})$ for MSMFE is 54.6 % higher than that of ALG-MNG−. The saturation profiles for this layer at the end of simulation are shown in Figure 4.20.

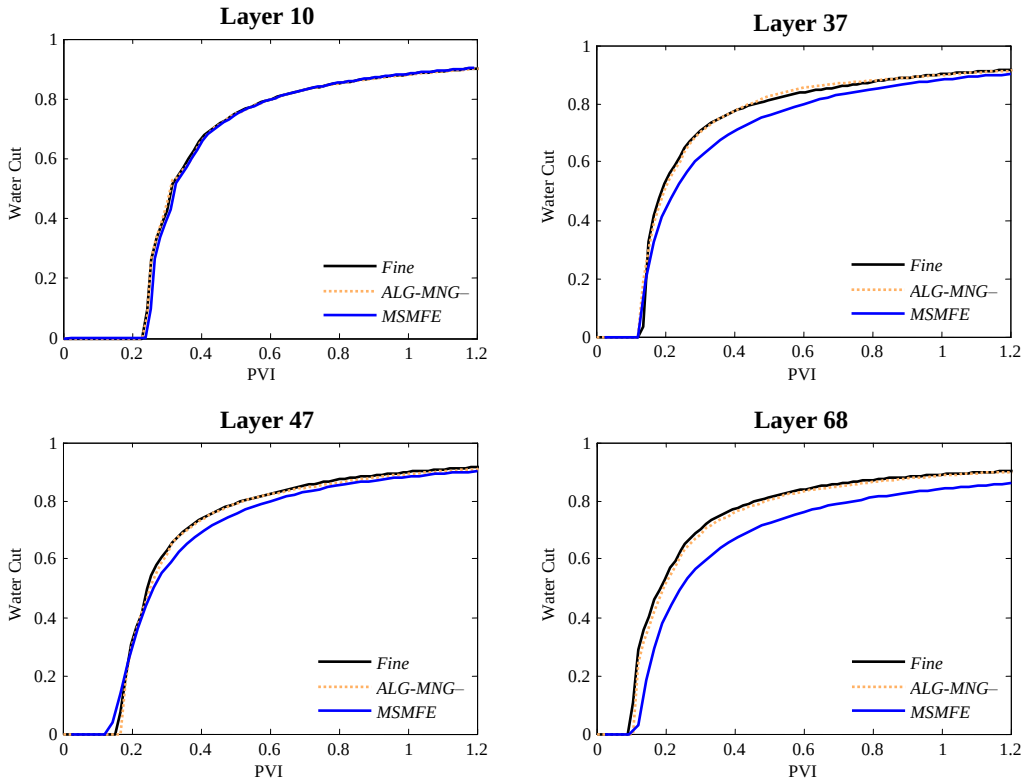

Figure 4.19: Water cut curves obtained by ALG-MNG− and MSMFE for multiphase flow simulation.

We note that the quality of MSMFE and other multiscale methods can be improved, in a similar way to ALG upscaling, by incorporating global information into the upscaling

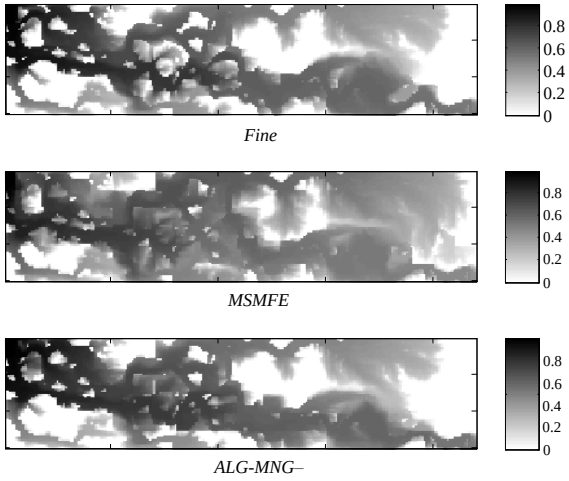

Figure 4.20: Saturation profiles for different models at 1.2 PVI, layer 68 of SPE10.

stage of the algorithms and definition of local basis functions. This has been investigated in Efendiev *et al.* (2006) and Durlofsky *et al.* (2007). The modified algorithms use either an initial fine scale velocity to correct the velocity basis functions in MSMFE or the fine scale pressure to correct upscaled transmissibilities in MSFV. Adaptivity can also be enforced to update basis functions only where and when needed. The aforementioned references show very promising accurate multiscale tools. Nonetheless, we note that, if the global information is to be exploited, it is very likely that ALG-MNG− offers a less algorithmically complex procedure than local-global multiscale methods.

4.3.5 Summary of Results

We have introduced modifications in downscaling by nested gridding that reduces computational overhead compared to the original scheme of nested gridding and can lead to better quality reconstructed saturation profiles. This modification stems from mimicking the behaviour of the fine velocity distribution from an extended-local upscaling stage. In an attempt to exploit the incompressibility of waterflooding, to avoid linear solvers in nested gridding, we showed that it is practical to only initially calculate and then reuse a set of basis functions for velocity reconstruction. The application is demonstrated in two and three dimensional test cases as well as using different sets of boundary conditions including corner to corner flow and directional flow with constant pressure production. We showed that use of these functions did not particularly undermine the strength of the ALG-NG upscaling-downscaling for strongly channelized systems. For the 3D case, our non-optimized code for ALG upscaling affected consider-

ably the speed-up factor but the result for the downscaling stage in lowering the error for fine saturation profiles and the application of basis functions remained as promising as in two dimensional cases.

5 EOR Applications of Upscaling-Static-Downscaling (ALG-MNG−)

The upscaling-static-downscaling (ALG-MNG−) method is applied in this chapter to simulate of a group of EOR flooding processes. The chemical flooding processes including polymer and surfactant flooding exhibit a wide range of difficulties for multiphase upscaling. The change in viscosities and relative permeability curves of the fluids are among these difficulties. For evaluating the improved technique, we compare the results with the fine scale reference model. The reference model is in turn validated by frontal advance theory in Section 5.1. ALG-MNG− method is tested for highly heterogeneous porous media under different scenarios of secondary recovery in Section 5.2.

5.1 Numerical Validation of the Fine Scale Solution

This section covers the validation of numerical simulation of the displacement by polymer, surfactant and thermal flooding with frontal advance theory Buckley & Leverett (1942), Claridge & Bondor (1974), Pope (1980). The purpose is to validate the fine scale model used for numerical simulation in the comparison study. The analytical results are based on Buckley-Leverett solutions of one-dimensional homogeneous cases. The examples are as follows: Example 1 is a case of polymer flooding with a simplistic rheology for the polymer. The polymer fluid is injected after a conventional waterflooding. The higher viscosity of injected fluid boosts the recovery. Example 2 is also a polymer flooding case with the difference that in this case the oil bank does not form and the polymer fluid is injected right from the beginning. In Example 3 we validate numerical simulation of surfactant flood with adsorption and change of relative permeability curves due to a reduced residual oil saturation. Ultimately, in Example 4, a thermal flooding analytical solution is used to validate numerical solution. In this example the viscosities of fluids are reduced due to the use of heated water and the equation for energy balance affects the saturation profiles.

5.1.1 Example 1: Polymer Flooding

In this example, we use a linear displacement example presented in Green & Willhite (1998). Water and viscous polymer fluids are injected into a one dimensional homogeneous system. The polymer fluid is miscible with the previously injected water, which has a low viscosity. It is also assumed that the polymer fluid is not adsorbed on the rock. No mixing occurs between the polymer fluid and the low-viscosity resident water. Thus, a boundary exists between the polymer and displaced water where there is a step change, or jump, in viscosity from viscosity of resident water μ_w to viscosity of polymer fluid μ_p. The resident water forms the leading flood front and because there is a discontinuity in the viscosity between the polymer and resident fluids, a second discontinuity in saturation, or shock front, must form at the boundary of polymer and resident water (Green & Willhite, 1998).

Formation of the polymer shock

A conceptual model of the displacement process is developed by considering the injection of polymer at some time after a waterflood has started. The waterflood and the polymer solution parameters used are given in Table 5.1.

For relative permeability, the relationships considered for oil and water are:

$$k_{ro} = \alpha_1(1 - S_{wD})^m, k_{rw} = \alpha_2(S_{wD})^n, \tag{5.1}$$

Table 5.1: Properties used for Example 1

Property	Value
Porosity, ϕ	0.20
Connate water saturation, S_{wc}	0.30
Residual oil saturation, S_{wc}	0.30
Oil viscosity, μ_o,cp	40
Water viscosity, μ_w,cp	1.0
Polymer viscosity, μ_p,cp	4.0

where $S_{wD} = (S_w - S_{wc})/(1 - S_{or} - S_{wc})$. S_w, S_{wc} and S_{or} are respectively water saturation, connate water saturation and residual oil saturation. For this example we used $\alpha_1 = 0.8$, $\alpha_2 = 0.2$, $m = 2$, $n = 2$.

The water material balance leads to

$$(A\varphi)\frac{\partial S_w}{\partial t} + q_t\frac{\partial f_w}{\partial x} = 0, \tag{5.2}$$

where A is cross sectional area, φ is porosity, q_t is injection rate, f_w is fractional flow of water, t is time from the beginning of injection, and any consistent set of units may be used. In case the system is horizontal and gravity-and capillary effects are negligible, the fractional flow of water is $f_w = \frac{k_w/\mu_w}{k_w/\mu_w + k_o/\mu_o}$. Using dimensionless variables, $x_D = x/L$ and $t_D = q_t t/A\phi$, the above equation changes to:

$$\frac{\partial S_w}{\partial t_D} + \frac{\partial f_w}{\partial x_D} = 0. \tag{5.3}$$

The derivation of an expression for the saturation velocities by frontal advance theory begins with writing $S_w = S_w(x_D, t_D)$ then, $dS_w = \left(\frac{\partial S_w}{\partial x_D}\right)_{t_D} dx_D + \left(\frac{\partial S_w}{\partial t_D}\right)_{x_D} dt_D$, for a path of constant saturation $dS_w = 0$ so

$$\left(\frac{\partial x_D}{\partial t_D}\right)_{S_w} = -\left(\frac{\partial S_w}{\partial t_D}\right)_{x_D} \Big/ \left(\frac{\partial S_w}{\partial x_D}\right)_{t_D} = v_{S_w}. \tag{5.4}$$

Combining Equations. 5.3 and 5.4, gives a constant velocity with which each S_w travels:

$$\left(\frac{dx_D}{dt_D}\right)_{S_w} = \left(\frac{df_w}{dS_w}\right)_{S=Sw}, \tag{5.5}$$

The flood-front saturation is found by constructing a tangent to the fractional flow curve ($f_w - S_w$ curve) from S_{wc} when the water in the rock is initially at connate

saturation, i.e., immobile. The slope of the tangent is given by:

$$f'_{wf} = \frac{f_{wf} - f_{wc}}{S_{wf} - S_{wc}}, \tag{5.6}$$

where f_{wf} is the fractional flow of water at the flood-front saturation, f_{wc} is the fractional flow of water at connate water saturation equal to zero, S_{wf} is flood-front saturation, and S_{wc} is the connate water saturation.

The flood-front or saturation shock moves at a velocity given by:

$$v_{wf} = \left(\frac{df_w}{dS_w}\right)_{S=Swf} = f'_{wf}. \tag{5.7}$$

All saturations less than S_{wf} travel at the flood-front velocity. The location of a particular saturation is found by integrating Equation 5.5 with respect to time to obtain:

$$(x_D)_{S_w} = t_D f'_w. \tag{5.8}$$

Because the velocity of every saturation is constant, the graph of saturation location versus time is a set of straight lines starting from the origin.

When polymer enters the linear system at $x_D = 0$ and $t_D = t_{D0}$ and dispersion is neglected, a miscible boundary forms between the injected water and the polymer. At this boundary, the velocity of the polymer phase must be equal to the velocity of the displaced water. The *specific velocity* of the resident water phase is given by:

$$v = f_w q_t / A\phi S_w, \tag{5.9}$$

where $A\phi S_w$ is the cross-sectional area that the water flows through. By analogy, for the specific velocity of the polymer phase:

$$v_p = f_p q_t / A\phi S_p, \tag{5.10}$$

where S_p and f_p are the water saturation and the fractional flow of the polymer. At the boundary between the polymer solution and the displaced water, the velocities of the two phases must be equal (i.e., $v = v_p$). Thus,

$$f_w / S_w = f_p / S_p. \tag{5.11}$$

It is convenient to express these velocities in terms of dimensionless parameters by

introducing the specific velocity defined as:

$$v_{Dp} = v_p/(q_t/A\phi). \tag{5.12}$$

The velocity of the saturation discontinuity is obtained by the *continuity equation* (Green & Willhite, 1998):

$$v_{Dv} = (\partial f_p/\partial S_p)_{S_{pf}} = (f_{pf} - f_{w1})/(S_{pf} - S_{w1}), \tag{5.13}$$

where, S_{pf} is the saturation on the upstream side of the discontinuity and S_{w1} is the saturation on the downstream side of the discontinuity. Because the specific water velocity must be equal to the velocity of the discontinuity,

$$v_{Dpf} = v_{Dw1}, \tag{5.14}$$

so

$$(f_{pf} - f_{w1})/(S_{pf} - S_{w1}) = f_{pf}/S_{pf} = f_{w1}/S_{w1}. \tag{5.15}$$

f_{pf} and S_{pf} can be found by constructing a tangent from the origin to the $f_p - S_p$, as shown in Figure 5.1**a**. The intersection of this tangent with the fractional-flow curve gives the values of f_{w1} and S_{w1}. With these values, the displacement of the shock caused by the differences in viscosities is completely defined.

The saturations of polymer fluid higher than S_{pf} that satisfy Equation 5.11 are found by drawing a straight line from the origin of the fractional-flow curve through S_p to intersect the $f_w - S_w$ curve at S_w, f_w. Figure 5.1**b** is an enlargement of the upper portion of Figure 5.1**a**. Lines a through f are drawn from the origin to $f_p - S_p$, which intersects the $f_w - S_w$ curve at S_w, f_w.

Inspection of Figure 5.1**b** reveals that $v_{Dv} > f'_w$ and $v_{Dv} > f'_p$ until $S_p = S_{pf}$, where $v_{Dv} = f'_{pf}$. Thus, the velocity of the polymer shock increases until it is equal to f_{pf} at S_{pf}, where it becomes stabilized at its maximum value. Smaller S_w values are encountered as the polymer fluid penetrates the rear of the original waterflood saturation profile. S_p, must decrease from $1 - S_{or}$ along the path from line a to line f to S_{pf}, while S_w must decrease from $1 - S_{or}$ to S_{wF} along the same path (see Figure 5.1**b**). Within a timestep that S_w^{n+1} is overtaken by S_p^{n+1}, the position of this two saturations are defined by:

$$x_{Dv}^{n+1} = t_D^{n+1} f_w'^{n+1}, \tag{5.16}$$

and

$$x_{Dv}^{n+1} = \int_0^{t_D} v_{Dv}^{n+1} dt_D = \int_0^{t_D} \left(\frac{f_w - f_p}{S_w - S_p}\right)^{n+1} dt_D. \tag{5.17}$$

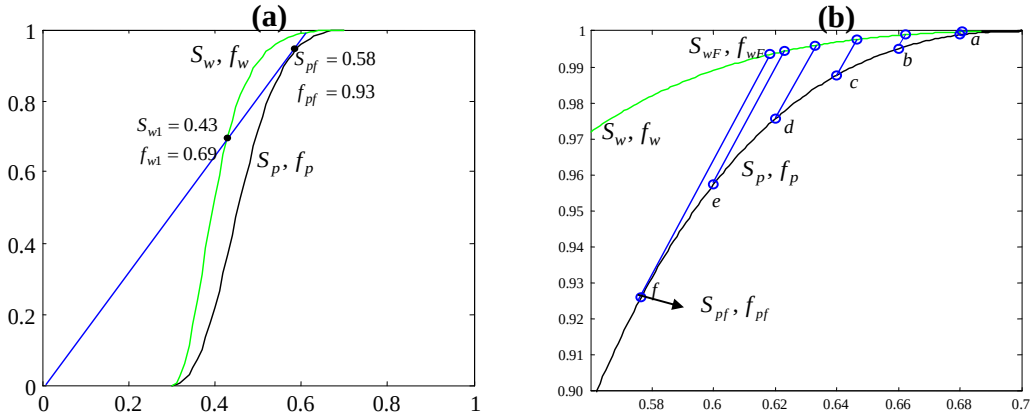

Figure 5.1: **(a)**: Fractional flow curves for water and polymer fluid. The graphical technique of finding the polymer shock front (at S_{pf}, f_{pf}) and oil bank water saturation (at S_{w1}, f_{w1}). **(b)**: Upper part of fractional flow curves for water and polymer fluid. Lines a to f represents the path within which the polymer fluid saturations supersede resident water saturations.

For integration of Equation 5.17, it is possible to use an average velocity for v_{Dv}^{n+1} and approximate the integral as:

$$x_{Dv}^{n+1} = x_{Dv}^{n} + \bar{v}_{Dv}^{n+1}(t_D^{n+1} - t_D^n), \tag{5.18}$$

which

$$\bar{v}_{Dv}^{n+1} = \frac{1}{2}\left(\left(\frac{f_w - f_p}{S_w - S_p}\right)^n + \left(\frac{f_w - f_p}{S_w - S_p}\right)^{n+1}\right). \tag{5.19}$$

Substituting Equation 5.16 into Equation 5.18 and solving for the time when the shock intersects the path of S_w^{n+1} yield:

$$t_D^{n+1} = \frac{x_{Dv}^n - \bar{v}_{Dv}^{n+1} t_D^n}{f_w'^{n+1} - \bar{v}_{Dv}^{n+1}}. \tag{5.20}$$

With pairs of S_w^{n+1} overtaken by by S_p^{n+1} depicted at the ends of lines a to f in Figure 5.1**b**, the evolution of the polymer shock can be calculated in a succession. The polymer shock in distance-time diagram intersects S_w^{n+1} from original waterflood lines to initiate new lines for S_p^{n+1}. The location of S_{pf} at subsequent times $t_D > t_{D0}$ is given by the frontal advance solution:

$$x_p = (t_D - t_{pD0}) f_w'^{n+1} + x_{pD0}, \tag{5.21}$$

where t_{pD0} and x_{pD0} are time and location where S_{Pf} evolves from the saturation discontinuity calculated from Equation 5.20 and Equation 5.16.

Oil bank formation

If $S_{w1} > S_{wf}$ an oil bank forms ahead of the polymer fluid and behind the resident water bank. If $S_{w1} < S_{wf}$ and t_{D0} is small, S_{w1} can overtake S_{wf} leaving no possibility for an oil bank to form. The value of S_{w1} can be graphically measured as shown in Figure 5.1. In this example, $S_{w1} = 0.427$ and $S_{wf} = 0.420$. Therefore we see an oil bank formation although S_{w1} is marginally higher than S_{wf} .The resident water saturation at the front of the oil bank (S_{wr}) approaches S_{w1} asymptotically. The oil bank extends between the position of S_{pf} and position of S_{wr}. Next the positioning of S_{wr} will be discussed.

Following the oil bank shock by front tracking

The front of the oil bank, a jump from S_{w1} to S_{wr}, can be followed in the same manner used to track the evolution of the polymer shock. As the oil shock moves, it intersects the paths of saturations in the water bank after the flood front forms i.e, $S_{wF} > S_w > S_{wf}$. Similar to the path of polymer shock in time-distance diagram, the points at oil bank shock must satisfy both frontal-advance of waterflood and overtaking by the oil bank. The velocity of the oil bank from the continuity equation around the shock is:

$$v_{Dr} = \frac{f_{wr} - f_{w1}}{S_{wr} - S_{w1}}, \tag{5.22}$$

and similar to Equation 5.18 for the distance traversed by the oil bank shock from the S^n_{wr} saturation line to the S^{n+1}_{wr} saturation line:

$$x^{n+1}_{Dr} = x^n_{Dr} + \bar{v}^{n+1}_{Dr}(t^{n+1}_D - t^n_D), \tag{5.23}$$

where

$$\bar{v}^{n+1}_{Dr} = \frac{1}{2}\left(\left(\frac{f_{wr} - f_{w1}}{S_{wr} - S_{w1}}\right)^n + \left(\frac{f_{wr} - f_{w1}}{S_{wr} - S_{w1}}\right)^{n+1}\right), \tag{5.24}$$

where v_{Dr} is dimensionless velocity of the oil-bank shock, x_{Dr} is location of the shock at t^{n+1}_D and $\bar{v}^{n+1}_{Dr}$ is average velocity of the shock between t^n_D and t^{n+1}_D. x^n_{Dr} and x^{n+1}_{Dr} can also be expressed in terms of frontal-advance equation (i.e. $x_{Dr} = t_D f'^{n+1}_{wr}$), so

$$t^{n+1}_D f'^{n+1}_{wr} = t^n_D f'^n_{wr} + \bar{v}^{n+1}_{Dr}(t^{n+1}_D - t^n_D), \tag{5.25}$$

and

$$t_D^{n+1} = t_D^n \frac{f_{wr}'^n - \bar{v}_{Dr}^n}{f_{wr}'^{n+1} - \bar{v}_{Dr}^{n+1}}. \tag{5.26}$$

The path followed by the front of the oil bank is computed by determining the value of x_{Dr} in Equation 5.23 as S_{wr} decreases. This path may be visualized by constructing the series of lines from S_{w1} to the $f_w - S_w$ curve. The slope of each line is the specific velocity of the oil bank shock at S_{wr}.

Figure 5.2 and Figure 5.3 are the distance/time diagram for a polymer flooding that began after injecting $t_{D0} = 0.06\ PV$ of water into a linear system. The path of the polymer shock appears to be linear because the maximum specific velocity of the shock, v_{DF}, is reached at $t_{pD0} = 0.069$ at point **A** in Figure 5.3. However, as shown in Figure 5.3 the specific velocity of the front of the oil bank continuously increases with t_D. In this example, the oil bank does not overtake the flood front S_{wf}, before it leaves the system at $x_D = 1.0$. Consequently, the polymer flooding would perform like the regular waterflood until breakthrough of the oil bank at $t_D = 0.33$.

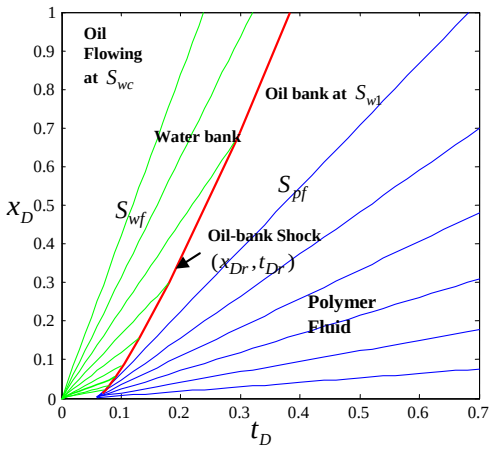

Figure 5.2: Time/Distance diagram for polymer fluid injection until $t_D = 0.7\ PV$ after a conventional waterflood that has been in operation until $t_{D0} = 0.06\ PV$.

Description of the solute concentration

The material balance equation for the solute concentration (polymer or salt, for instance) denoted by C in the polymer fluid, is given by (Sorbie, 1991):

$$\frac{\partial C S_w}{\partial t_D} + \frac{\partial C f_w}{\partial x_D} = 0. \tag{5.27}$$

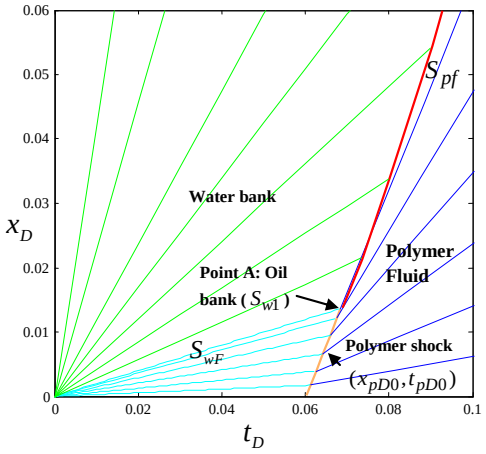

Figure 5.3: Evolution of the polymer shock at $t_{D0} = 0.06\ PV$. Cyan lines represent resident water saturations that are intersected by the polymer shock while green lines represent resident water saturations that are intersected by the oil bank shock or leave the system non-intersected.

Expanding the differentials and using Equation 5.3 we have:

$$S_w \frac{\partial C}{\partial t_D} + f_w \frac{\partial C}{\partial x_D} = 0. \tag{5.28}$$

which describes the movement of a sharp concentration front through the porous rock. There is no dispersion or mixing of the fluids, and the concentration jumps from 0 to maximum concentration (1 for here) at the concentration front. The concentration front can be followed by deriving an expression for the concentration velocity by frontal advance theory. Consider a path of constant composition where $C = C(x_D, t_D)$ then, $dC = \left(\frac{\partial C}{\partial x_D}\right)_{t_D} dx_D + \left(\frac{\partial C}{\partial t_D}\right)_{x_D} dt_D$, for a path of constant composition $dC = 0$ and

$$\left(\frac{\partial x_D}{\partial t_D}\right)_C = -\left(\frac{\partial C}{\partial t_D}\right)_{x_D} \Big/ \left(\frac{\partial C}{\partial x_D}\right)_{t_D} = v_C, \tag{5.29}$$

which gives the specific velocity of the concentration shock. Combining Equations. 5.28 and 5.29, gives

$$v_C = \frac{dx_D}{dt_D} = \frac{f_w}{S_w}. \tag{5.30}$$

Because the concentration front causes the saturation shock and these shocks must travel at the same specific velocity, the specific velocity of the concentration front is the same as that of saturation shock.

Numerical simulations

In this part the results of numerical simulation of the polymer fluid injection at $t_{D0} = 0.06$ after conventional waterflood are compared with saturation profiles obtained from frontal advance theory.

The numerical simulations are based on the finite difference discretization of conventional waterflood and the aqueous-phase transport equations for one dimensional case. For the aqueous-phase transport equation, ignoring physical dispersion, we discretize:

$$\frac{\partial C S_w}{\partial t_D} + \frac{\partial C \tilde{f}_w(S_w, C)}{\partial x_D} = 0, \tag{5.31}$$

where $\tilde{f}_w$ is the fractional flow of the mixed aqueous phase (water and the polymer fluid). The definition of $\tilde{f}_w$ as a function of C directly affects the numerical simulation results. We briefly describe here a conventional approach and a recent improved one based on AlSofi & Blunt (2012) that reduces the numerical diffusion error.

Traditionally the fractional flow of the aqueous phase is defined by:

$$\tilde{f}_w = \frac{1}{1 + \frac{\tilde{\mu}_w(C)}{\tilde{k}_{rw}(C)} \frac{k_{ro}}{\mu_o}}, \tag{5.32}$$

where $\tilde{\mu}_w(C)$ is the mixed phase viscosity and is defined as a linear or quadratic function of the solute concentration. In the linear case of concentration-viscosity dependence, we can write $\tilde{\mu}_w(C) = (1 - C)\mu_w + C\mu_p$. Finally, $\tilde{k}_{rw}(C)$ is the relative permeability of the mixed phase. Here we assumed that the polymer fluid is not modifying the relative permeability curves, hence $\tilde{k}_{rw}(C)$ is the same as $k_{rw}(S)$.

Alternatively AlSofi & Blunt (2012) modified the definition of $\tilde{f}_w$ in which the aqueous phase is decomposed into *segregated* water and polymer fractional flows:

$$\tilde{f}_w = (1 - C) f_w + C f_p = (1 - C) \frac{1}{1 + \frac{\mu_w}{k_{rw}} \frac{k_{ro}}{\mu_o}} + C \frac{1}{1 + \frac{\mu_p}{k_{rp}} \frac{k_{ro}}{\mu_o}}, \tag{5.33}$$

Then for the transport, the discretization of Equation 5.31 is replaced with:

$$\frac{\partial C S_w}{\partial t_D} + \frac{\partial C f_p(S_w, C)}{\partial x_D} = 0, \tag{5.34}$$

that is, the solute is being transported strictly by the polymer fluid fractional flow (f_p) only, instead of the overall aqueous phase fractional flow ($\tilde{f}_w$). This formulation is equivalent to assuming that the process takes place as a segregation-in-flow (denoted henceforth by SEG), as opposed to the traditional instant full mixing assumption (denoted henceforth by IFM)(AlSofi & Blunt, 2010). The improvements obtained by this

modification in terms of reduction of the numerical diffusion error is shown for Example 1, in Figure 5.4. In this figure, the concentration and saturation profiles are shown at $t_D = 0.15$ PVI and the reduction of smearing effect by implementing SEG scheme is evident. Such reduction, however, can be more outstanding for certain set of viscosity values (as for the next example) that infers greater differences between fractional flow of water and the polymer fluid.

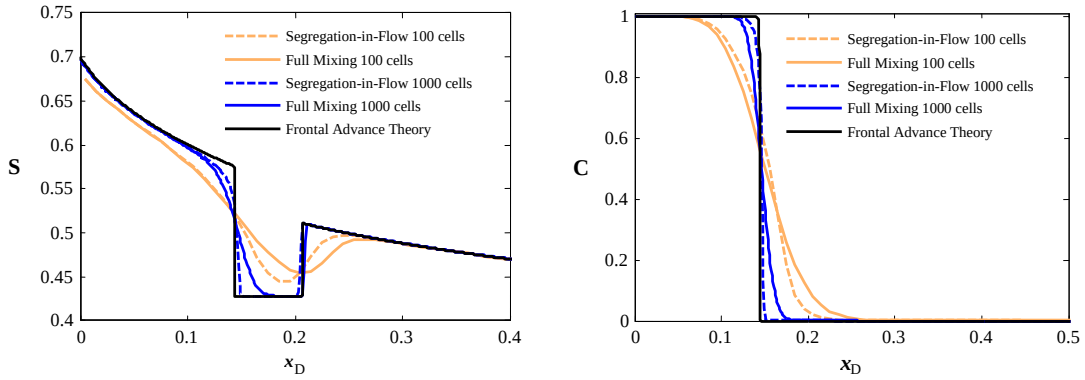

Figure 5.4: The improvements of numerical simulation by SEG scheme for saturation and concentration profiles for Example 1 at $t_D = 0.15$ PVI.

Continuing the simulations, the saturation profiles from frontal advance and numerical calculations (10,000 cells and with SEG scheme) are compared in Figure 5.5 at $t_D = 0.06$, $t_D = 0.09$, $t_D = 0.15$ and $t_D = 0.3$. The agreement is complete between the two methods.

5.1.2 Example 2: Injection of Polymer at Connate Water Saturation

In this example, a polymer injection to a linear reservoir at connate water saturation is considered. As in the previous example the injected polymer fluid is miscible with the connate water and is not retained on the porous rock by adsorption or other mechanisms. The properties of the polymer fluid, connate water and oil are given in Table 5.2.

For relative permeability, the relationships of Equation 5.1 are used with:$\alpha_1 = 1.0$, $\alpha_2 = 0.4$, $m = 2$ and $n = 2$

A polymer shock forms instantaneously with the same properties of previous example:

$$\left(\frac{dx_D}{dt_D}\right)_{S_{pf}} = \frac{f_{pf} - f_{w1}}{S_{pf} - S_{w1}}, \tag{5.35}$$

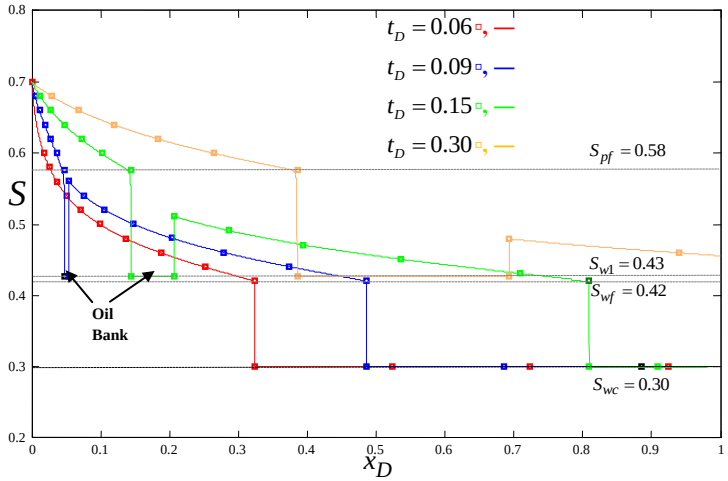

Figure 5.5: The profiles for water saturation. The solid lines are calculated from numerical simulator while the rectangular markers are the results of frontal advance theory.

Table 5.2: Properties used for Example 2

Property	Value
Porosity, ϕ	0.20
Connate water saturation, S_{wc}	0.20
Residual oil saturation, S_{wc}	0.20
Oil viscosity, μ_o, cp	10
Water viscosity, μ_w, cp	1.0
Polymer viscosity, μ_p, cp	20

and

$$x_{D3} = t_D \frac{f_{pf} - f_{w1}}{S_{pf} - S_{w1}}. \tag{5.36}$$

Water saturations greater than S_{pf} travel at velocities given by:

$$\left(\frac{dx_D}{dt_D}\right)_{S_p} = \left(\frac{f_p}{S_p}\right)_{S_p}. \tag{5.37}$$

Using the properties of Table 5.2, the values of S_{pf} and S_{w1} are determined graphically as shown in Figure 5.6**a** to be $S_{pf} = 0.760$ and $S_{w1} = 0.405$. Also similar to S_{pf} for water fractional curve, we can determine that $S_{wf} = 0.468$. Unlike the previous example, $S_{wf} > S_{w1}$, therefore the oil bank forms immediately, overtakes S_{wf} and has a uniform water saturation of S_{w1}. The velocity of the oil bank is given by:

$$\left(\frac{dx_D}{dt_D}\right)_{S_{w1}} = \frac{f_{w1}}{S_{w1} - S_{wc}}. \tag{5.38}$$

With the help of Equation 5.37 and Equation 5.38, the time/distance diagram of this example for until $t_D = 0.3$ of PVI is shown in Figure 5.6**b**.

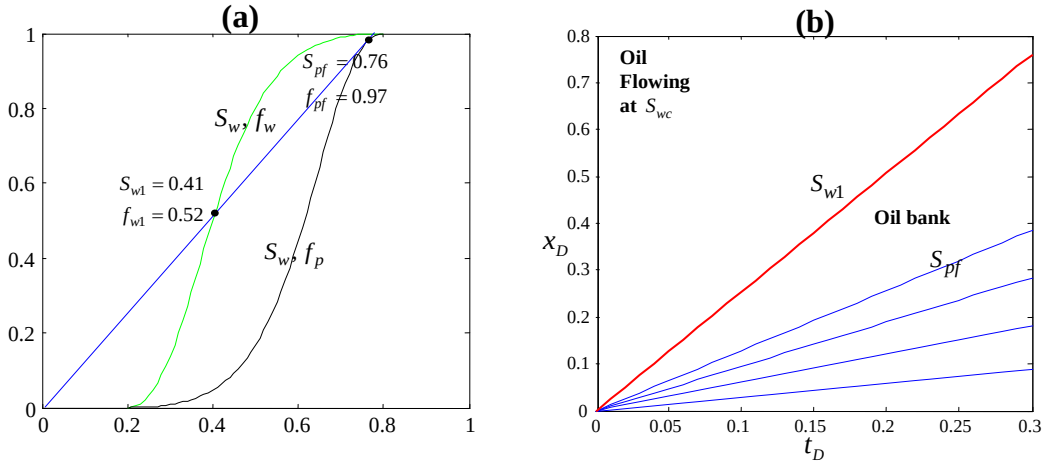

Figure 5.6: **(a)**: The polymer shock front (at S_{pf}, f_{pf}) and oil bank water saturation (at S_{w1}, f_{w1}) for Example 2. **(b)**: The time/distance diagram for Example 2 from beginning to t_D=0.3 PV injected.

For the numerical simulation part, due to the larger gap between the fractional flow curves of water and the polymer fluid, we are able to demonstrate the improvements achieved by the use of the SEG scheme. The difference between mixed phase fractional curves obtained by either Equation 5.32 or Equation 5.33 is shown in Figure 5.7**a**. The difference is very significant and the curvature in $\tilde{f}_{w,SEG}$ will lead to saturation velocities

(shown in Figure 5.7**b**) quite different from those obtained by $\tilde{f}_{w,IFM}$. The saturation velocities ($f'_w = \frac{df_w}{dS_w}$) obtained by SEG scheme clearly represent two shocks (water and the polymer fluid) while those obtained by IFM scheme show smeared shocks.

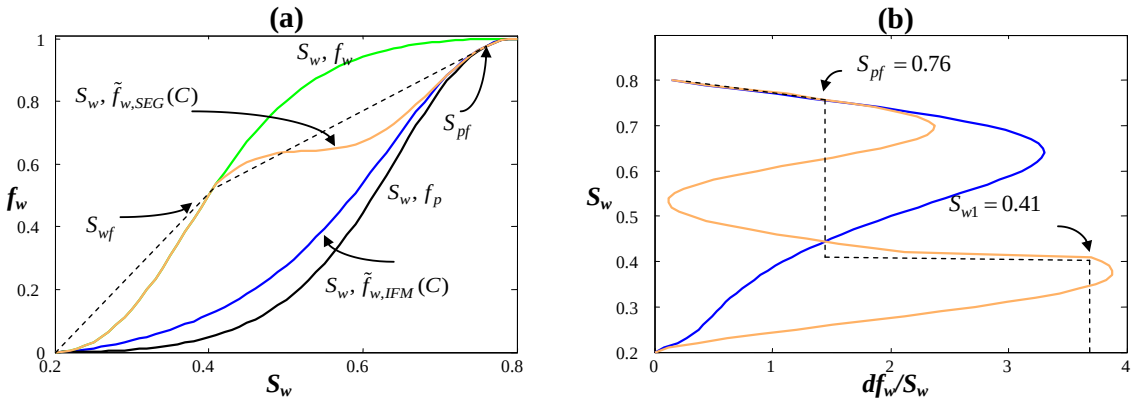

Figure 5.7: **(a)**: The fractional flow curves for water, the polymer fluid and the mixed phase by IFM and SEG schemes. **(b)**: water saturation velocities induced by the polymer fluid injection obtained by the two schemes. Also shown are the frontal advance solutions in dashed black.

Finally, the agreement of the saturation and concentration profiles with the frontal advance theory as well as the reduction in numerical diffusion by SEG are shown in Figure 5.8.

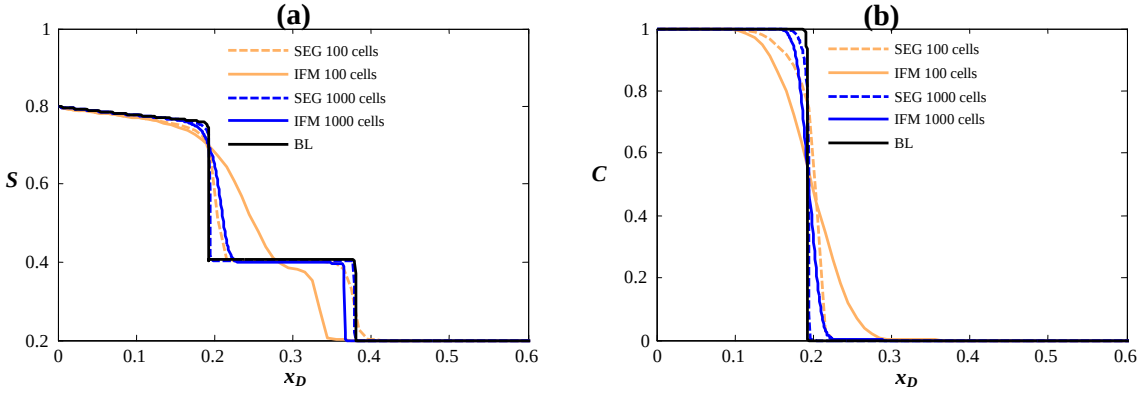

Figure 5.8: The improvements of numerical simulation by SEG scheme for saturation and concentration profiles for Example 2 at $t_D = 0.15$ PVI.

5.1.3 Example 3: Surfactant Flooding

In this example we validate numerical simulation of surfactant flooding. The surfactant reduces the IFT between the injected fluid and the oil. The reduction has two effects on the relative permeability curves (Talash, 1976). Firstly, the relative permeability curves have less curvature. Secondly is the reduction of the residual oil saturation from S_{or}, the waterflood residual oil, to S_{sor}, the residual saturation to the surfactant flood. This reduction shifts the fractional flow curve toward higher water saturations. In this example we assume the chemical system reduces the IFT sufficiently to obtain $S_{sor} = 0.10$ for the reservoir rock and oil system presented in Example 1. We assume, however, that the curvatures of the relative permeability curves are left unchanged.

The effects of adsorption and retention occurring as a result of rock-fluid interactions by chemicals, are described for the concentration equation by:

$$\frac{\partial C(S_w + D_i)}{\partial t_D} + \frac{\partial C f_w}{\partial x_D} = 0, \tag{5.39}$$

where D_i is a convenient factor defined to represent the retention of species i on the rock by:

$$D_i = \partial \hat{C}_i / \partial C, \tag{5.40}$$

where $\hat{C}_i$ is retention of species i in terms of the pore volume of the rock:

$$\partial \hat{C}_i = \frac{A_i \rho_{gr}(1-\varphi)}{\varphi}, \tag{5.41}$$

where A_i is the amount of species i retained by the rock and ρ_{gr} is the density of the rock. It is assumed that the porosity occupied by species i is φ. The surfactant in this example is assumed to be strongly adsorbed and retarded by retention of chemical species on the rock so that for the sharp-front approximation, $D_i = \hat{C}_i / C = 0.8$.

For the movement of the concentration shock, we can simply notice that everything is similar to the previous examples, with the only difference being the existence of D_i. Hence the specific velocity of the concentration shock is:

$$v_{C_i} = \frac{dx_D}{dt_D} = \frac{f_w}{S_w + D_i}. \tag{5.42}$$

And again because the concentration front causes the saturation shock and these shocks must travel at the same specific velocity, the specific velocity of the saturation shock is

$$\left(\frac{dx_D}{dt_D}\right)_{S_{sf}} = \left(\frac{\partial f_w}{\partial S_w}\right)_{S_{sf}} = \frac{f_{sf} - f_{w1}}{S_{sf} - S_{w1}}. \tag{5.43}$$

Thus

$$\frac{dx_D}{dt_D} = \frac{f_{w1}}{S_{w1} + D_i} = \frac{f_{sf} - f_{w1}}{S_{sf} - S_{w1}} = \frac{f_{sf}}{S_{sf} + D_i}. \tag{5.44}$$

Inspection of Equation 5.44 shows that the values of f_{sf} and S_{sf} can be found by drawing a tangent to the $f_s - S_w$ fractional flow curve from the point $f_s = 0$, $S_w = -D_i$. The intersection of this tangent with the (f_w, S_w) curve for the original oil/water system gives (f_{w1}, S_{w1}). Figure 5.9 shows the construction procedure. The positions of S_{sf}, S_{w1} and S_{wf} at time t_D are respectively, $x_{Df} = t_D f'_{sf}$, $x_{D1} = t_D f'_{w1}$ and $x_{Df} = t_D f'_{wf}$.

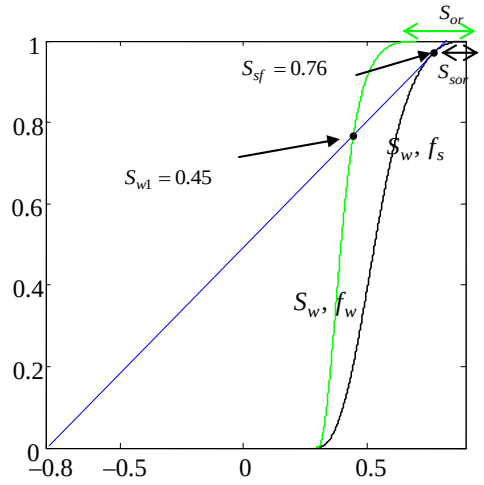

Figure 5.9: Construction procedure to determine f_{sf} and S_{sf} for when adsorption occurs, Example 3.

For the numerical simulations, we use only the SEG scheme. In this, the segregated water, the segregated chemical and the oil fractional flow functions are calculated by:

$$\begin{aligned}
\lambda_w &= \alpha_1 (S_{wD})^n / \mu_w, \\
\lambda_s &= \alpha_1 (S_{sD})^n / \mu_s, \\
\lambda_o &= (1 - C)\alpha_2 (1 - S_{wD})^m / \mu_o + C\alpha_2 (1 - S_{sD})^m / \mu_o,
\end{aligned} \tag{5.45}$$

where $S_{wD} = \frac{S - S_{wc}}{1 - S_{wc} - S_{or}}$ and $S_{sD} = \frac{S - S_{wc}}{1 - S_{wc} - S_{sor}}$. Then we have $f_w = \frac{\lambda_w}{\lambda_w + \lambda_s + \lambda_o}$, $f_s = \frac{\lambda_s}{\lambda_w + \lambda_s + \lambda_o}$ and $f_o = \frac{\lambda_o}{\lambda_w + \lambda_s + \lambda_o}$. With these, the calculation of the mixed phase fractional flow $(\tilde{f}_w)$ will be similar to Equation 5.33.

Figure 5.10 is the saturation profiles by frontal advance theory as well as the numerical simulations.

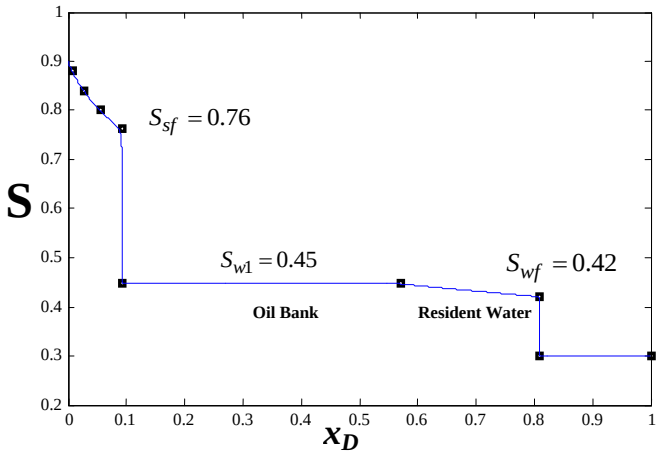

Figure 5.10: Saturation profile for surfactant flood of Example 3 at $t_D = 0.15$. Solid line is based on the numerical simulation and rectangles are based on the frontal-advance theory.

5.1.4 Example 4: Thermal Flooding

In this example, a simple thermal flooding is considered to validate the numerical simulation. We assume injection of hot water into a reservoir saturated initially with cold fluid and containing cold connate water. The hot water warms up the oil and reduces its viscosity and mobilizes it. It is assumed that oil responds more to heating than the water so that the viscosity ratio (viscosity of oil divided by that of water) decreases to favourable values for a piston-like displacement. In this case we have two fractional flow curves each pertinent to different temperatures, i.e. f_w is a function of both saturation and temperature. The cold fluid fractional-flow is represented by f_w and the thermal hot fluid fractional-flow is represented by f_{th}.

The governing equations for thermal flooding are the material balance for water and energy balance that determines the temperature profile. For a dimensionless set of equations that are easy to work with, we use the assumptions and formulation of references Bratvold (1989) and Dindoruk & Dindoruk (2008):

$$\frac{\partial S_w}{\partial t_D} + \frac{\partial f_w(T_D, S_w)}{\partial x_D} = 0, \tag{5.46}$$

and

$$(S_w + \beta)\frac{\partial T_D}{\partial t_D} + (f_w + \alpha)\frac{\partial f_w}{\partial x_D} = 0, \tag{5.47}$$

where T_D is normalized dimensionless temperature defined as:

$$T_D = (T - T_{min})/(T_{max} - T_{min}), \tag{5.48}$$

and α and β are dimensionless functions of the thermal properties of rock and fluid, and as well as porosity:

$$\alpha = \frac{\rho_o c_{vo}}{\rho_w c_{vw} - \rho_o c_{vo}}, \tag{5.49}$$

and

$$\beta = \frac{\rho_o c_{vo} + \frac{1-\phi}{\phi}\rho_r c_{vr}}{\rho_w c_{vw} - \rho_o c_{vo}}, \tag{5.50}$$

where c_{vr}, c_{vo} and c_{vw} are heat capacity of rock, oil and water respectively and ρ_r, ρ_o and ρ_w are density of rock, oil and water respectively. The assumptions for the derivation of Equation 5.47 is that heat is not conducted by rock and it is just convected by the fluid. Similar to Example 3, for the specific velocity of temperature shock we have:

$$v_{T_D} = \frac{dx_D}{dt_D} = \frac{f_w + \alpha}{S_w + \beta} \tag{5.51}$$

Because the temperature front causes the saturation shock and these shocks must travel at the same specific velocity, we have:

$$\frac{dx_D}{dt_D} = \frac{f_{w1} + \alpha}{S_{w1} + \beta} = \frac{f_{thf} - f_{w1}}{S_{thf} - S_{w1}} = \frac{f_{thf} + \alpha}{S_{thf} + \beta}. \tag{5.52}$$

Inspection of Equation 5.52 shows that the values of f_{thf} and S_{thf} can be found by drawing a tangent to the $f_{th} - S_w$ fractional flow curve of hot water from the point $f_{th} = -\alpha$, $S_w = -\beta$. The intersection of this tangent with the (f_w, S_w) curve for the cold fluid gives (f_{w1}, S_{w1}).

In addition to the equations for water saturation and temperature, we can use a non-adsorbing tracer with a similar transport equation:

$$S_w \frac{\partial C}{\partial t_D} + f_w \frac{\partial C}{\partial x_D} = 0. \tag{5.53}$$

However, f_w is not a function of tracer concentration and the C-front does not affect the saturation profile.

The properties we consider here are the same properties used for hot water injection into cold reservoir for the base case investigated in Dindoruk & Dindoruk (2008). The properties are reported in Table 5.3 and Table 5.4. For relative permeabilities, we put $\alpha_1 = \alpha_2 = 1.0$ and $n = m = 3$ in Equation 5.1 and $S_{wc} = 0.18$ and $S_{or} = 0.20$. Based on these properties, Figure 5.11 shows the procedure of finding S_{thf}, S_{w1} and S_{wf}. The

Table 5.3: Thermal properties and densities of rock and fluids used for Example 4

	Porosity	Heat Capacity $(Btu/lb-F)$	Density (lb/ft^3)	α	β
Oil		0.45	53.04		
Water		1.00	62.40		
Rock	0.25	0.31	126.54	0.62	3.73

Table 5.4: Temperature dependent parameters (fluid viscosity) used for Example 4

T(F)	$\mu_o(cp)$	$\mu_w(cp)$
180 (Hot Fluid)	2	0.70
70 (Cold Fluid)	8	1

positions of S_{thf}, S_{w1} and S_{wf} at time t_D are respectively, $x_{Dthf} = t_D f'_{thf}$, $x_{D1} = t_D f'_{w1}$ and $x_{Df} = t_D f'_{wf}$.

The SEG scheme used here is the same as Equation 5.45 the only difference being that T is used instead of C. It is notable, however, that due to a narrow gap between the two fractional curves of cold and hot fluids in this example, there is no significant benefit in using the SEG scheme.

Figure 5.12 is the saturation profiles by frontal advance theory as well as numerical results at $t_D = 0.25$ PVI.

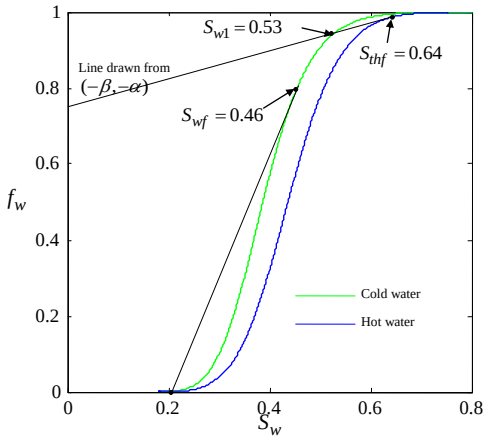

Figure 5.11: Construction procedure to determine f_{thf} and S_{thf} for thermal flood, Example 4.

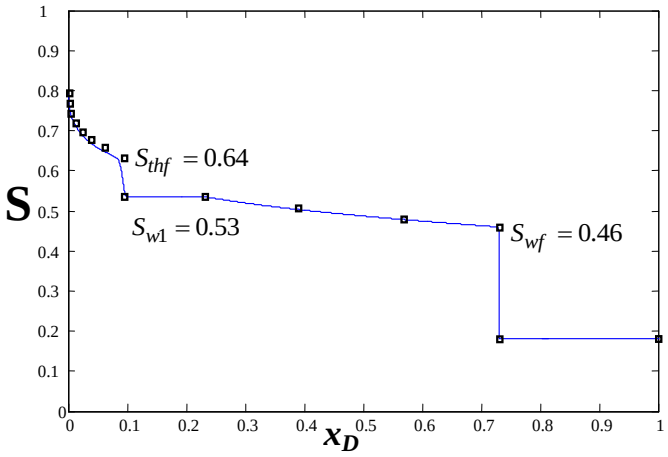

Figure 5.12: Saturation profile for thermal flood of Example 4 at $t_D = 0.25$. Solid line is based on the numerical simulation and rectangles are based on the frontal-advance theory.

5.2 Numerical Assessment of ALG-MNG−

In this section, we compare the results of the application of Chapter 4 upscaling and upscaling-downscaling techniques (listed in Table 4.1) on two and three dimensional test cases for polymer (viscous fluid), surfactant and thermal flooding. For the two dimensional case, we consider layers 37 and 47 of SPE10 model, upscaled from 60×220 to 6×22. For the three dimensional case, we consider the same SPE10 subsection used in the the previous chapter, upscaled from $60 \times 60 \times 50$ to $6 \times 6 \times 5$ and a homogeneous case, upscaled from $20 \times 20 \times 20$ to $5 \times 5 \times 5$. The objective remains to assess the performance of static downscaling, ALG-MNG−, described in the previous chapter.

5.2.1 Polymer Flooding

We start the comparisons with fluid properties used in Example 1 of the previous section and rock properties of layers 37 and 47. Although we use the SEG scheme for the upscaled models, the improvements are not considerable bearing in mind that the gap between the fractional flow curves of water and the viscous fluid is not prominent. Hence we leave the illustration of possible improvements for the next example. We compare water cut curves as well as curves for the recovery factor vs. time. The polymer is injected after 0.25 PVI injection of water and is continued up until 1.5 PVI. The results are shown in Figure 5.13.

Quite clearly, the static downscaling (ALG-MNG−) shows very good agreement with the fine reference method. This is very important since we have *not* updated the velocity basis functions for the polymer flood initiation and in the downscaling we relied only on the coarse velocities to inform the change of the flooding scenario. Such performance and agreement on the locally measured water cut and the recovery factor quantities assure us that global error estimates too remain as strongly in favour of ALG-MNG− as they were in the previous chapter.

Next, the same fluid properties of Example 2 were used with polymer flood right from the beginning. As noted previously, here the SEG scheme is naturally favourable for the upscaled method since it reduces the numerical diffusion of the saturation coarse-scale representation. It is however interesting to test the performance of the downscaled SEG and IFM coarse-scale velocities.

To start, we apply downscaling on homogeneous models. The model was solved with a 100×100 grid with the SEG scheme for the fractional flow. For the downscaling we consider three methods: one with the SEG scheme for both the coarse-scale (10×10) and fine-scale fractional flow curves in solution of the saturation equation, denoted by Downscaled–1, one with IMF scheme for both the coarse-scale and the fine-scale frac-

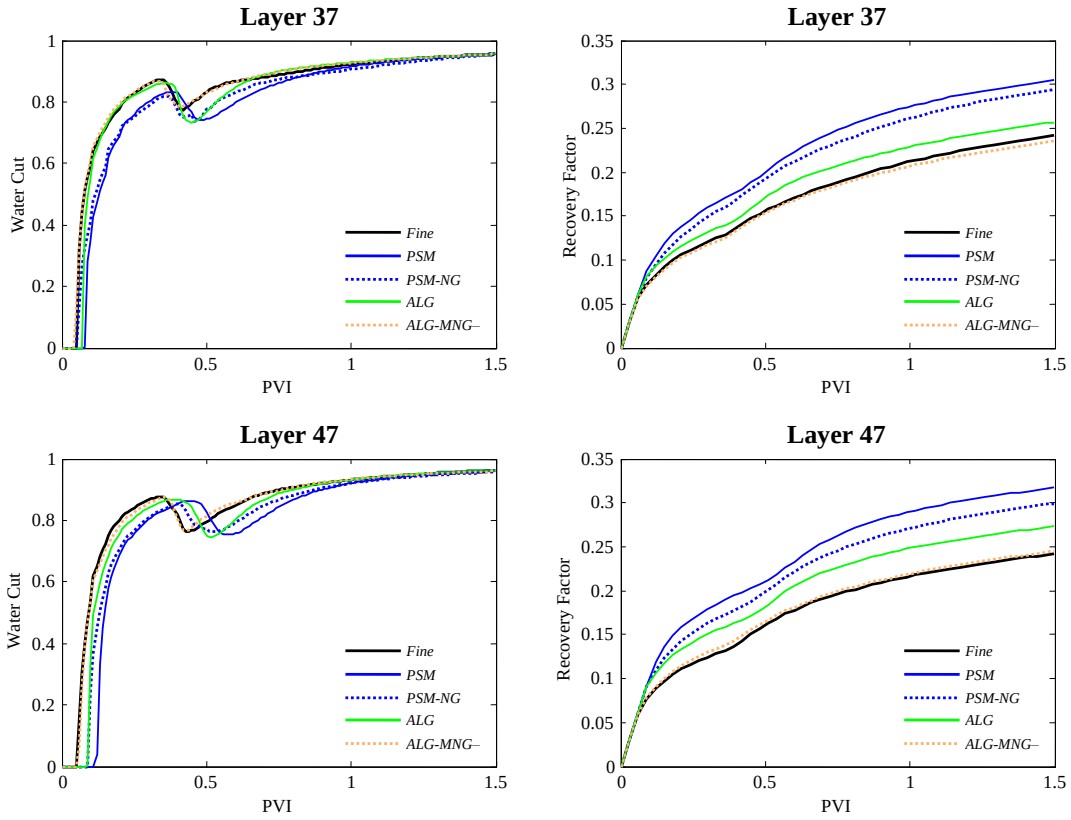

Figure 5.13: Recovery factor and water cut curves for layer 37 and layer 47 of SPE10 model for polymer flooding case.

tional flow functions, denoted by Downscaled–2 and finally one with IFM for the coarse and the SEG scheme for the fine-scale fractional flow functions denoted by Downscaled–3. The water cut curves obtained by these methods are shown in Figure 5.14**a**. In Figure 5.14**b** the saturation profiles obtained by different methods are shown at 0.35 PVI. It is clear that Downscaled-2 method has significant smeared regions around the second front.

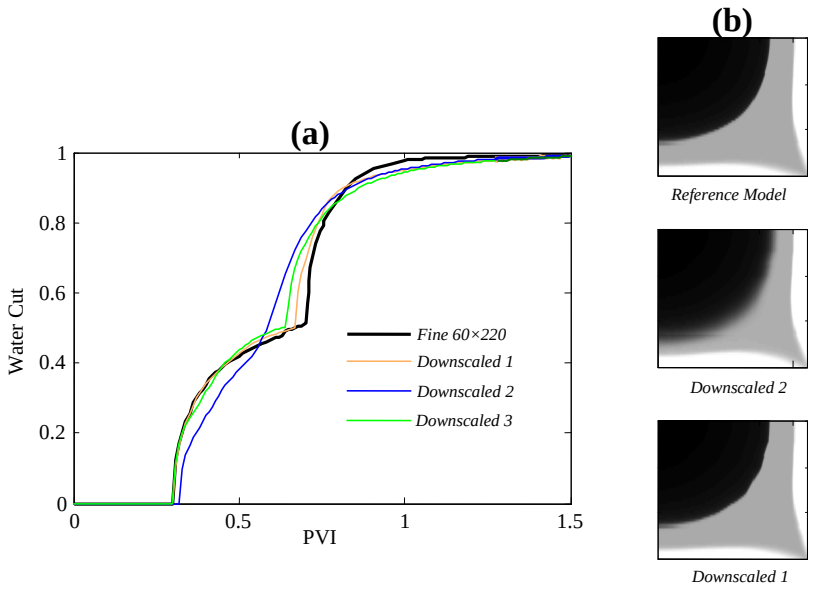

Figure 5.14: Polymer flood water cut curves with fluid properties of Example 2 on a homogeneous system (a). Saturation profiles at 0.35 PVI by three methods (b).

It is clear that Downscaled–1 matches the fine reference method reasonably well for both the first and second shocks, whereas Downscaled–2 has not resolved the second shock due to the use of a smeared fractional flow function. Downscaled–3 shows that the first shock is perfectly captured while the error for the second shock, although reduced, is not completely removed as of Downscaled–1 method.

Now, we test the methods on layers 37 and 47 for ALG-MNG−. The saturation profiles obtained by the fine reference method, Downscaled–1 (with SEG) and Downscaled–2 (with IFM) are shown in Figure 5.15. Similar to the previous observation, a reduction in numerical diffusion is seen by application of the SEG scheme.

For the water cut the general agreement between ALG-MNG− with the SEG scheme and the fine reference method is evident in Figure 5.16 as of the homogeneous case. Both methods show a flat part in the water cut curve due to the arrival and passage of

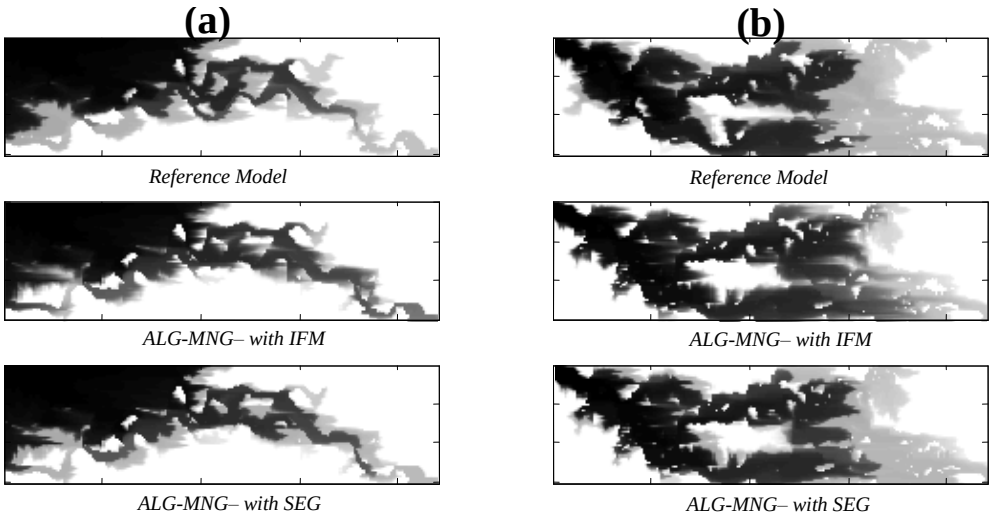

Figure 5.15: Saturation profiles for polymer flooding with three methods for layer 37 (a) and for layer 47 (b) at 0.25 PVI.

an unsmeared oil bank until the arrival of the second shock.

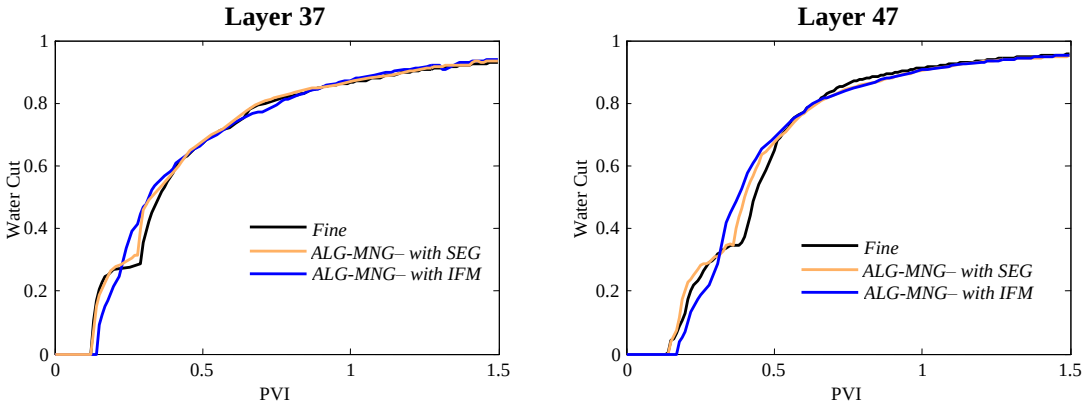

Figure 5.16: Water cut curves for polymer flooding with three methods for layer 37 and for layer 47.

Next, we use properties of Example 1 for the 3D case. The results for the homogeneous case and heterogeneous case (subsection of SPE10 model) are shown in Figure 5.17. First we note that for the homogeneous case MNG and NG are essentially identical, second, for all the methods we use the SEG scheme. It is observed that the water cut curves for the homogeneous case obtained by PSM-NG+ and ALG-NG− do not match the fine reference method. Only the ALG-NG+ matches. This observation raises the point that the secondary shock due to polymer is very sensitive to both the upscaled and down-

scaled solutions. As we observed similar sensitivity in two dimensional homogeneous case towards the SEG and IMF schemes, here the problem has wider aspects: PSM versus ALG upscaling and static versus dynamic downscaling. For the Figure 5.14, the Downscaled–1 method was actually PSM-NG+ method in Figure 5.17.

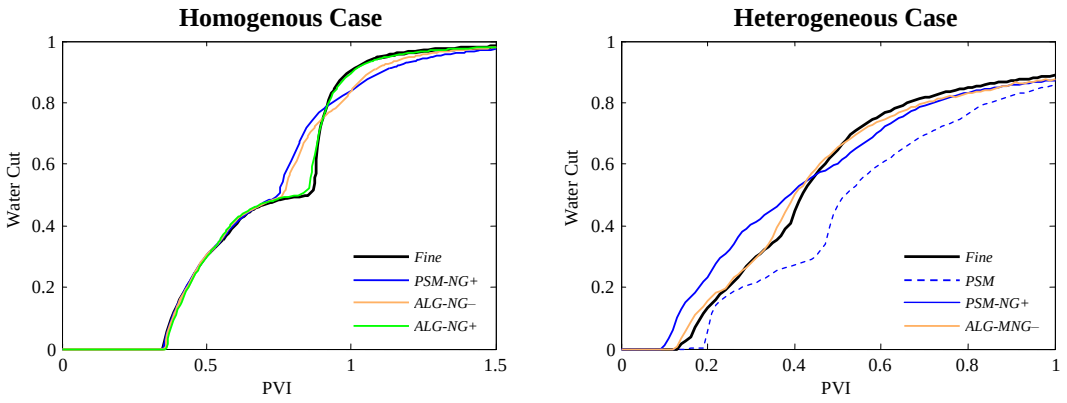

Figure 5.17: The water cut curves obtained by 3D cases for the polymer flooding.

Now here for 3D, the large secondary-shock smearing effect is eliminated by implementing ALG upscaling. The effects of solute related total mobility changes are captured in the transmissibilities by iteration (similar to a two-phase flow upscaling). Then the dynamic downscaling has been equally effective to transfer such effects to the saturation equation. The same effects are not obviously captured well by the static downscaling. This can be a major drawback. However, looking at Figure 5.17, for the heterogeneous case, we see that ALG-MNG− is performing well. This is because the heterogeneity has helped to smear the secondary shock more or less, so the sensitivity has been lowered.

From the efficiency point of view, the computational gain by the application of the static downscaling for this example is considerable. The time for the dynamic downscaling was $t_{NG+} = 291$ seconds, where as the time for the static downscaling was $t_{NG-} = 48$ seconds. Other time measurements are the fine scale pressure equation solution is $t_{fine} = 3185$, the coarse scale pressure equation solution by PSM is only $t_{PSM} = 0.3643$, the coarse scale pressure equation by ALG is $t_{ALG} = 476$, although this can still be made more efficient.

5.2.2 Surfactant and Thermal Flooding

The comparisons here are based on the rock and fluid properties used in Example 3 of the previous section for the surfactant. For the thermal flooding, in order to have a more pronounced secondary shock than the one produced by Example 4, we use,

Table 5.5: Thermal properties and densities of rock and fluids used for numerical assessment

	Porosity	Heat Capacity $(Btu/lb-F)$	Density (lb/ft^3)	α	β
Oil		38.6	77.9		
Water		41.3	82.8		
Rock	0.3	35.0	100	7.80	28.8

Table 5.6: Temperature dependent parameters (fluid viscosity) used for numerical assessment

T(F)	$\mu_o(cp)$	$\mu_w(cp)$
180 (Cold Fluid)	120.0	0.77
70 (Hot Fluid)	1.0	0.60

instead, properties given in Tables 5.5 and 5.6. The properties represent a heavy oil reservoir which reacts very favourably towards the injection of hot water.

Again, we compare recovery factor and water cut curves obtained by simulation of the surfactant and thermal flooding by different methods on two and three dimensional models. Whereas the surfactant is injected after 0.25 PVI injection of water and is continued up until 1.5 PVI, the thermal flood initiates right from the beginning to 1 PVI.

For both of the scenarios, we use only the SEG scheme for the fine and the coarse scale. For the two dimensional cases, the results of recovery factor and water cut curves are shown in Figure 5.18 and Figure 5.19. For both scenarios we observe an acceptable performance of ALG-MNG−.

For the three dimensional cases, the water cut curves are shown in Figure 5.20 and Figure 5.21. The secondary increase of the water cut in heterogeneous cases of these two plots have been significantly smeared by the heterogeneity present. In any case, homogeneous or heterogeneous, the performance of ALG-MNG− is as satisfying as before.

Finally, the saturation profiles at 1 PVI for the three methods of the fine-scale reference, PSM-NG+ and ALG-MNG− are shown in Figure 5.22.

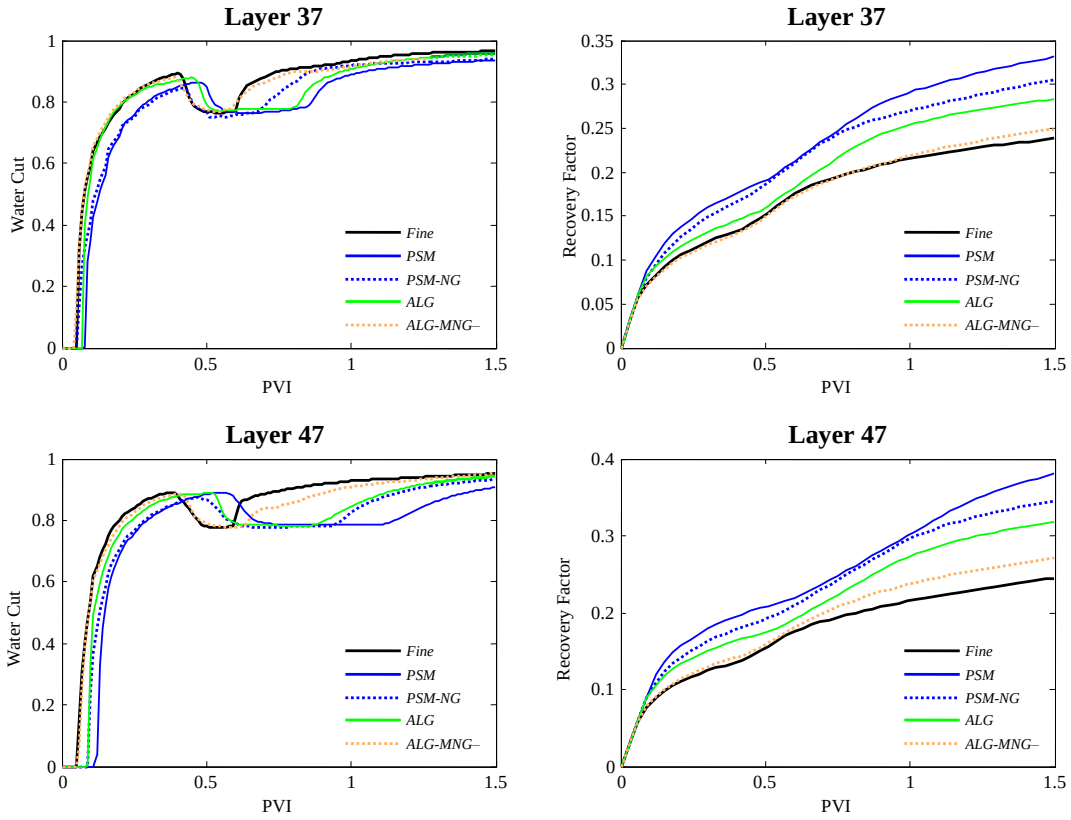

Figure 5.18: Recovery factor and water cut curves for layer 37 and layer 47 of SPE10 model for surfactant flooding case.

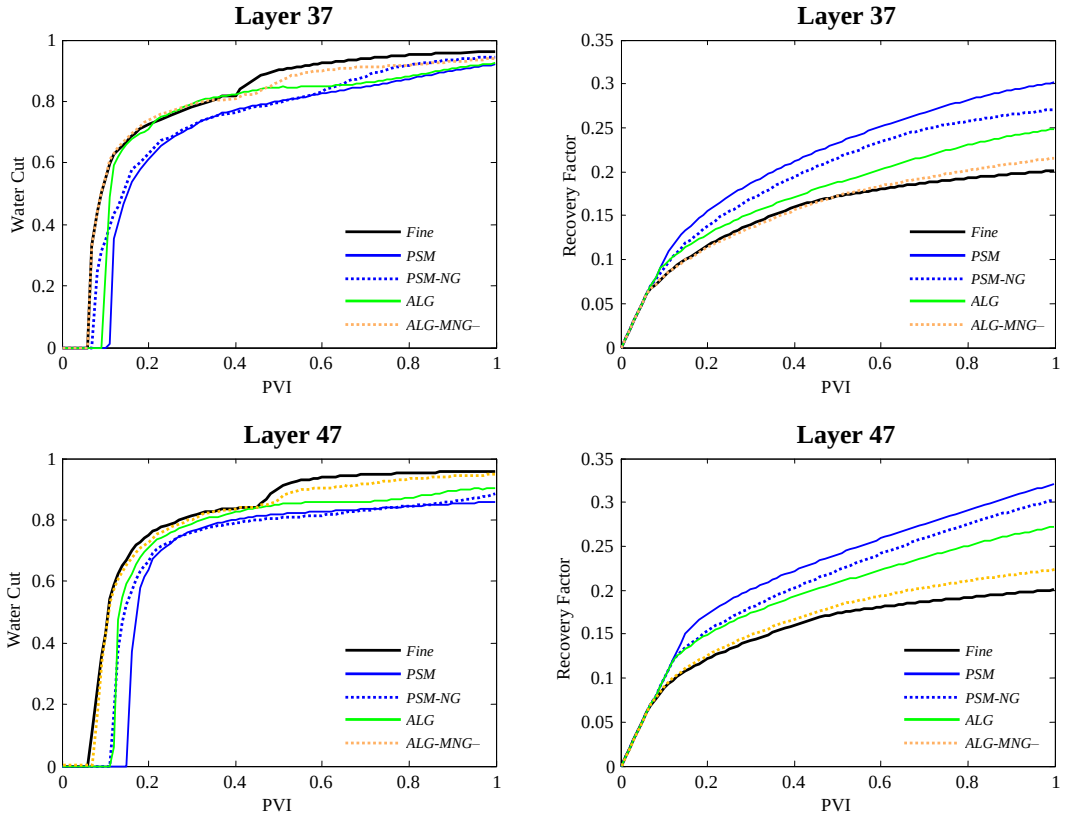

Figure 5.19: Recovery factor and water cut curves for layer 37 and layer 47 of SPE10 model for thermal flooding case.

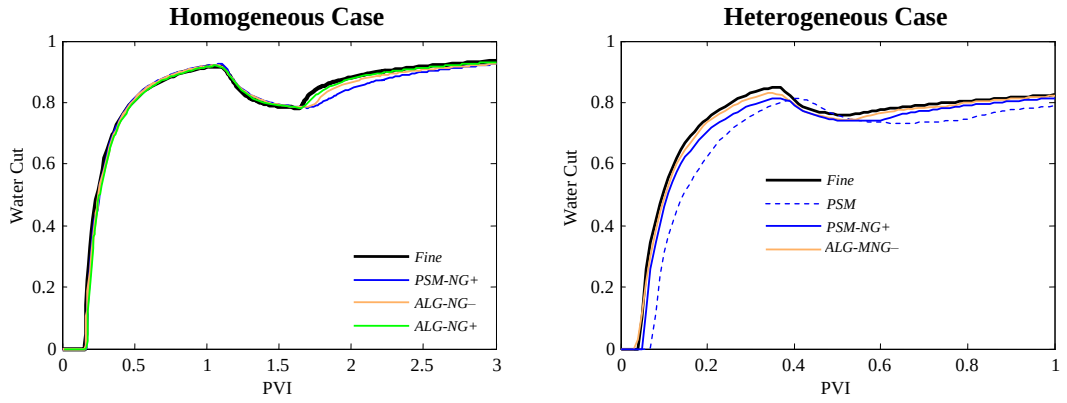

Figure 5.20: The water cut curves obtained by 3D cases for the surfactant flooding.

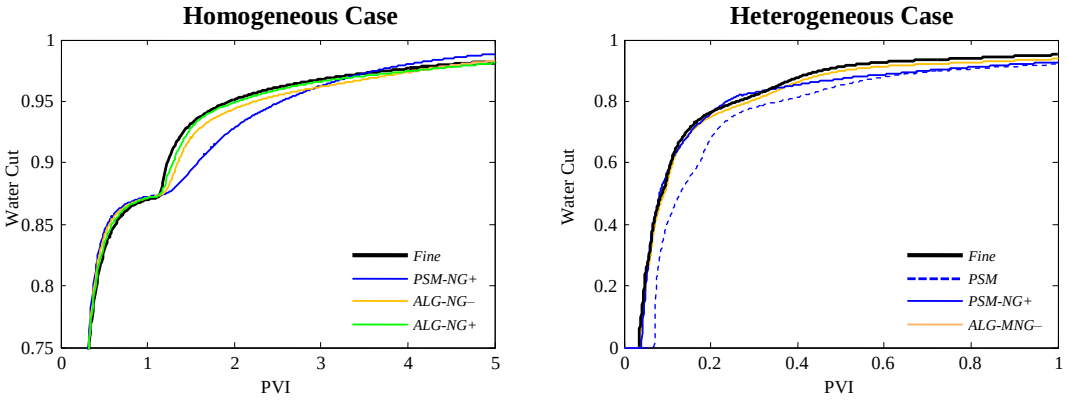

Figure 5.21: The water cut curves obtained by 3D cases for thermal flooding.

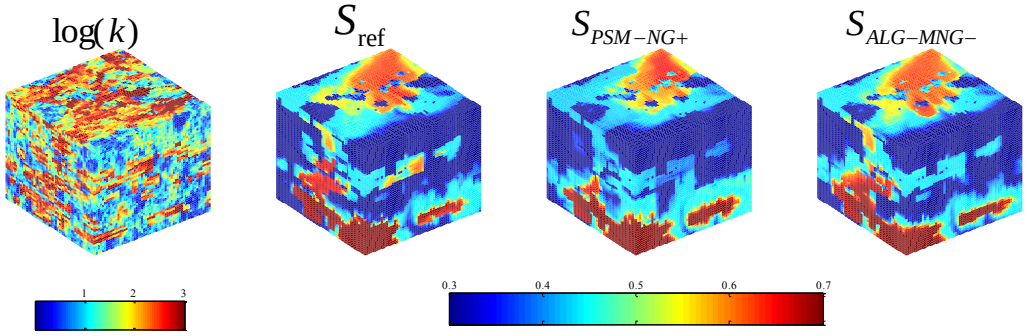

Figure 5.22: The logarithm of absolute permeability and saturation profiles for the surfactant flooding, heterogeneous 3D case at 1 PVI.

5.2.3 Summary of Results

We showed the applicability of static downscaling introduced in the previous chapter to a handful of EOR simulations. The agreement between the fine scale and the static downscaled method (ALG-MNG−) was generally reasonable for 2D and 3D systems that we tested. It is, however, a matter of investigation to judge the performance of a static downscaling method for more physically complex EOR processes and flooding scenarios.

6 Quadtree Grid Generation vs. Adaptive Local Global Upscaling

In this chapter, a non-uniform quad-tree grid generation algorithm, originally developed by Elsheikh (2007), is modified for tracer and multiphase flow in channelized heterogeneous porous media. In Section 6.1 two approaches for quad-tree grid construction will be described. In the first approach, a wavelet transformation was used to generate a refinement field based on permeability variations. The second approach uses flow information based on the solution of an initial-time fine-scale problem. In Section 6.2 the resulting grids were compared with uniform grid upscaling. For uniform upscaling, we use renormalization upscaling and local-global upscaling. The velocities obtained by non-uniformly and uniformly upscaled grids, were downscaled. This procedure allows us to separate the upscaling errors, on non-uniform and uniform grids, from the numerical diffusion errors.

Cartesian non-uniform quadtree grid generation for reservoir simulation is relatively easy to implement and requires much less bookkeeping in comparison to unstructured grids. Also, from the reservoir simulation standpoint, upscaling can be more straightforward on quadtree grid than on an unstructured grid. Permeability can be upscaled within each coarse grid block just with changing the level of upscaling. Nonetheless the main drawback of a quad-tree grid is the lack of flexibility in representing severe geometrical deformities of porous media compared to an unstructured grid. This might lead to a high number of cells around the heterogeneities.

In this chapter, we perform a critical evaluation of two different methods for quadtree grid construction based on permeability field information and flow based information. The solution on non-uniform quadtree grid is compared with uniform grid coarsening with standard upscaling and iterative local-global upscaling methods (Chen & Durlofsky, 2006). This problem differs from standard mesh adaptivity methods where the mesh is refined and coarsened based on a discretization error metric. Here, both the discretization errors and upscaling errors are present. The list of the methods used is: (1) Uniform mesh coarsening with renormalization upscaling, (2) Uniform mesh coarsening with adaptive local-global upscaling, (3) Quad-tree grid coarsening based on permeability field indicator (wavelets) with renormalization upscaling, and (4) Quad-

tree grid coarsening based on flow field indicator with renormalization upscaling. These different methods are numerically tested against heterogeneous geological models with large permeability variations. In the numerical simulations, coarse scale velocities were downscaled back to the original fine grid in order to keep the errors bound to the absolute permeability upscaling. This allows us to solve the phase saturations at the fine grid for all the methods under consideration.

In this chapter we will try to determine what is the best way to use mesh adaptivity via quad-trees combined with an upscaling method for solving multiphase flow problems in heterogeneous medium. In that pursuit, we quantify and compare the performance of non-uniform quad-tree grids to the fairly accurate adaptive local-global upscaling algorithm.

6.1 Quadtree Grid Generation

A quadtree grid consists of a set of non-uniform Cartesian cells obtained from recursive subdivision of a unit square called the root cell (de Berg *et al.*, 2000). Each cell in the quad-tree corresponds to a square and has four children and one parent. The exception is the root cell which has no parent and the leaves which have no children. Dividing a leaf cell into four is denoted as a refinement operation and merging four children cells into their parent is denoted as a coarsening operation. In the current work, each quad-tree cell is assessed based on a certain metric and if its value exceeds a minimum threshold, that cell is marked for refinement. Different refinement criteria can be used within the same adaptivity algorithm. Following the marking step, a grid regularization operation is performed to ensure that no cell has a side length more than twice the size of its neighbours. This step is called tree balancing. After finishing the marking and balancing phases, the actual refinement is done by dividing each cell into four children and updating the neighbouring relationship between the different cells.

In the context of subsurface flow modelling, as was described in Chapter 1, the criteria for generating optimal quad-trees are not always entirely clear. Subsequently, we will investigate two different strategies for marking quadtree cells for refinement; permeability based and flow based criteria. In following subsections we present a detailed description for each of these criteria.

6.1.1 Wavelet Transformation for Permeability-based Gridding

Wavelets are used here for the permeability based gridding. Wavelets have been applied successfully for grid generation on cases of high heterogeneity by Ebrahimi & Sahimi (2002, 2004) and Rasaei & Sahimi (2008b,a). The main idea is to filter the detail (or wavelet) coefficients obtained by transformation to reduce the size of data set or to eliminate fluctuations. During the thresholding, a wavelet coefficient is compared with a specified value and is set to zero if its magnitude is less than the threshold; otherwise, it is retained or modified depending on the thresholding rule. *VisuShrink* and *SureShrink* are two commonly used wavelet thresholding rules. For a signal with size n, *VisuShrink* which is also referred to as universal threshold (Donoho, 1995) is defined as:

$$t = \sigma\sqrt{2\log n}, \tag{6.1}$$

where σ is the noise level or equivalently σ^2 is the noise variance present in the signal. For practical use, when the noise level cannot be assumed to be known, it is important to estimate it. Based on the *median absolute deviation*, Donoho & Johnstone (1995)

defined an estimate of the noise level as:

$$\hat{\sigma} = \frac{\text{median}(d_{j,k})}{0.6745}, \tag{6.2}$$

where $d_{j,k}$ corresponds to the detail coefficients in the wavelet transform at scale j and position k. The value 0.6745 is used for normalization because the median absolute deviation of the detail coefficients converges to this value times the noise level as n goes to infinity. *VisuShrink* yields overly smoothed fields as it applies a global thresholding scheme where a single threshold value is applied globally to all the wavelet coefficients.

Alternatively, *SureShrink* (Donoho & Johnstone, 1995) is an adaptive threshold chooser based on the *Stein's Unbiased Risk Estimator* (SURE) (Stein, 1981). It combines the universal threshold and the SURE threshold estimator and the goal is to minimize the *mean squared error* that one can find in full mathematical detail in references like Donoho & Johnstone (1995). The thresholding employed by *SureShrink* is adaptive and level dependent, that is, a different threshold value is assigned to each resolution level in the wavelet transform. This technique is also smoothness adaptive, which means that the reconstructed image preserves the abrupt changes or boundaries in the original image.

The *SureShrink* thresholding is applied here on wavelet transformation of permeability field by utilising MATLAB built-in `rigrsure` option for threshold selection. The reconstruction of an inverse transform yields a map with similar size of the original field. If any variation is detected in the reconstructed permeability map (filtered) within a coarse grid block, that cell is marked for refinement.

6.1.2 Flow-based Gridding

For flow-based adaptivity, the refinement/coarsening indicator is based on the maximum velocity magnitude within a coarse grid. The indicator for a cell E is defined as:

$$I_E = \max_{e \in E} \{\mathbf{v}_e\} \tag{6.3}$$

where $\mathbf{v}_e$ is the cell centred velocity magnitude at a subgrid cell e inside the coarse grid cell E. The velocity magnitude is defined as

$$\mathbf{v}_e = \sqrt{\mathbf{v}_x^2 + \mathbf{v}_y^2}, \tag{6.4}$$

where $\mathbf{v}_x$ and $\mathbf{v}_y$ are the cell-centred averaged velocity values in the x and y directions, respectively. The velocity values are obtained from a single-stage calculation of fine scale velocity from solution of pressure equation with the boundary conditions of the

simulation. For example the boundary condition can be one quarter of five spot pattern or constant pressure gradient.

The quad-tree leaves are marked for refinement based on the relative value of I. In so doing, a user-defined percentile of the values of I is determined. Then all the leaf cells that have an indicator value exceeding the percentile value are marked for refinement. The velocity field is obtained by solving the fine scale problem at the initial time step. The use of percentile automates the refinement for different heterogeneous media.

We note that the use of different global boundary conditions to generate flow-based grid results in different meshes. For example, in this work, we use a corner-to-corner flow. This pattern may result in more high velocity regions than the actual simulation implicates. On the other hand the pattern may not cover high flow regions induced by other cases of boundary conditions. For such circumstances, we refer to the same implications which were discussed in flow-based non-uniform coarsening presented in Durlofsky *et al.* (1997). The authors used the pressure-flux boundary condition which sets a constant pressure gradient in one direction and no flow on the sides of the other direction. With the aforementioned implications, the authors argued that an over-determination of high flow regions is preferred to an under-determination. Furthermore, the cost of resolving for missed high flow regions is not significant either.

Here we present a step-by-step algorithm for quadtree grid generation:

1. If using wavelets, map the permeability with wavelet transformation by a filtering procedure. We used a MATLAB built-in function for this purpose (`dwt2`, which performs 2D discrete wavelet transform). However, one can use wavelet discrete transform functions developed under any other programming languages for the same filtering purpose.

2. If using flow-based gridding, first use the fine scale permeability and the specified boundary conditions, calculate the fine scale velocity field and the cell-centred magnitude of velocity based on Equation 6.4.

3. Starting with the current grid, (initially uniform 8×32), use either the filtered map of permeability or the magnitude of velocity for refinement marking step.

   The refinement for the wavelet-based quadtree grid is based on detection of variation in the permeability of constituent cells of a targeted coarse grid block because for the homogeneous coarse grid blocks, the constituent cells all have the same filtered permeability value.

   The refinement for the flow-based quadtree grid is based on ranking of the coarse grids based on magnitude of velocity. That is, first we calculate, for each coarse grid, maximum value of the magnitude of velocity of the constituent fine cells.

Then we calculate a specified percentile of the set of maximum values of the magnitude of velocity for the coarse grid blocks. Here, we decide that the coarse grid blocks with maximum value of the magnitude of velocity higher than 70th percentile are assumed to belong to high flow region and consequently are marked for refinement. We note that we also could have decided the coarse grids with maximum value of the magnitude of velocity lower than 30th percentile be marked for coarsening, however we did not implement this coarsening stage.

Also we do not allow the neighbouring cells to be refined so that the level of the refinement between them would be more than one. Therefore extra grids are marked for refinement.

4. Perform the refinements of the marked grid blocks. Each coarse grid block is refined to four smaller grids.

5. Now we have a non-uniform grid with new number of cells. We perform the stage 3 (with new refinement marking values from the new grid) until we finish the loop for the maximum number of refinement (see Figure 6.1 for the repetition of stage 3 for the layer 37 of SPE10 model).

6. With the grid obtained, we can perform renormalization algorithm at different levels to assign coarse permeabilities to each cell of the new grid.

6.1.3 Pressure Equation Discretization for *h*-Adaptive Grids

The classical finite difference discretization of the pressure equation over the interfaces γ_{ac} and γ_{bc}, as shown in Figure 6.2 is:

$$\int_{\gamma_{ac}} k\lambda_t \nabla p ds = \left(\frac{\ell_a + \ell_c}{\ell_a/k_a + \ell_c/k_c}\right) \lambda_{t,ac} \left(\frac{p_a - p_c}{\ell_a + \ell_c}\right), \tag{6.5a}$$

$$\int_{\gamma_{bc}} k\lambda_t \nabla p ds = \left(\frac{\ell_b + \ell_c}{\ell_b/k_b + \ell_c/k_c}\right) \lambda_{t,bc} \left(\frac{p_b - p_c}{\ell_b + \ell_c}\right), \tag{6.5b}$$

where ℓ_a, ℓ_b and ℓ_c are grid lengths and k_a, k_b and k_c are absolute permeabilities of cells a, b and c. The use of classical cell centred discretization results in a local leading truncation error of *O(1/h)* when applied to h-adaptive grids with local refinement (Quandalle & Besset, 1985; Forsyth & Sammon, 1986). This is attributed to the non-aligned flux vectors as shown in Figure 6.2. Therefore, extra care is needed when calculating the transmissibility at the interface of fine/coarse grid.

Edwards (1996a) provided a consistent discretization method to deal with the interface between differing grid levels. This scheme utilizes an extended stencil around the

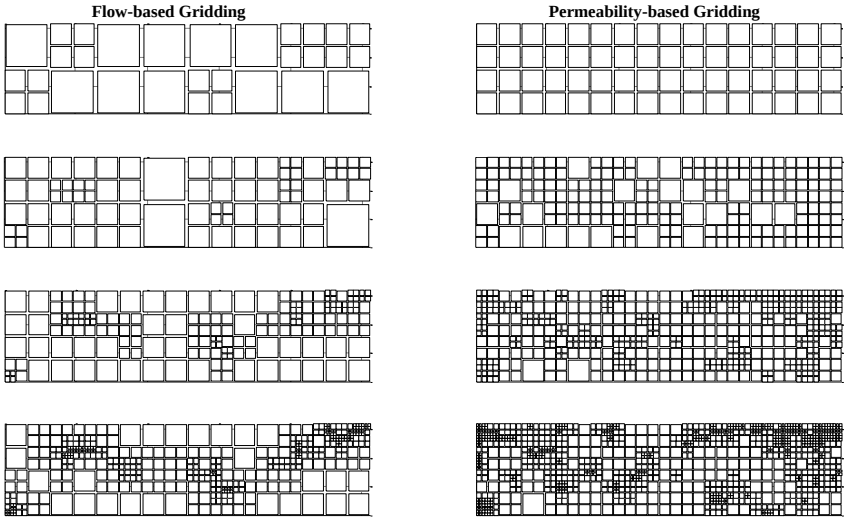

Figure 6.1: Step by step construction of flow-based and permeability-based grids for layer 37 of SPE10 model from an 8×32 uniform coarse grid (not shown) to the last non-uniform quadtree grid. We imposed the layer with two wells at the lower left and upper right corners. We note that for the permeability-based gridding, we added the position of wells to the criteria of refinements.

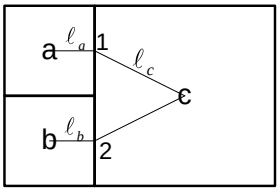

Figure 6.2: An illustration of fine/coarse grid interface.

interface derived by flux and pressure continuity. It also produces a symmetric, positive definite and diagonally dominant matrix of coefficients. First, it considers mean pressures at 1 and 2. To preserve local conservation over the resulting triangle 1,2,c (see Figure 6.2) the fluxes on the left-hand side of faces 1 and 2 are equated to the flux on the right-hand side. This results in two equations for the two mean face pressures p_1 and p_2, respectively,

$$k_a \frac{p_1 - p_a}{h} = k_c \frac{p_c - (p_1 + p_2)/2}{2h}, \tag{6.6a}$$

$$k_a \frac{p_2 - p_b}{h} = k_c \frac{p_c - (p_1 + p_2)/2}{2h}, \tag{6.6b}$$

where (h_x, h_y) are dimensions of the finer cell (a or b). Eliminating p_1 and p_2 in terms of p_a , p_b and p_c yields a flux that changes Equation 6.5b to:

$$\int_{\gamma_{ac}} k\nabla p ds = \int_{\gamma_{bc}} k\nabla p ds = 4\frac{h_y}{h_x}\left(\frac{k_a k_b k_c}{4k_a k_b + k_a k_c + k_b k_c}\right)\left(p_c - \frac{(p_a + p_b)}{2}\right). \tag{6.7}$$

6.2 Numerical Results, Comparisons and Discussions

The simulations were performed on the following models:

1. Two uniform coarse grid models (256 cells: coarsening level 1 and 1024 cells: coarsening level 2) with upscaled permeabilities obtained by renormalization method. We denote these models by RM with 256 cells and RM with 1024 cells.

2. Two uniform coarse grid models (256 cells and 1024 cells) with transmissibilities obtained by adaptive local-global upscaling method. We denote these models by ALG with 256 cells and ALG with 1024 cells.

3. Two models of permeability based quadtree grid (coarsening levels 1 and 2, obtained by different numbers of refinement loops), with the permeabilities of coarse grids obtained by renormalization. These models are denoted by k-QG followed by the number of cells in each model.

4. Two models of flow based quadtree grid, with permeabilities of coarse grids obtained by renormalization. These models are denoted by q-QG followed by the number of cells in each model.

For the assessment of each model, a comparison to the fine scale reference solution is performed. The following error measures are considered:

1. The saturation error as of Equation 4.25. Further, we calculate a relative error for RM, q-QG and k-QG compared to ALG by

$$\epsilon_r(s) = \frac{\delta(s)_l \times N_l}{\delta(s)_{ALG} \times N_{ALG}}, \tag{6.8}$$

   where l=RM, q-QG and k-QG and N is the number of cells in each model. Assuming that error reduces linearly with larger number of cells, this value represents an approximate estimation of accuracy of each method compared to ALG in terms of quality of saturation profile.

2. The reconstructed velocity error as of Equation 4.26. Similar to saturation, we calculate a relative error for RM, q-QG and k-QG compared to ALG by

$$\epsilon_r(v) = \frac{\delta(v)_l \times N_l}{\delta(v)_{ALG} \times N_{ALG}}, \tag{6.9}$$

   where l=RM, q-QG and k-QG and N is the number of cells in each model.

3. The water cut curves.

4. The $Q_o/\Delta P$ curves.

For all the models, the pressure equation is solved on a coarse grid and the velocity is downscaled by a uniform grid or non-uniform grid nested gridding procedure. The saturation is then calculated on the original fine scale grid. This assures that the upscaling errors are separated from numerical diffusion error arising from coarse representation of saturation. For boundary and well conditions we assume a source (constant injection flow rate) and a sink (constant bottom-hole pressure production), respectively on the lower left and the upper right corners of the system. This configuration will induce a corner to corner flow. A no flow boundary condition is applied on the domain outer boundaries.

6.2.1 Tracer Flow

Here, we perform simulations on smoothly heterogeneous layer 10 and two very channelized layers 37 and 47 of SPE10 model. Layer 10 shown in Figure 6.3**(a)** is selected to investigate how different methods perform at moderately heterogeneous medium. The constructed grids and saturation profiles are shown in Figure 6.3. From wavelet filtered permeability map shown in Figure 6.3**(c)**, we observe that regions of high permeability are not filtered out by the wavelet transform. It is also observed that the fine scale velocity and the reconstructed velocities resulted in a similar saturation fields at t =0.6 PVI. Further, the uniform grid upscaling and QG models yielded almost identical water cut curves (shown in Fig. 6.4) that match the fine scale results. The match is complete in cases of ALG and q-QG models and is very reasonable for RM and k-QG models. This assures that the downscaling effectively eliminated the diffusion error in all coarse and non-uniform grid models.

Next, the channelized layers 37 and 47 are examined. The constructed grids and saturation profiles at t=0.6 PVI for layer 37 and 47 are shown in Figure 6.5 and Figure 6.6, respectively. Additionally, the saturation profiles obtained form downscaling of ALG and RM are shown for comparison. Continuing the simulations till t=1.2 PVI, we obtain $\delta(s)$ and $\epsilon_r(s)$ for layers 37 and 47 which are reported in Tables 6.1 and 6.2. In the same tables we reported $\delta(v)$ and $\epsilon_r(v)$.

From the tables we draw the following points. First, neither k-QG or q-QG have achieved as low global error norms as produced by ALG. The two k-QG models show minimal improvements in $\delta(s)$ and $\delta(v)$, if any, in comparison to uniform RM. Regarding the number of cells, $\epsilon_r(s)$ and $\epsilon_r(v)$ for k-QG are considerably higher than those of RM, showing that addition of cells has not been effective at all. For q-QG, coarsening level 1, resulted in lower values of $\delta(s)$ and $\delta(v)$ compared to RM with 256 cells. However, the degree of reduction is not emphatic and the values of $\epsilon_r(s)$ and $\epsilon_r(v)$ are higher than

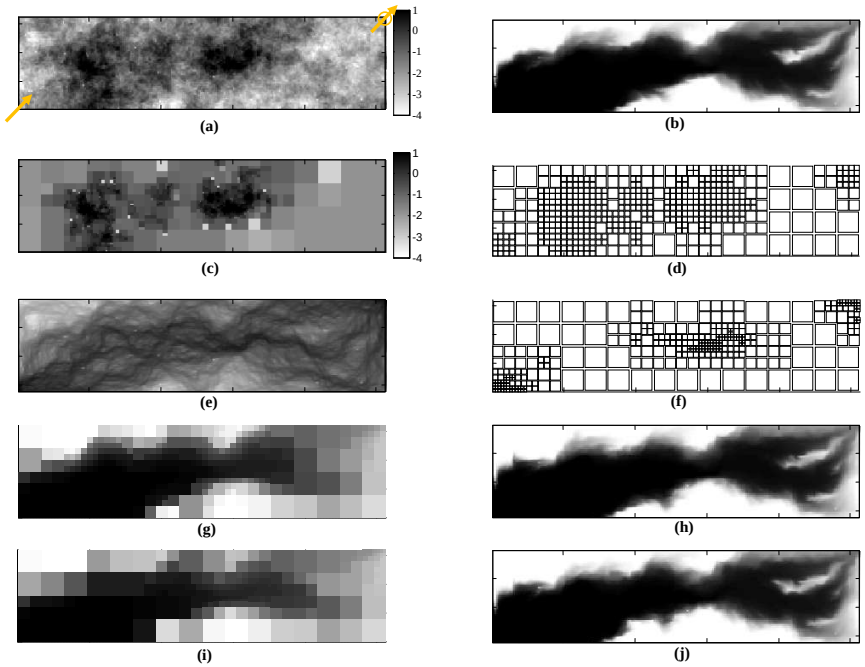

Figure 6.3: Layer 10 tracer flow simulation. **(a)** Layer 10's original fine scale permeability, **(b)** fine scale saturation at 0.6 PVI, **(c)** the filtered permeability obtained by wavelet transformation, **(d)** k-QG model constructed based on (c), **(e)** logarithm of cell-centred velocity magnitude, **(f)** q-QG model constructed based on (e), **(g)** coarse saturation solution at 0.6 PVI for k-QG, **(h)** fine saturation solution at 0.6 PVI obtained by use of velocity reconstructed from k-QG, **(i)** coarse saturation solution at 0.6 PVI for q-QG, **(j)** fine saturation solution at 0.6 PVI obtained by use of velocity reconstructed from q-QG.

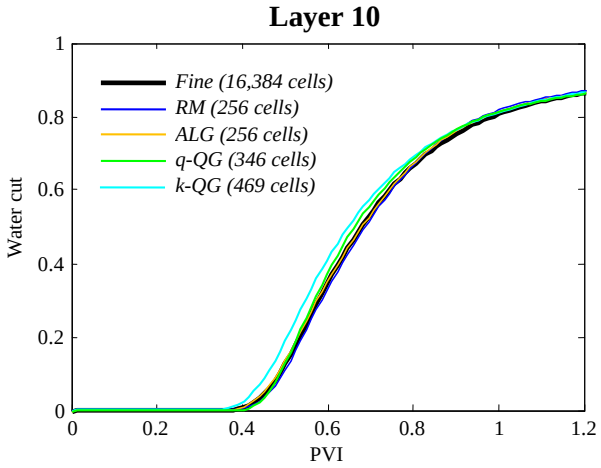

Figure 6.4: Water cut curves obtained by different models for layer 10 tracer flow simulation.

Table 6.1: The saturation and velocity errors for layer 37 tracer flow simulation.

Error	RM 256 c	RM 1024 c	ALG 256 c	ALG 1024 c	q-QG 403 c	q-QG 847 c	k-QG 508 c	k-QG 1066 c
$\delta(s)$	0.31	0.22	0.16	0.09	0.29	0.22	0.28	0.25
$\epsilon_r(s)$	1.97	2.51	-	-	2.88	2.05	3.51	2.89
$\delta(v)$	1.12	0.96	0.51	0.32	0.95	0.75	1.00	0.90
$\epsilon_r(v)$	2.21	3.05	-	-	2.93	1.97	3.91	2.97

those of RM with 256 cells. Similar trends are observed for layer 47 with the exception of the $\epsilon_r(v)$ value. On the other hand, q-QG, coarsening level 2, produced $\epsilon_r(s)$ and $\epsilon_r(v)$ that are around the same range of RM with 1024 cells, with only 0.625 of the total number of cells. Consequently $\epsilon_r(s)$ and $\epsilon_r(v)$ for this model is lower than RM with 1024 cells.

In terms of locally measured quantities, the water cut curves are depicted in Figure 6.7 and Figure 6.8 for layers 37 and 47 at two coarsening levels. Apart form layer 47 at coarsening level 1, q-QG is performing very similar to ALG. Even for layer 47, coarsening level 1, the breakthrough time and early time water cut are in good agreement with the fine scale solution and ALG model. For k-QG models, the curves are identical to RM curves and no improvement in the quality of the solution is observed by increasing the number of cells.

For the same set of conditions, $Q_o/\Delta P$ versus PVI are depicted in Figure 6.9 and Figure 6.10. The interaction of oil flow rate and pressure difference errors for this quantity, yields a mixed ranking between q-QG and ALG before and after breakthrough time.

Table 6.2: The saturation and velocity errors for layer 47 tracer flow simulation.

Error	RM 256 c	RM 1024 c	ALG 256 c	ALG 1024 c	q-QG 304 c	q-QG 640 c	k-QG 583 c	k-QG 1363 c
$\delta(s)$	0.45	0.32	0.20	0.10	0.44	0.38	0.42	0.38
$\epsilon_r(s)$	2.19	3.17	-	-	2.56	2.32	4.71	4.968
$\delta(v)$	1.29	0.78	0.45	0.29	0.98	0.81	0.97	0.85
$\epsilon_r(v)$	2.8	2.66	-	-	2.57	1.71	4.89	3.83

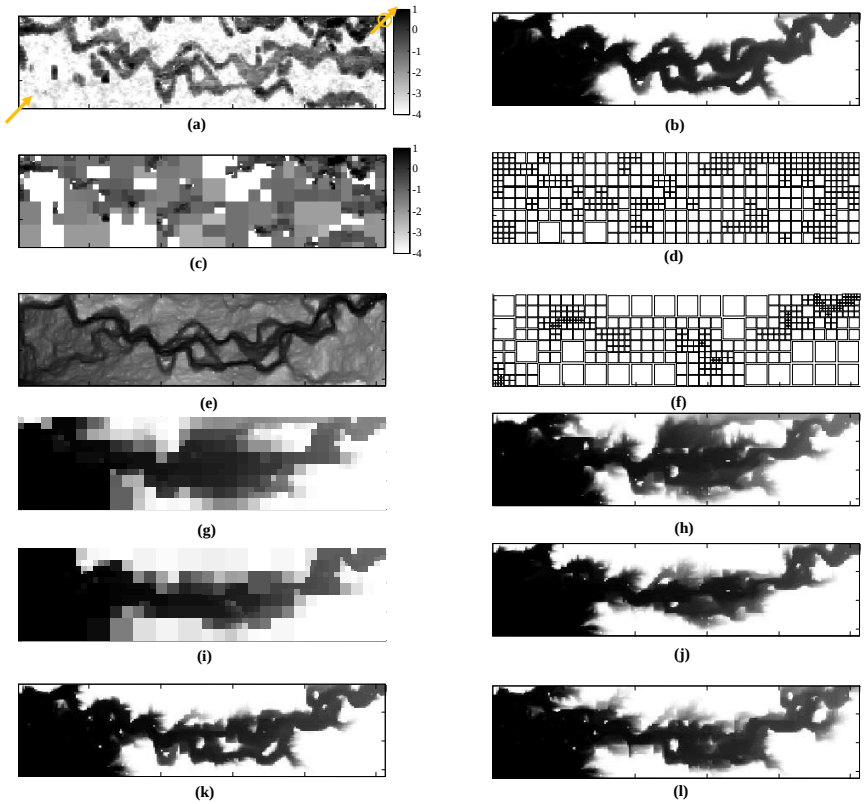

Figure 6.5: Layer 37 tracer flow simulation. **(a)** Layer 37's original fine scale permeability, **(b)** fine scale saturation at 0.6 PVI, **(c)** the filtered permeability obtained by wavelet transformation, **(d)** k-QG model constructed based on (c), **(e)** logarithm of cell-centred velocity magnitude, **(f)** q-QG model constructed based on (e), **(g)** coarse saturation solution at 0.6 PVI for k-QG, **(h)** fine saturation solution at 0.6 PVI obtained by use of velocity reconstructed from k-QG, **(i)** coarse saturation solution at 0.6 PVI for q-QG, **(j)** fine saturation solution at 0.6 PVI obtained by use of velocity reconstructed from q-QG, **(k)** the saturation profile at 0.6 PVI from ALG and **(l)** the saturation profile at 0.6 PVI from RM.

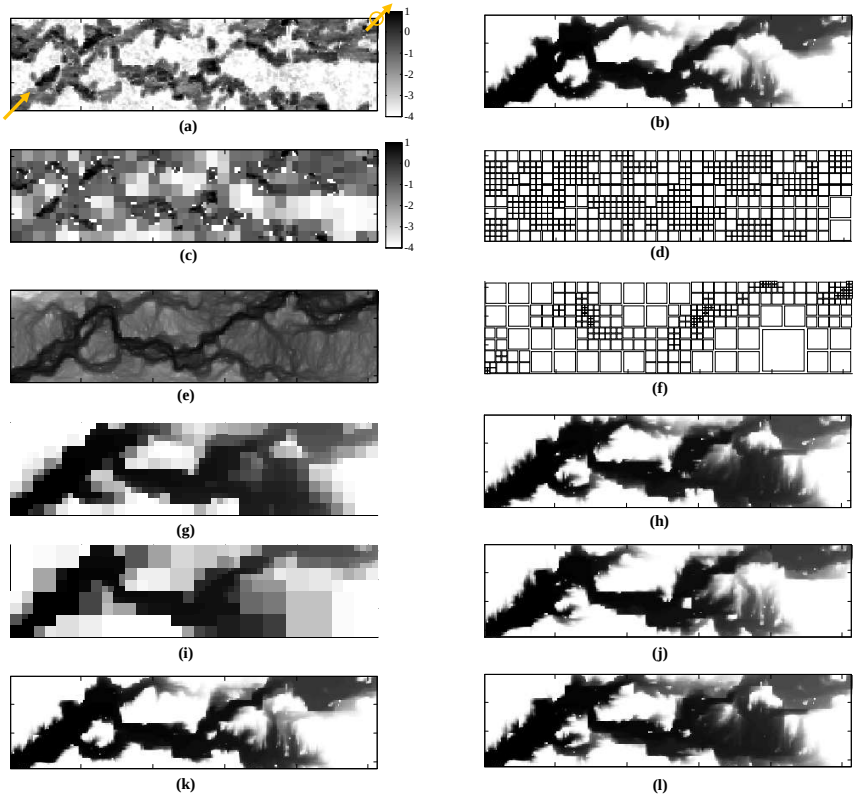

Figure 6.6: Layer 47 tracer flow simulation. **(a)** Layer 37's original fine scale permeability, **(b)** fine scale saturation at 0.6 PVI, **(c)** the filtered permeability obtained by wavelet transformation, **(d)** k-QG model constructed based on (c), **(e)** logarithm of cell-centred velocity magnitude, **(f)** q-QG model constructed based on (e), **(g)** coarse saturation solution at 0.6 PVI for k-QG, **(h)** fine saturation solution at 0.6 PVI obtained by use of velocity reconstructed from k-QG, **(i)** coarse saturation solution at 0.6 PVI for q-QG, **(j)** fine saturation solution at 0.6 PVI obtained by use of velocity reconstructed from q-QG, **(k)** the saturation profile at 0.6 PVI from ALG and **(l)** the saturation profile at 0.6 PVI from RM.

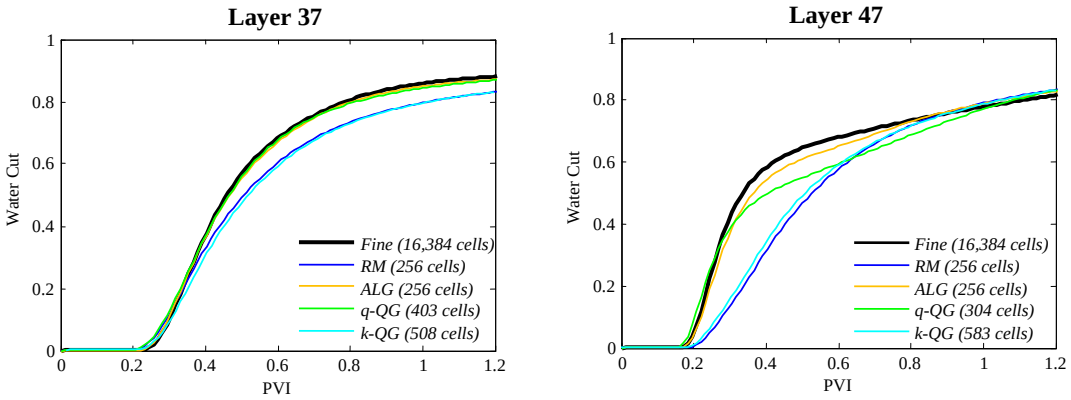

Figure 6.7: Water cut curves obtained by different models for layers 37 and 47 tracer flow simulation at coarsening level 1.

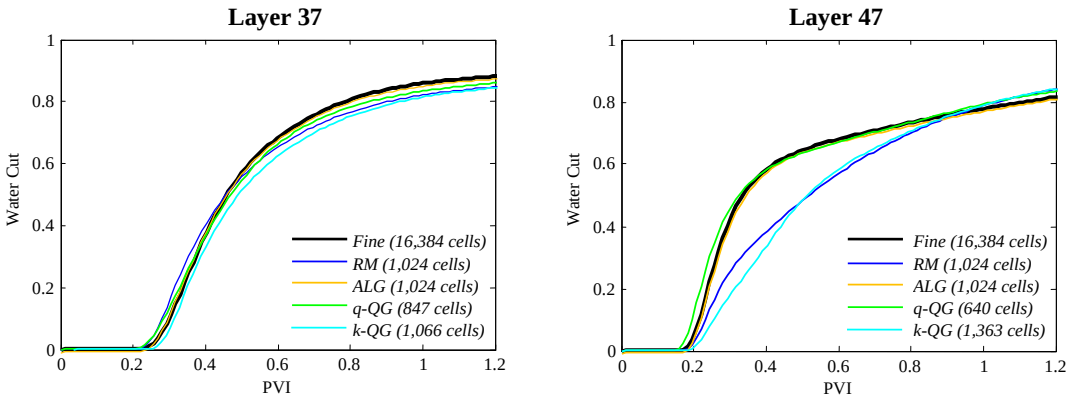

Figure 6.8: Water cut curves obtained by different models for layers 37 and 47 tracer flow simulation at coarsening level 2.

We observe a better performance by ALG initially then the q-QG curves are clearly closer to the fine scale solution. This can be attributed to the coarse scale measurement of the oil flow rate and the additional number of cells around the production gridblock in q-QG model compared to ALG model. However, both methods reasonably match the reference $Q_o/\Delta P$ values at the final time. On the other hand, the curves obtained by RM and k-QG show clear deviation from the fine scale reference curves. Hence, by the use of k-QG models, the discrepancy between the obtained results and fine scale reference solutions is evident in both the water cut and the $Q_o/\Delta P$ curves.

The comparison of curves above show almost the same level of accuracy obtained by q-QG and ALG. In other words, for locally measured quantities estimated at the production gridblock, q-QG models produce the same solution quality as of the iterative procedure of ALG method. The channelized flow patterns are *effectively* captured from injection to production points by a flow-adapted grid. However, this has not been exactly the case for globally measured error norms shown in Tables 6.1 and 6.2. This can be attributed to a slight deviation in the location of high flow region in the q-QG model in comparison to ALG and the reference model, and the error norm sensitivity to these slight dislocations. The spatial discrepancy, while not undermining the water cut and $Q_o/\Delta P$ prediction, has increased global error norms. Certainly application of an iterative local-global adjustment technique, similar to Gerritsen & Lambers (2008), can improve the results of a flow-based quadtree grids, albeit with considerable computational expenses.

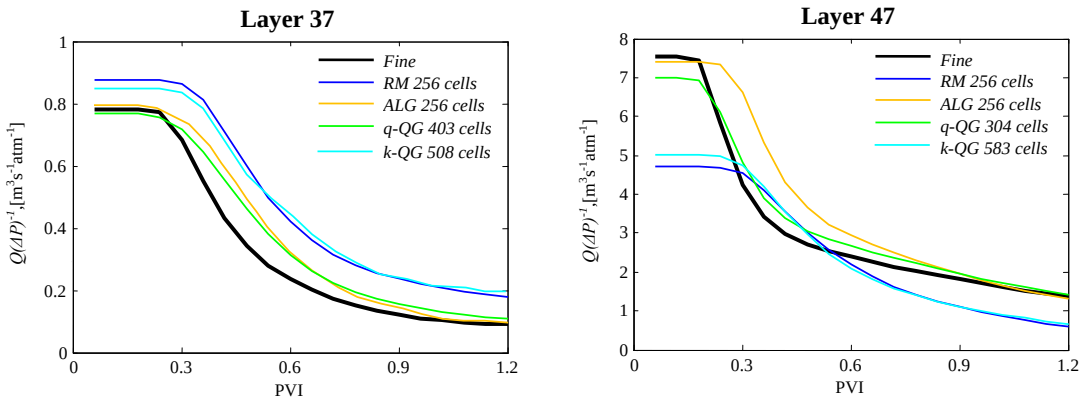

Figure 6.9: $Q_o/\Delta P$ obtained by different models for layers 37 and 47 tracer flow simulation at coarsening level 1.

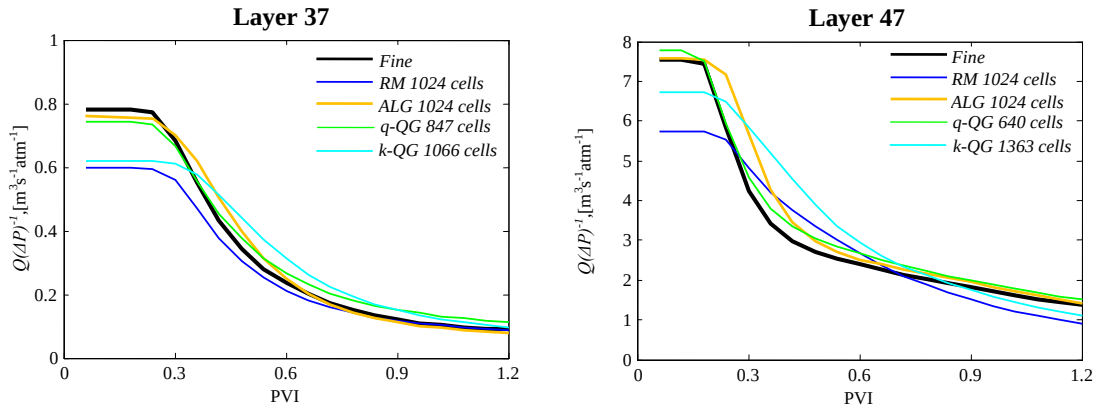

Figure 6.10: $Q_o/\Delta P$ obtained by different models for layers 37 and 47 tracer flow simulation at coarsening level 2.

Table 6.3: The saturation error for layer 37 multiphase flow simulation.

Error	RM 256 c	RM 1024 c	ALG 256 c	ALG 1024 c	q-QG 403 c	q-QG 847 c	k-QG 508 c	k-QG 1066 c
$\delta(s)_{M=0.1}$	0.36	0.28	0.25	0.16	0.34	0.29	0.32	0.29
$\epsilon_r(s)_{M=0.1}$	1.44	1.80	-	-	2.14	1.54	2.56	1.96
$\delta(s)_{M=10}$	0.30	0.21	0.19	0.11	0.28	0.22	0.28	0.24
$\epsilon_r(s)_{M=10}$	1.59	2.01	-	-	2.28	1.72	2.83	2.34

6.2.2 Multiphase Flow

In order to assess the quality of solutions on non-uniform grids in multiphase case, the same simulations with non-linear flow function are performed on layers 37 and 47. In Tables 6.3 and 6.4, the saturation errors are reported. Performing the simulation till 1.2 PVI, similar to the tracer flow case, we observe reasonable performance of q-QG models, coarsening level 2, in terms of $\epsilon_r(s)$, either for $M = 0.1$ or $M = 10$. Other observations are similar to the tracer flow simulation. The good performance of q-QG and relatively poor quality solutions obtained by k-QG, are clear.

Table 6.4: The saturation errors for layer 47 multiphase flow simulation.

Error	RM 256 c	RM 1024 c	ALG 256 c	ALG 1024 c	q-QG 304 c	q-QG 640 c	k-QG 583 c	k-QG 1363 c
$\delta(s)_{M=0.1}$	0.43	0.29	0.28	0.18	0.41	0.37	0.38	0.31
$\epsilon_r(s)_{M=0.1}$	1.54	1.61	-	-	1.72	1.31	3.07	2.34
$\delta(s)_{M=10}$	0.43	0.32	0.23	0.12	0.42	0.35	0.41	0.36
$\epsilon_r(s)_{M=10}$	1.93	2.65	-	-	2.21	1.82	4.15	4.07

Figure 6.11 shows water cut curves obtained by different models (at coarsening level 1) for multiphase case for layers 37 and 47. The general observation here is that, for $M = 10$ case, q-QG stands in the middle of the ALG curves and RM, k-QG curves. The accuracy is not as of the tracer flow case, however, the breakthrough time has been reasonably matched for both layers. On the contrary, for the case of $M = 0.1$, the breakthrough time is not that predicted by the fine scale reference solution and ALG model. This can be attributed to the sharp increase of saturation within a small spatial distance due to piston-like movement of the front. In such case, the water cut curves are more sensitive to saturation at the production cell. Such sensitivity is captured effectively by ALG model but not as much effectively by q-QG models. For $M = 10$, the physical dispersion and gradual increase of saturation and water cut at production cell, have provided a suitable condition for q-QG model. The k-QG model is results in relatively poor quality solutions similar to RM.

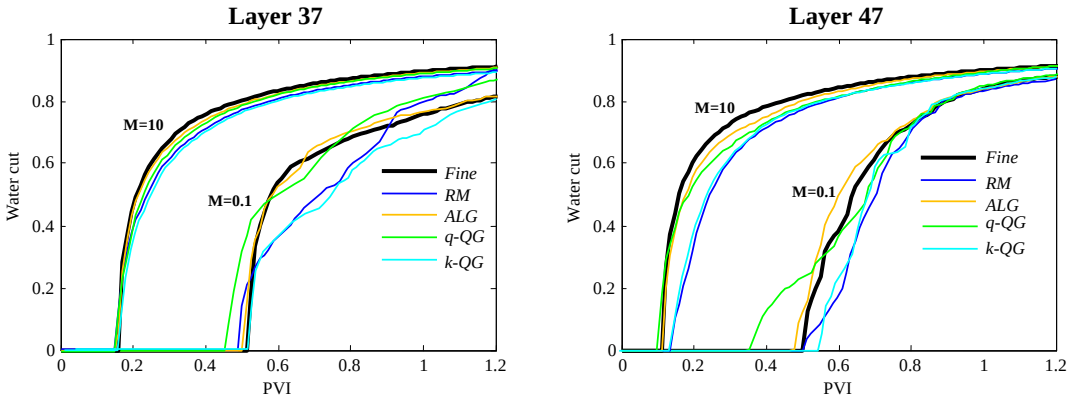

Figure 6.11: Comparisons of water cut curves measured at production cell by different models for layers 37 and 47, coarsening level 1, for multiphase simulation.

In Figure 6.12 we have shown $Q_o/\Delta P$ for layer 37, coarsening level 1, $M = 0.1$ and $M = 10$. Similar to the water cut curves, for $M = 10$ case, q-QG is very comparable to ALG. For $M = 0.1$ case we observe a considerable discrepancy with the fine scale model. For the multiphase case, the general outcome of simulation by q-QG, for global error norms is similar to the tracer flow case, but for the water cut and $Q_o/\Delta P$, the results are not as strong as the tracer flow case.

6.2.3 Presence of Shale in Porous Media

In the previous subsections, we studied several subsurface flow problems representing fluvial channels and high permeability flow-paths that create problems for upscaling.

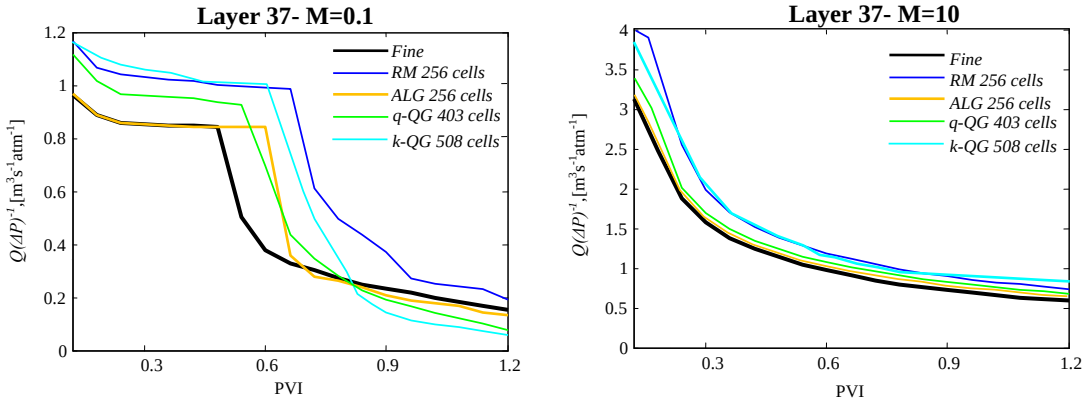

Figure 6.12: Comparisons of $Q_o/\Delta P$ for multiphase simulation for layer 37, coarsening level 1, left $M = 0.1$ and right $M = 10$.

In this subsection, we study problems where flow barriers in the form of shales with very low permeability are present. These flow barriers can also be problematic for upscaling. For example, renormalization upscaling treats shales imprecisely and results in a misjudgement of the reservoir connectivity. Typically, shales have a large aspect ratio and they can be distributed against the flow direction.

Moreover, the presence of flow barriers might be problematic for velocity reconstruction. Aarnes *et al.* (2006), for example, have shown that for a barrier that is stretched beyond a coarse scale gridblock, the boundary conditions interpolated form coarse velocities in multiscale method represent erroneous assumptions that may produce an unnatural amount of flow through the barrier. That is, the barrier is totally or partially ignored by the reconstructed velocity field. In the downscaling algorithm used here, also a particular position of shale is a source of error: the shale is stretching out of the coarse grid boundaries so that the tail or head of the shale is not situated either inside the coarse grid or over the boundaries.

Here, we examine non-uniform grid models on a synthetic permeability model populated with a few barriers located against a diagonal corner-to-corner flow as shown in Figure 6.13**(a)**. The model consists of a 128×128 grid with unit permeability everywhere except in shale streaks where it is 10^{-10} Darcy. The permeability and flow based quadtree grids are shown in Figure 6.13**(d)** and **(f)**, respectively. We note that, because the streaks of shale are the only feature in the porous medium, the wavelet filtered map is essentially identical to the original map. Henceforth, the k-QG grid is adapted to refine around the shales. In contrast, for q-QG construction, shale offers zero flow, hence they are completely ignored in the adapted grid.

Tracer flow simulations are performed on two levels of uniform upscaling by RM and

Table 6.5: The saturation and velocity errors for shale tracer flow simulation.

Error	RM 256 c	RM 1024 c	ALG 256 c	ALG 1024 c	q-QG 487 c	q-QG 958 c	k-QG 511 c	k-QG 1231 c
$\delta(s)$	0.36	0.21	0.25	0.10	0.47	0.46	0.21	0.11
$\delta(v)$	0.72	0.53	0.52	0.29	1.02	0.97	0.53	0.39
$\epsilon_r(s)$	1.41	2.08	-	-	3.55	4.45	1.70	1.39
$\epsilon_r(v)$	1.38	1.78	-	-	3.71	3.09	2.03	1.60

ALG (again $16 \times 16 = 256$ and $32 \times 32 = 1024$ cells) and two models for each of q-QG and k-QG. First, in Table 6.5 the velocity and saturation errors are reported. Here we observe an interchange between k-QG and q-QG ranking, in terms of error norms.

Figure 6.14 shows the water cut curves obtained by the different models and for different levels of coarsening. Similar to error norms, the curves obtained by k-QG are very reasonable. In fact, not only does k-QG performs better than q-QG and RM at coarsening level 1, it even outperforms ALG at this level. For this case, the poor performance of ALG, can be attributed to the lack of high flux over the interface and the block-to-block pressure drop due to the presence of shale. This factor diminishes the chance of transmissibility correction by an iterative procedure.

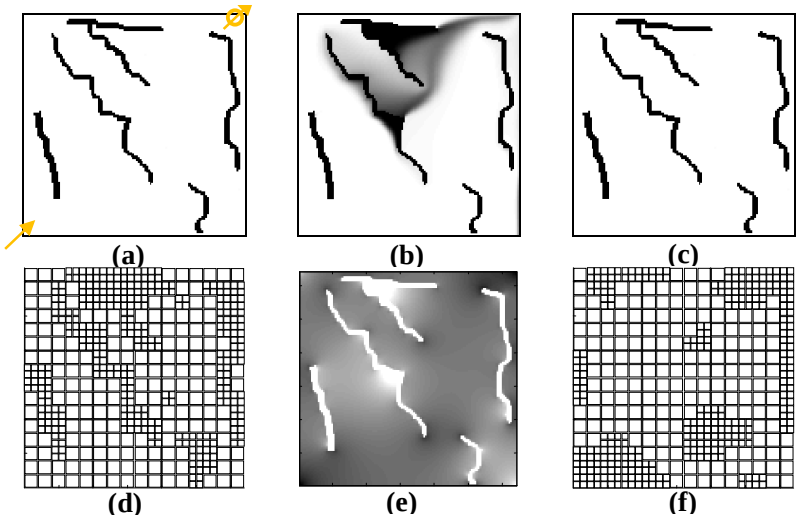

Figure 6.13: Shale tracer flow simulation, **(a)** permeability field for shale system, shales are shown in black, **(b)** the fine scale saturation profile at t=1.2 PVI, water is shown in white and oil in black, **(c)** wavelet transformation-based filtered permeability, **(d)** wavelet-based k-QG with 511 cells, **(e)** Euclidean norm of cell-centered velocity averages and **(f)** flow-based q-QG with 487 cells.

Figure 6.15 shows the saturation profiles obtained by the different models at the end of

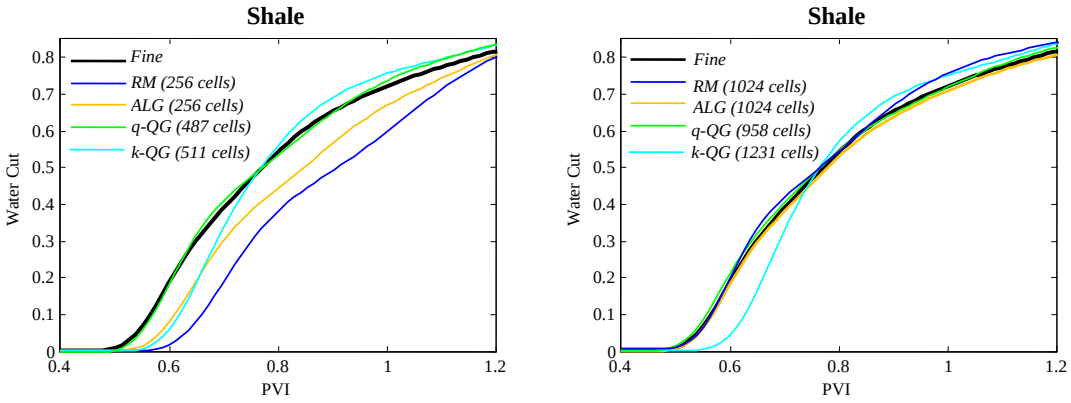

Figure 6.14: Water cut curves obtained by different models for shale system. Left is comparison of curves at coarsening level 1 with the fine scale reference model, while right is for the coarsening level 2.

simulation. These figures should be compared to the fine scale reference solution shown in Figure 6.13**(b)**. Clearly, k-QG with 511 cells are closer to the fine scale solution than q-QG with 487 cells, RM with 256 cells or ALG with 256 cells. At coarsening level 2, ALG with 1024 cells and k-QG with 1231 cells, corrected the errors of RM with 1024 cells around shales. Furthermore, not only q-QG with 487 cells produced poor quality results, but also adding more cells has shown no improvement in the quality of results as shown for the case of q-QG with 958 cells. These results showed that flow based adaptivity as done in q-QG might perform poorly in the presence of shale. We conclude that relying on flow information only and ignoring predominant heterogeneity features, like barriers, can lead to significant errors by grid adaptivity methods. In the next subsection we add a heuristic criterion to q-QG to account for the presence of flow barriers.

6.2.4 Combined Heterogeneities and Shale

In this subsection we examine a medium consisting of both channelized heterogeneities and few flow barriers. Figure 6.16**(a)** shows the fine scale permeability field used. This field is an overlay of few flow barriers on the layer 37 of the SPE10 model. These barriers are cutting the high flow regions of the model. Figure 6.16**(b)** shows the saturation profile at 1.2 PVI obtained by solving the fine scale problem.

The refinement criterion used in q-QG is modified to refine the grid at zero permeabilities as well as high flow areas. The new refinement *heuristic* is denoted by qh-QG. The resulting grid for coarsening level 2 is shown in Figure 6.16**(c)** with 1681 cells, refining both the areas containing barriers and inducing high flow. The resultant saturation pro-

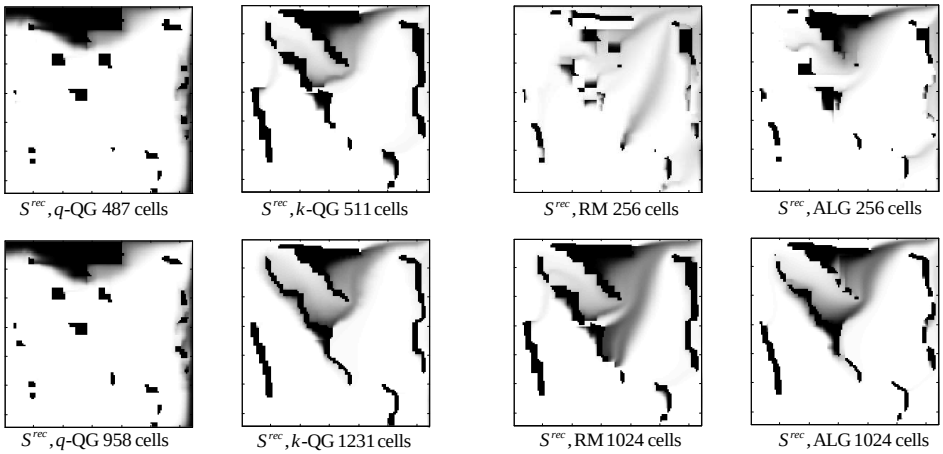

Figure 6.15: The saturation profiles obtained by downscaling of q-QG, k-QG, RM and ALG modelsat t=1.2 PVI. Water is shown in white and oil in black.

file from downscaling of tracer flow simulation on this grid is shown at Figure 6.16**(d)**. For RM with 1024 cells and ALG with 1024 cells, the obtained saturation profiles after velocity downscaling are shown in Figure 6.16 **(e)** and **(f)**, respectively. At t=1.2 PVI, the value of $\delta(s)$ for RM with 1024 cells, ALG with 1024 cells, q-QG with 1417 cells and qh-QG with 1681 cells is 0.58, 0.50, 0.52 and 0.20, respectively. These numbers shows qh-QG gives significantly smaller errors in comparison to other methods. We plotted water cut curves obtained by these three models at two coarsening levels in Figure 6.17. The water cut curves demonstrate that qh-QG model produce considerably more accurate results in comparison to RM and ALG.

Now we examine the model with multiphase flow with viscosity ratios as before. We only assess the models at the coarsening level 1. The water cut curves obtained by $M = 0.1$ and $M = 10$ are shown in Figure 6.18 at t=1.2 PVI. At this time $\delta(s)$ for RM with 256 cells, ALG with 256 cells and qh-QG with 565 cells for $M = 0.1$ is 0.6040, 0.5569 and 0.52, respectively. For $M = 10$ the values are 0.57, 0.46 and 0.39. These results shows that qh-QG for multiphase flow especially case of $M = 0.1$ is not as effective as in the case of tracer flow simulation. This might be attributed to the lack of multiphase flow upscaling method for the relative permeabilities used in the model. However, qh-QG outperforms all other methods presented in this study in terms of estimated error norms.

6.2.5 Summary of Results

We have presented a critical evaluation of different methods of quadtree construction. These methods were compared to uniform grid upscaling. For the quadtree design,

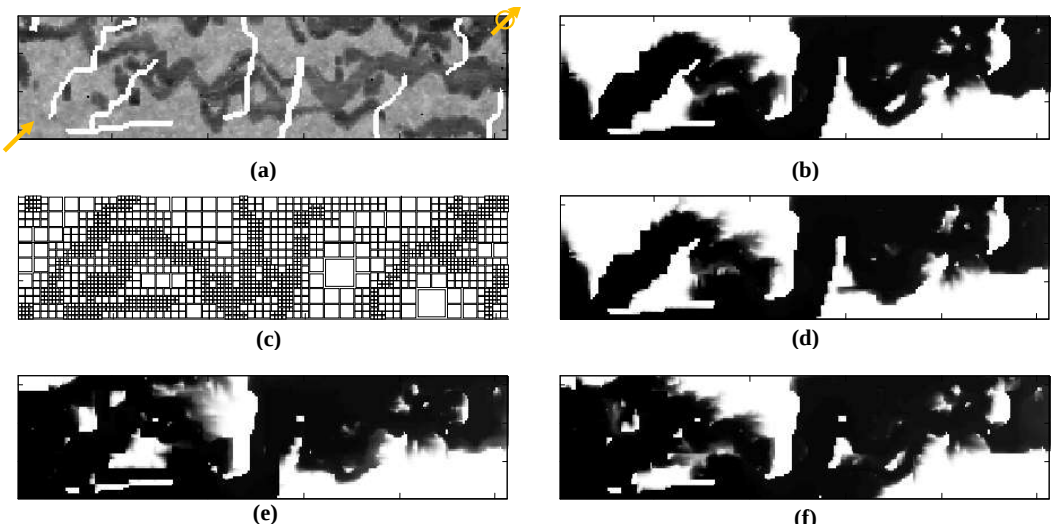

Figure 6.16: Tracer flow simulation on layer 37 combined with few streaks of shale. **(a)** The permeability field,**(b)** the saturation profile at t=1.2 PVI, black is water while white is oil, **(c)** the *qh*-QG model, **(d)** the saturation profile at 1.2 PVI from *qh*-QG downscaled velocities, **(e)** the saturation profile at 1.2 PVI from RM downscaled velocities and **(f)** the saturation profile at 1.2 PVI from ALG downscaled velocities.

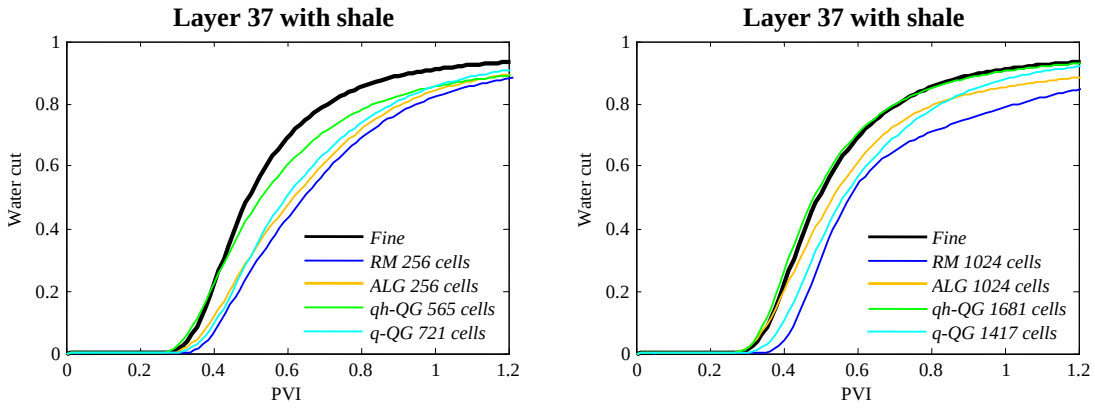

Figure 6.17: The water cut curves for layer 37 with shale at two coarsening levels, tracer flow simulation.

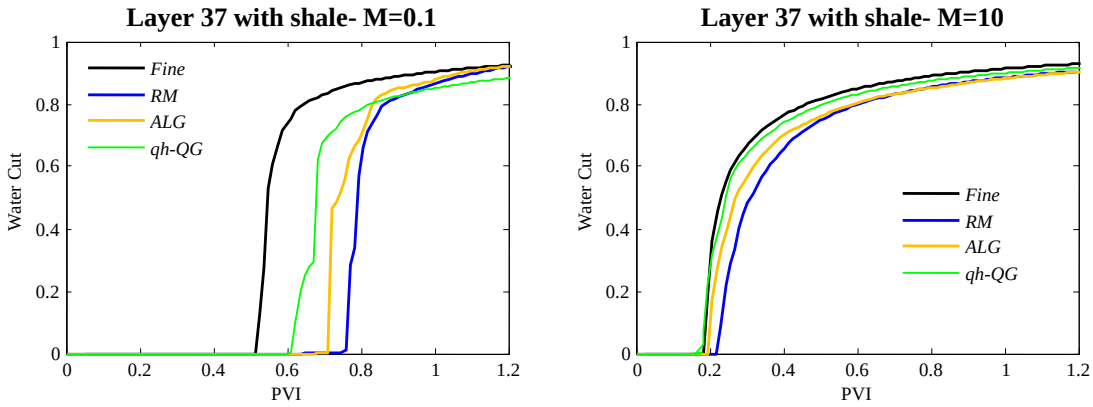

Figure 6.18: The water cut curves for layer 37 with shale at two viscosity ratios, multiphase flow simulation. Left figure shows the result for coarsening level 1 and right figure shows the results is for the coarsening level 2.

two adaptivity criteria were considered: flow-based and permeability-based. For the uniform grid, renormalization and local-global upscaling were used. Based on the extensive numerical testing on single phase and multiphase flow simulations the following conclusions are drawn:

1. A permeability-based non-uniform quad-tree grid (k-QG) led to significant errors in tracer flow simulations of a channelized systems. This can be attributed to either the loss of channels continuity or to an inaccurate grid refinement.

2. A flow-based non-uniform quad-tree grid (q-QG) coupled with renormalization upscaling showed good results compared to adaptive local-global (ALG) upscaling for the production outputs in the tracer flow test cases. The production quantities were the water cut and oil flow rate divided by the pressure drop along the domain. The global error norms, however, showed that ALG upscaling is more accurate in positioning the details of the subgrid flow.

3. For the case of multiphase simulations, the quality of q-QG water cut curves depended on the viscosities of engaging fluids. For high values of viscosity ratios (ratio of viscosity of displaced fluid over viscosity of displacing one) we have a satisfying agreement between q-QG and the fine model for the production outputs. For low values of viscosity ratio, the production data obtained by q-QG shows some deviation from the reference results. For high viscosity ratios, this can be largely attributed to the predominantly streaming flow through the channels and streaks that the non-uniform grid has refined around. In contrast, for the case

of low viscosity ratios, the flow is piston-like, hence more sweep-efficient, and not necessarily dispersing through the channels.

4. Finally, we inserted streaks of shale as forms of barriers inside a test reservoir. For this pattern, q-QG model was tuned heuristically for refining around the shale in addition to the flow based refinement indicator. For the tracer flow case, the results in terms of water production values and saturation profiles were comparable to the fine scale solution. For the multiphase case and low viscosity ratios the results were sensitive to grid quality. However, for high viscosity ratio the grid performed reasonably well in terms of the production curves.

Quadtrees can be dynamically adapted during the simulation time. This might result in a robust method for dynamic upscaling for multiphase flow problems. In the context of reservoir flow simulation, dynamic grids for EOR processes have been tested by Heinemann *et al.* (1983) and Edwards (1996b). However, the presence of extreme heterogeneities, barriers or high flow channels have not been examined there. Trangenstein (2002), Pau *et al.* (2009) and Chueh *et al.* (2010) have applied solution-based evolving grids for flow in porous media with some success. However, these studies did not consider permeabilities upscaling/downscaling effects and the effects of flow barriers and other forms of extreme heterogeneity on the performance of the grid. Testing dynamically adapted flow based quadtree grids combined with downscaling is a promising line of future research.

7 Conclusions and Future Directions

7.1 Conclusions

In this thesis several aspects of upscaling of flow in porous media were investigated and a static downscaling was proposed and tested.

First, in Chapter 3, we used an operator coarsening approach for upscaling with the help of Haar wavelet transformation. The methodology resembled the renormalization approach using a hierarchy of coarsening. The method presented a transformation matrix with which we could upscale the pressure equation discretized operator. The transformed operator had different blocks where each block corresponded to an identifiable section of the transferred pressure solution. The transferred solution constitutes the averages at a specific coarsening level plus a hierarchy of details or differences from the coarsest to the finest levels.

We decided to keep only the block corresponding to the average pressure terms. This is equivalent to neglecting the pressure fluctuations away from the averages. The results of application of the wavelet-based coarsened operator for layers of SPE10 Model 2 were compared to a group of upscaling methods described in Chapter 2: the renormalization method, the pressure solver method and the adaptive local-global method.

The renormalization method uses a closed-form formula derived from resistor analogy. The pressure solver method, uses local flow solutions of the pressure equation obtained from constant pressure boundary condition on two sides of the local region. The boundary condition is similar to resistor analogy's derivation of the formula for equivalent permeability. Unlike such choice of boundary conditions, adaptive local global upscaling adapts boundary conditions calculated form the coarse pressure values. An iteration follows and the global information is incorporated into the local solutions to enhance the quality of upscaling. We used a version of adaptive local global upscaling in which transmissibilities rather than permeabilities are upscaled. For multiphase flow, we added effects of total mobility change into the upscaled transmissibilities for adaptive local global method. This inclusion substitutes relative permeability upscaling and pseudofunction generation.

We started the comparisons for checker-board pattern, a synthetically created set of realizations of permeability and two two-dimensional subsets of SPE10 Model 2. Results

showed adaptive local global method is most accurate due to the ability of the algorithm to capture the subgrid flow complexities. For the renormalization method and pressure solver method the results were very similar, this can be attributed to the similarities in the algorithms of these methods when deriving the equivalent block permeability. For the wavelet coarsened operator, however, the results for the heterogeneous examples were only better than the arithmetic mean. We concluded that unless a more accurate operator based on including the difference blocks is developed, we cannot expect satisfying results from the current method. In this case, the new enriched operator is able to solve a coarse pressure beyond the mean field approximation.

We did not go further in implementing other upscaling techniques. The problem of upscaling remains a challenge. The only conclusion is that whereas wavelet operator coarsening is not a solution, renormalization and the pressure solver methods are only limited solutions and adaptive local global upscaling is an expensive solution to this challenge.

Then we turned our attention to discretization error in representing the derivatives that is affecting the production curves in upscaling techniques. Hence, we dedicated Chapter 4 to developing a static downscaling algorithm. By upscaling-downscaling in a dual mesh framework, we solved the pressure in the coarse scale, then we downscaled the velocities and finally we solved the saturation in the fine scale. We coupled adaptive local global upscaling with a modified nested-gridding downscaling. The resulting upscaling-static-downscaling algorithm showed acceptable reduction of "discretization error", leaving only the "upscaling error". This is the error due to discarding the subgrid flow complexities and inaccurate assignment of equivalent upscaled permeabilities by a poor upscaling method.

The application was examined for different heterogeneity patterns in two and three dimensions and using different boundary conditions. In terms of accuracy, we observed good performance of adaptive local global upscaling coupled by nested gridding downscaling for the production curves. For the saturation profiles, the performance of upscaling downscaling was generally satisfactory but not exact.

The static downscaling provided computational advantages compared to the conventional downscaling. This was achieved by defining building blocks as the basis functions for the fine scale velocity field. The results compared to the dynamic downscaling (where the coarse velocity is downscaled at all time steps) showed minimal deterioration of quality of the reconstructed saturation profiles. The results confirmed the argument by Aarnes & Efendiev (2006) that used homogenization theory to prove that under some assumptions, the two-phase flow velocity, can be approximated by a static part that does not depend on saturation, times a time dependent function in each coarse

block.

The computational saving for static downscaling is subject to the size of the system, computer memory and processing power. However, one thing obvious is the gain in not solving as many equations as number of coarse grid blocks that each of which is as large as number of geomodel fine cells inside the coarse grid block. More precisely if a solver for solving a linear system of size $n \times n$ takes a CPU time of $t(n) = O(n^{\alpha})$ with α a varying number larger than one, then we save computations from dynamic downscaling minus the basis functions generations for static downscaling at initial time. This can be written as $M\left(\sum_{i=1}^{N_c} t(n_i)\right) - 2^D\left(\sum_{i=1}^{N_c} t(n_i)\right)$, which N_c is the number of coarse grid blocks, n_i is the number of fine cells inside coarse grid block i, M is the number of times that we have to perform downscaling and D is dimension of the system.

The modification in the downscaling is from the use of an approximated velocity field, obtained from upscaling stage by adaptive local global method, to define boundary conditions in the reconstruction stage. This enhanced the quality of the saturation profiles for the highly heterogeneous and high upscaling factor values. Furthermore for comparison studies we examined a multiscale algorithm and we concluded that unless the multiscale algorithm is improved to capture global effects, the upscaling-static-downscaling performs better in heterogeneous models.

Regarding the fact that we used the simplest geometrical form for a reservoir grid, we have to consider the applicability of static downscaling for more general "corner point geometry" (distorted grids). The gird can better adapt the grid to reservoir boundaries, faults, horizontal wells and flow patterns and is easily used in standard finite difference reservoir simulators. The corner point geometry can represent complex reservoir geometries by specifying the corners of each grid block in grid building. Such geometry, however, would be still suitable for downscaling, as we are able to define basis functions for each edges. For geometrically flexible grids such as Voronoi polygons or Delaunay triangles, the downscaling is actually less justified, since the grid must have been designed to resolve around fine scale details and reduce numerical diffusion by itself.

Application of static downscaling for large reservoir models that contain around million grid blocks should be reasonable when we consider the displacement process can be often a very local phenomenon spatially and temporally. At these cases there should be limited locations to resolve saturation profiles. The downscaling of fluxes are then limited to the interested areas and simple interpolation of fluxes are used elsewhere. At this case, the upscaling-downscaling is very suitable for a physical system where different processes occur in different parts of a domain and on different scales. Subsequently a streamline simulator or a multiscale saturation solver can be called at fine scale for

higher resolutions.

The reasonable performance of static downscaling motivated us to test it for a range of EOR processes in Chapter 5. The results were very promising. They were established based on examination of the method for two and three dimensional polymer, surfactant and thermal flooding. We concluded that in the case of an EOR process with rather more complicated physics than waterflooding, it was enough to rely on a good upscaling to inform the statically computed velocity basis functions about the flow details. Then the basis functions that were statically computed similar to Chapter 4 can be used to downscale the velocity. The information coming from the upscaled method, however, was very crucial for accurate capturing of a secondary shock caused by solute and its consequent increase in water (or aqueous phase) cut in the production cell. In fact, the basis functions used in such a development seem to have only a trivial role in distributing the flux over a coarse grid area and only the subgrid heterogeneity must somehow be honoured. The complexities of saturation changes, apparently are all works of the total mobility changes which were captured by adaptive local global upscaled transmissibilities sufficiently at coarse scale or the fractional flow functions affecting the saturation equation which was solved at fine scale.

Although the EOR flooding example processes were perhaps oversimplified in comparison to more realistic cases, the difference will not be fundamental. For example we already know that the algorithm works for low-salinity flooding and shear-rate dependent polymer flooding. Modelling the physics of these processes requires that in low-salinity flooding both reduction of residual oil saturation and modification of relative permeabilities be accounted for whereas in shear-rate dependent polymer flooding, the viscosities should be iteratively updated based on the flux magnitude. All these physical details only affect the saturation equation coefficients at the fine scale. As mentioned in the text dealing with the upscaling of the saturation equation or the derivation of pseudo-relative permeabilities were not our objective. Consequently, we are sure that as long as the process is incompressible and immiscible, we will have satisfying performance for our upscaling-static-downscaling algorithm.

In Chapter 6 a non-uniform quadtree grid generation algorithm is developed and applied for tracer and multiphase flow in channelized heterogeneous porous media. Grid generation was guided using two different approaches. In the first approach, wavelet transformation was used to generate a refinement field based on permeability variations. The second approach uses flow information based on the solution of an initial-time fine-scale problem. The resulting grids were compared with uniform grid upscaling. For uniform upscaling, two commonly applied methods were used: renormalization upscaling and local-global upscaling. The velocities obtained by non-uniformly and

uniformly upscaled grids, were downscaled. This procedure allows us to separate the upscaling errors, on non-uniform and uniform grids, from the numerical diffusion errors resulting from solving the saturation equation on a coarse grid. The simulation results obtained by solving on flow-based quadtree grids for the case of a single phase flow show reasonable agreement with more computationally demanding fine-scale models and local-global upscaled models. For the multiphase case, the agreement is less evident, especially in piston-like displacement cases with sharp frontal movement. Furthermore, existence of barriers in a porous medium complicates both upscaling and grid adaptivity. This issue is addressed by adjusting the grid using a combination of flow information and a permeability based heuristic criterion.

The computational saving by using a quadtree grid is obvious once we consider fewer grid blocks in the model than the uniform coarse grid model. Given that in our examples the construction was procedurally simple and renormalization was readily used, the use of the quadtree models looked very promising and rendered a good alternative for the adaptive local global upscaling. In reservoir applications, however, it is very rare to see uniform size grid models represented in quadtree or octtree (for 3D) structures. For unequal size grid models, as long as they are structured (similar to corner point geometry grids), we can perform divisions and mergers fairly easily. Then the concern is the criteria of grid generation. It might be not easily feasible to run a fine scale flow simulation on a million grid block model to decide where to coarsen and where to leave at fine scale or finer scales. One suggestion is to use parts of the model separately to run the flow and generate the grid. Then the parts of the system that are fairly homogeneous can be discarded for flow-based grid generation stage. Another concern is the boundary conditions and changes in them throughout the simulation. The practical implications that decide whether we are able to adjust the grid to varying global boundary conditions by a dynamic adaptive setting and by an optimised and computationally reasonable procedure should be carefully considered.

As mentioned above any upscaling technique can be used for assigning equivalent permeability values to the generated non-uniform grid. For example a *non-iterative* transmissibility upscaling procedure for quadtree grid can significantly reduce the errors and make the non-uniform quadtree grid more comparable to the *iterative* adaptive local-global upscaling. In this case, although we might avoid iteration to correct the boundary conditions for the quadtree grid transmissibilities, for multiphase flow case we can update the transmissibilities to account for the total mobility change throughout the simulation.

7.2 Future Work

This thesis focused on looking at the permeability and transmissibility upscaling coupled with static downscaling or combined with non-uniform Cartesian quadtree grid generation. To build on the results of this research, for three topics of upscaling, upscaling-downscaling and non-uniform grid generation combined with upscaling, the followings are recommended.

For upscaling:

- Advanced techniques such as near well upscaling can resolve adequately around the well so that we do not need downscaling to reduce the diffusion error.
- It should be investigated whether an optimised, process independent multiphase flow upscaling of relative permeability curves, can be a solution to reducing the numerical diffusion error. If this is the case, downscaling is not recommended.
- For three dimensional case, an efficient adaptive local global upscaling method enhanced with full tensor permeability or transmissibility upscaling may result in more robust upscaling-downscaling performances.
- Use of a higher order accurate finite difference scheme for the simulation which minimizes numerical diffusion is recommended. Such implementations may also lead to adequate reduction of numerical diffusion such that downscaling becomes redundant.

For upscaling-downscaling:

- An application of downscaling for practical cases of reservoir simulation in conjunction with the use a commercial simulator such as ECLIPSE to provide coarse scale velocity field from a realistic model. The downscaling can be performed separately, and the results fed back to the commercial simulator. We have to be very consistent about the read and write formats for ECLIPSE and equally careful about rather more sophisticated well and boundary conditions and their effects on downscaling.
- The addition of gravity and capillarity on upscaling-downscaling is recommended. The operator splitting procedure that was suggested should allow us to be still able to use the basis function of the incompressible cases. However the gravity velocities need a frequent updating because they are more dynamic than the incompressible viscous velocities. In such cases the computational savings by static downscaling will be less pronounced.

- The investigation of upscaling-static-downscaling for the reservoir processes other than incompressible displacements is recommended. The performance of our proposed upscaling-static-downscaling may be different for compressible, compositional or miscible flow cases. The methodology may need complete revisions and may not even work for dynamic flow cases such as compressible flow. The pressure-dependent densities for compressible cases may cause serious errors once we switch the scale in upscaling-downscaling. As we just proposed in the thesis, corrective terms can be added to account for the changes in the properties of fluid that are averaged out in upscaling and introduces error in downscaling.

- For large scale reservoir simulations, parallelisation of computations is recommended. We may be able to benefit from decoupled process of downscaling form a coarse grid block to another. In case that grid blocks contain considerable number of fine cells (large upscaling ratio), the decoupled process will allow us to implement a parallelisation in calculating the basis functions at initial time. Such implementation will lead to higher computational efficiencies.

- To build basis functions for the transport or saturation equation, is another line of research that we recommend for future work. Such development requires special inter-scalar interpolation operators that map each coarse grid saturation field onto a fine scale saturation profile that is close to the corresponding profile that one would get by solving saturation equation on the global fine grid.

- Use of upscaling-static-downscaling in conjunction with a streamline-based ranking approach that will adequately represent the uncertainties in the reservoir performance predictions is also recommended.

For grid generation combined with upscaling:

- Generation of dynamic adaptive non-uniform quad-trees or oct-trees is recommended. Testing such grids combined with procedurally simple permeability or transmissibility upscaling and combined with downscaling (if needed) can be a promising line of future research. The combination, however, must result in better computational runtime and more accuracy compared to the unstructured geometrically flexible grids.

Bibliography

Aarnes, J.E. (2004). On the use of a mixed multiscale finite element method for greater flexibility and increased speed or improved accuracy in reservoir simulation. *Multiscale Modeling & Simulation*, **2**, 421–439. 77, 78, 84

Aarnes, J.E. & Efendiev, Y. (2006). An adaptive multiscale method for simulation of fluid flow in heterogeneous porous media. *Multiscale Modeling & Simulation*, **5**, 918. 43, 85, 165

Aarnes, J.E., Krogstad, S. & Lie, K.A. (2006). A hierarchical multiscale method for two-phase flow based upon mixed finite elements and nonuniform coarse grids. *Multiscale Modeling & Simulation*, **5**, 337–363. 78, 157

Aarnes, J.E., Kippe, V., Lie, K.A. & Rustad, A.B. (2007). Modelling of multiscale structures in flow simulations for petroleum reservoirs. *Geometric Modelling, Numerical Simulation, and Optimization*, 307–360. 16, 17

AlSofi, A.M. & Blunt, M.J. (2010). Control of numerical dispersion in simulations of augmented waterflooding. In *SPE Paper 129658-MS, Proceedings of SPE Symposium on Improved Oil Recovery, Tulsa, Oklahoma*. 118

AlSofi, A.M. & Blunt, M.J. (2012). A segregated flow scheme to control numerical dispersion for multi-component flow simulations. *Computational Geosciences*, **16**, 1–16. 118

Audigane, P. & Blunt, M.J. (2004). Dual mesh method for upscaling in waterflood simulation. *Transport in Porous Media*, **55**, 71–89. 18, 79

Aziz, K. & Settari, A. (1979). *Petroleum Reservoir Simulation*. Kluwer Academic Publishers. 26, 28

Barker, J. & Thibeau, S. (1997). A critical review of the use of pseudorelative permeabilities for upscaling. *SPE Reservoir Engineering*, **12**, 138–143. 17, 41, 43

Barker, J., Maarten, C. & Lars, H. (2000). Quantifying uncertainty in production forecasts: Another look at the punq-s3 problem. In *SPE Annual Technical Conference and Exhibition*. 14

Batycky, R.P., Blunt, M.J. & Thiele, M.R. (1997). A 3D field-scale streamline-based reservoir simulator. *SPE Reservoir Engineering*, **12**, 246–254. 30

Bear, J. (1972). *Dynamics of Fluids in Porous Media*. Dover Publications, Inc. 26

Begg, S.H., Carter, R.R. & Dranfield, P. (1989). Assigning effective values to simulator gridblock parameters for heterogeneous reservoirs. *SPE Reservoir Engineering*, **4**, 455–463. 18, 33

Bratvedt, F., Gimse, T. & Tegnander, C. (1996). Streamline computations for porous media flow including gravity. *Transport in Porous Media*, **25**, 63–78. 85

Bratvold, R.B. (1989). *An analytical study of reservoir pressure response following cold water injection*. Ph.D. thesis, Stanford Univ. 125

Buckley, S.E. & Leverett, M.C. (1942). Mechanism of fluid displacement in sands. *Trans. AIME*, **146**, 107–116. 110

Burrus, C.S., Gopinath, R.A. & Guo, H. (1998). *Introduction to wavelets and wavelet transforms: a primer*, vol. 23. Prentice Hall Upper Saddle River NJ. 49

Busby, D., Farmer, C.L. & Iske, A. (2007). Uncertainty evaluation in reservoir forecasting by bayes linear methodology. *Algorithms for Approximation*, 187–196. 15

Cardwell, W.T. & Parsons, R.L. (1945). Average permeabilities of heterogeneous sands. *Transactions of the American Institute of Mining*, 34–42. 32

Carlson, M.R. (2003). *Practical reservoir simulation: using, assessing, and developing results*. PennWell Books. 13, 15

Carr, A.H. & Christie, M.A. (1983). Controlling numerical diffusion in reservoir simulation using flux corrected transport. In *SPE Paper 12235-MS, Proceedings of SPE Reservoir Simulation Symposium, San Francisco, California*. 18

Castellini, A. (2001). *Flow based grids for reservoir simulation*. Master's thesis, Stanford University, Stanford, CA. 91

Castellini, A., Edwards, M.G. & Durlofsky, L.J. (2000). Flow based modules for grid generation in two and three dimensions. In *Proceedings of 7th European Conference on the Mathematics of Oil Recovery, Baveno, Italy*. 20

Chen, Y. & Durlofsky, L.J. (2006). Adaptive local-global upscaling for general flow scenarios in heterogeneous formations. *Transport in Porous Media*, **62**, 157–185. 18, 41, 44, 139

Chen, Y., Durlofsky, L.J., Gerritsen, M. & Wen, X.H. (2003). A coupled local-global upscaling approach for simulating flow in highly heterogeneous formations. *Advances in Water Resources*, **26**, 1041–1060. 40, 41, 79

Chen, Y., Durlofsky, L.J. & Wen, X.H. (2004). Robust coarse scale modeling of flow and transport in heterogeneous reservoirs. In *Proceedings of 9th European Conference on the Mathematics of Oil Recovery, Cannes, France*, vol. 30. 99

Chen, Z. & Hou, T.Y. (2003). A mixed multiscale finite element method for elliptic problems with oscillating coefficients. *Mathematics of Computation*, **72**, 541–576. 45

Christie, M.A. (1996). Upscaling for reservoir simulation. *Journal of Petroleum Technology*, **48**, 1004–1010. 33

Christie, M.A. & Blunt, M.J. (2001). Tenth SPE comparative solution project: A comparison of upscaling techniques. *SPE Reservoir Evaluation & Engineering*, **4**, 308–317. 70, 92

Chueh, C.C., Secanell, M., Bangerth, W. & Djilali, N. (2010). Multi-level adaptive simulation of transient two-phase flow in heterogeneous porous media. *Computers & Fluids*, **39**, 1585–1596. 163

Claridge, E.L. & Bondor, P.L. (1974). A graphical method for calculating linear displacement with mass transfer and continuously changing mobilities. *Society of Petroleum Engineers Journal*, **14**, 609–618. 110

Cosentino, L. (2001). *Integrated reservoir studies*. Editions Technip. 14, 15

Darcy, H. (1856). *Les Fontaines Publiques de la Ville de Dijon*. Dalmount, Paris. 25

Darman, N.H., Durlofsky, L.J., Sorbie, K.S. & Pickup, G.E. (2001). Upscaling immiscible gas displacements: quantitative use of fine-grid flow data in grid-coarsening schemes. *SPE Journal*, **6**, 47–56. 20

Das, D.B. & Hassanizadeh, S.M. (2005). *Upscaling multiphase flow in porous media: From pore to core and beyond*, vol. 200. Springer. 17

Daubechies, I. (1992). *Ten lectures on wavelets*. CBMS-NSF Regional conference series in applied mathematics, SIAM, Philadelphia. 48

de Berg, M., van Kreveld, M., Overmars, M. & Schwarzkopf, O. (2000). *Computational Geometry: Algorithms and Applications*. Springer-Verlag, 2nd edn. 141

De Leon, D. (2008). A new wavelet multigrid method. *Journal of Computational and Applied Mathematics*, **220**, 674–685. 59

Demirmen, F. (2007). Reserves estimation: The challenge for the industry. *Journal of Petroleum Technology*, **59**, 80–89. 13

Desbarats, A.J. (1992). Spatial averaging of transmissivity in heterogeneous fields with flow toward a well. *Water Resources Research*, **28**, 757–767. 19

Dindoruk, D. & Dindoruk, B. (2008). Analytical solution of nonisothermal Buckley-Leverett flow including tracers. *SPE Reservoir Evaluation & Engineering*, **11**, 555–564. 125, 126

Ding, Y. (1995). Scaling-up in the vicinity of wells in heterogeneous field. In *SPE Paper 29137-MS, Proceedings of SPE Reservoir Simulation Symposium, San Antonio, Texas*. 19

Donoho, D.L. (1995). De-noising by soft-thresholding. *Information Theory, IEEE Transactions on*, **41**, 613–627. 141

Donoho, D.L. & Johnstone, I.M. (1995). Adapting to unknown smoothness via wavelet shrinkage. *Journal of the american statistical association*, 1200–1224. 141, 142

Dorobantu, M. & Engquist, B. (1998). Wavelet-based numerical homogenization. *SIAM Journal of Numerical Analysis*, 540–559. 59

Durlofsky, L.J. (1991). Numerical calculation of equivalent grid block permeability tensors for heterogeneous porous media. *Water Resources Research*, **27**, 699–708. 18, 31, 33

Durlofsky, L.J. (1997). Use of higher moments for the description of upscaled, process independent relative permeabilities. *SPE Journal*, **2**, 474–484. 43

Durlofsky, L.J. (1998). Coarse scale models of two phase flow in heterogeneous reservoirs: volume averaged equations and their relationship to existing upscaling techniques. *Computational Geosciences*, **2**, 73–92. 43

Durlofsky, L.J. (2005a). Upscaling and gridding of fine scale geological models for flow simulation. In *Proceedings of 8th International Forum on Reservoir Simulation, Iles Borromees, Stresa, Italy*. 20, 21

Durlofsky, L.J. (2005b). Upscaling and gridding of fine scale geological models for flow simulation, paper presented at the 8th International Forum on Reservoir Simulation, Iles Borromees, Stresa, Italy, June 20-24. 40

Durlofsky, L.J., Behrens, R., Jones, R. & Bernath, A. (1996). Scale up of heterogeneous three dimensional reservoir descriptions. *SPE Journal*, **1**, 313–326. 20

Durlofsky, L.J., Jones, R.C. & Milliken, W.J. (1997). A nonuniform coarsening approach for the scale-up of displacement processes in heterogeneous porous media. *Advances in Water Resources*, **20**, 335–347. 20, 143

Durlofsky, L.J., Milliken, W.J. & Bernath, A. (1999). Scale up in the near-well region. In *SPE Paper 51940-MS, Proceedings of SPE Reservoir Simulation Symposium, Houston, Texas*. 19

Durlofsky, L.J., Efendiev, Y. & Ginting, V. (2007). An adaptive local-global multiscale finite volume element method for two-phase flow simulations. *Advances in Water Resources*, **30**, 576–588. 107

Dykhne, A.M. (1971). Conductivity of a two-dimensional two-phase system. *Soviet Journal of Experimental and Theoretical Physics*, **32**, 63. 36

Ebrahimi, F. & Sahimi, M. (2002). Multiresolution wavelet coarsening and analysis of transport in heterogeneous media. *Physica A: Statistical Mechanics and its Applications*, **316**, 160–188. 141

Ebrahimi, F. & Sahimi, M. (2004). Grid coarsening, simulation of transport processes in, and scale-up of heterogeneous media: Application of multiresolution wavelet transformations. *Mechanics of Materials*, **38**, 772–785. 141

Edwards, M.G. (1996a). Elimination of adaptive grid interface errors in the discrete cell centered pressure equation. *Journal of Computational Physics*, **126**, 356–372. 144

Edwards, M.G. (1996b). A higher-order godunov scheme coupled with dynamic local grid refinement for flow in a porous medium. *Computer Methods in Applied Mechanics and Engineering*, **131**, 287–308. 163

Efendiev, Y. & Durlofsky, L.J. (2002). Numerical modeling of subgrid heterogeneity in two phase flow simulations. *Water Resources Research*, **38**, 1128. 43

Efendiev, Y. & Durlofsky, L.J. (2003). A generalized convection-diffusion model for subgrid transport in porous media. *Multiscale Modeling and Simulation*, **1**, 504–526. 43

Efendiev, Y., Durlofsky, L.J. & Lee, S.H. (2000). Modeling of subgrid effects in coarse-scale simulations of transport in heterogeneous porous media. *Water Resources Research*, **36**, 2031–2041. 43

Efendiev, Y., Ginting, V., Hou, T. & Ewing, R. (2006). Accurate multiscale finite element methods for two-phase flow simulations. *Journal of Computational Physics*, **220**, 155–174. 107

Elsheikh, A.H. (2007). *Multiscale a posteriori error estimation and mesh adaptivity for reliable finite element analysis*. Ph.D. thesis, McMaster University, Ontario, Canada. 139

Essley, P.L. (1965). What is reservoir engineering? *Journal of Petroleum Technology*, **17**, 19–25. 13

Farmer, C.L. (2002). Upscaling: a review. *International Journal for Numerical Methods in Fluids*, **40**, 63–78. 17, 39, 40, 65

Farmer, C.L. (2005). Geological modelling and reservoir simulation. *Mathematical Methods and Modelling in Hydrocarbon Exploration and Production*, 119–212. 14, 17

Farmer, C.L., Heath, D.E. & Moody, R.O. (1991). A global optimization approach to grid generation. In *SPE Paper 21236-MS, Proceedings of SPE Symposium on Reservoir Simulation, Anaheim, California*. 20

Floris, F.J.T., Bush, M.D., Cuypers, M., Roggero, F. & Syversveen, A.R. (2001). Methods for quantifying the uncertainty of production forecasts: a comparative study. *Petroleum Geoscience*, **7**, S87–S96. 14

Forsyth, P. & Sammon, P. (1986). Local mesh refinement and modeling of faults and pinchouts. *SPE Formation Evaluation*, **1**, 275–285. 144

Garcia, M., Journel, A. & Aziz, K. (1992). Automatic grid generation for modeling reservoir heterogeneities. *SPE Reservoir Engineering*, **7**, 278–284. 20

Gautier, Y. & Noetinger, B. (1997). Preferential flow-paths detection for heterogeneous reservoirs using a new renormalization technique. *Transport in Porous Media*, **26**, 1–23. 36

Gautier, Y., Blunt, M.J. & Christie, M.A. (1999). Nested gridding and streamline-based simulation for fast reservoir performance prediction. *Computational Geosciences*, **3**, 295–320. 18, 79, 81

Gerritsen, M. & Lambers, J.V. (2008). Integration of local-global upscaling and grid adaptivity for simulation of subsurface flow in heterogeneous formations. *Computational Geosciences*, **12**, 193–208. 154

Gómez-Hernández, J.J. & Journel, A.G. (1990). Stochastic characterization of grid-block permeabilities: from point values to block tensors. In *Proceedings of 2nd European Conference on the Mathematics of Oil Recovery, Arles, France*, 83–90, Arles, France. 32

Green, D.W. & Willhite, G.P. (1998). *Enhanced Oil Recovery*, vol. 6 of *SPE textbook series*. Society of Petroleum Engineers, Richardson, TX. 110, 113

Guérillot, D.R. & Verdière, S. (1995). Different pressure grids for reservoir simulation in heterogeneous reservoirs. In *SPE Paper 29148-MS, Proceedings of SPE Reservoir Simulation Symposium, San Antonio, Texas*. 18, 45, 79

Guzman, R.E., Domenico, G., Fayers, F.J., Antonella, G. & Aziz, K. (1999). Evaluation of dynamic pseudofunctions for reservoir simulation. *SPE Journal*, **4**. 42

Haar, A. (1909). *Zur Theorie der orthogonalen Funktionensysteme*. Ph.D. thesis, Goettingen. 48

Hajibeygi, H. & Jenny, P. (2009). Multiscale finite-volume method for parabolic problems arising from compressible multiphase flow in porous media. *Journal of Computational Physics*, **228**, 5129–5147. 88

Hauge, V.L., Lie, K.A. & Natvig, J.R. (2012). Flow-based coarsening for multiscale simulation of transport in porous media. *Computational Geosciences*, **16**, 391–408. 90

He, C. (2005). *Structured flow-based gridding and upscaling for reservoir simulation*. Ph.D. thesis, Stanford University. 20, 91

He, C. & Durlofsky, L.J. (2006). Structured flow-based gridding and upscaling for modeling subsurface flow. *Advances in Water Resources*, **29**, 1876–1892. 20

Heinemann, Z.E., Gerken, G. & von Hantelmann, G. (1983). Using local grid refinement in a multiple-application reservoir simulator. In *SPE Paper 12255-MS, Proceedings of SPE Reservoir Simulation Symposium, San Francisco, California*. 163

Heinemann, Z.E., Brand, C.W., Munka, M. & Chen, Y.M. (1991). Modeling reservoir geometry with irregular grids. *SPE Reservoir Engineering*, **6**, 225–232. 20

Hesse, M.A. (2008). *Mathematical modeling and multiscale simulation of CO2 storage in saline aquifers*. Ph.D. thesis, Stanford University. 45

Hinrichsen, E.L., Aharony, A. & Feder, J. (1993). A fast algorithm for estimating large-scale permeabilities of correlated anisotropic media. *Transport in Porous Media*, **12**, 55–72. 36

Holden, L. & Nielsen, B.F. (2000). Global upscaling of permeability in heterogeneous reservoirs; the output least squares (OLS) method. *Transport in Porous Media*, **40**, 115–143. 40

Hou, T.Y. & Wu, X.H. (1997). A multiscale finite element method for elliptic problems in composite materials and porous media. *Journal of Computational Physics*, **134**, 169–189. 75, 76, 78

Hristopulos, D.T. (2003). Renormalization group methods in subsurface hydrology: overview and applications in hydraulic conductivity upscaling. *Advances in Water Resources*, **26**, 1279–1308. 34

Hristopulos, D.T. & Christakos, G. (1999). Renormalization group analysis of permeability upscaling. *Stochastic Environmental Research and Risk Assessment*, **13(12)**, 131–160. 34

Jacks, H., Smith, O. & Mattax, C.C. (1973). The modeling of a three-dimensional reservoir with a two-dimensional reservoir simulator-the use of dynamic pseudo functions. *SPE Journal*, **13**, 175–185. 42

Jenny, P., Lee, S.H. & Tchelepi, H.A. (2003). Multiscale finite-volume method for elliptic problems in subsurface flow simulation. *Journal of Computational Physics*, **187**, 47–67. 75, 84

Jenny, P., Lee, S.H. & Tchelepi, H.A. (2005). Adaptive multiscale finite-volume method for multiphase flow and transport in porous media. *Multiscale Modeling and Simulation*, **3**, 50–64. 44, 76, 77

Jenny, P., Lee, S.H. & Tchelepi, H.A. (2006). Adaptive fully implicit multiscale finite-volume method for multiphase flow and transport in heterogeneous porous media. *Journal of Computational Physics*, **217**, 627–641. 77, 80

Journel, A.G., Deutsch, C. & Desbarats, A.J. (1986). Power averaging for block effective permeability. In *SPE Paper 15128-MS, Proceedings of SPE California Regional Meeting*. 18, 32

Khoozan, D., Firoozabadi, B., Rashtchian, D. & Ashjari, M.A. (2011). Analytical dual mesh method for two-phase flow through highly heterogeneous porous media. *Journal of Hydrology*, **400**, 195–205. 85

King, P.R. (1987). The use of field theoretic methods for the study of flow in a heterogeneous porous medium. *Journal of Physics A: Mathematical and General*, **20**, 3935–3947. 33

King, P.R. (1989). The use of renormalization for calculating effective permeability. *Transport in Porous Media*, **4**, 37–58. 34, 35

King, P.R. (1996). Upscaling permeability: Error analysis for renormalization. *Transport in porous media*, **23**, 337–354. 36, 65

King, P.R., Muggeridge, A.H. & Price, W.G. (1993). Renormalization calculations of immiscible flow. *Transport in Porous Media*, **12**, 237–260. 34

Kippe, V., Aarnes, J.E. & Lie, K.A. (2008). A comparison of multiscale methods for elliptic problems in porous media flow. *Computational Geosciences*, **12**, 377–398. 45, 70, 90, 105

Kyte, J.R. & Berry, D.W. (1975). New pseudo functions to control numerical dispersion. *Society of Petroleum Engineers Journal*, **15**, 269–276. 42

Landau, L.D. & Lifshitz, E.M. (1960). *Electrodynamics of Continuous Media*. Pergamon, Oxford. 32

Lantz, R.B. (1971). Quantitative evaluation of numerical diffusion (truncation error). *SPE Journal*, **11**, 315–320. 18

Lee, S.H., Wolfsteiner, C. & Tchelepi, H.A. (2008). Multiscale finite-volume formulation for multiphase flow in porous media: black oil formulation of compressible, three-phase flow with gravity. *Computational Geosciences*, **12**, 351–366. 30

Li, D., Cullick, A.S. & Lake, L.W. (1995). Global scale-up of reservoir model permeability with local grid refinement. *Journal of Petroleum Science and Engineering*, **14**, 1–13. 20

Lie, K.A., Krogstad, S., Ligaarden, I., Natvig, J.R., Nilsen, H.M. & Skaflestad, B. (2011). Open-source matlab implementation of consistent discretisations on complex grids. *Computational Geosciences*, 1–26. 105

Lie, K.A., Natvig, J.R. & Nilsen, H.M. (2012). Discussion of dynamics and operator splitting techniques for two-phase flow with gravity. *International Journal of Numerical Analysis and Modelling (Special issue in memory of Magne Espedal)*, **9**, 684–700. 85

Mahani, H. & Evazi, M. (2010). Vorticity-based perpendicular-bisector grids for improved upscaling of two-phase flow. *SPE Journal*, **15**, 989–1002. 20

Mascarenhas, O. & Durlofsky, L.J. (2000). Coarse scale simulation of horizontal wells in heterogeneous reservoirs. *Journal of Petroleum Science and Engineering*, **25**, 135–147. 19

Matheron, G. (1967). Composition des permeabilites en milieu poreux heterogene: Methode de schwyndler et regles de ponderation. *Revue de l'Institut Francais du Petrole*, **22**, 443–466. 32, 65

Mlacnik, M., Durlofsky, L.J. & Heinemann, Z. (2006). Sequentially adapted flow-based PEBI grids for reservoir simulation. *Society of Petroleum Engineers Journal*, **11**, 317–327. 20

Muggeridge, A.H., Cuypers, M., Bacquet, C. & Barker, J.W. (2002). Scale-up of well performance for reservoir flow simulation. *Petroleum Geoscience*, **8**, 133–139. 19

Niessner, J. & Helmig, R. (2009). Multi-physics modeling of flow and transport in porous media using a downscaling approach. *Advances in Water Resources*, **32**, 845–850. 79

Palagi, C.L. (1992). *Generation and application of Voronoi grid to model flow in heterogeneous reservoirs*. Ph.D. thesis, Stanford University. 20

Pancaldi, V. (2007). *Coarse graining equations for flow in porous media: a Haar wavelets and renormalization approach*. Ph.D. thesis, Imperial College London. 38, 59, 62, 63, 67

Pancaldi, V., Christensen, K. & King, P.R. (2006). Permeability up-scaling using haar wavelets. *Transport in Porous Media*, **67**, 395–412. 38, 57, 61

Pancaldi, V., King, P. & Christensen, K. (2009). Hierarchical coarse-graining transform. *Physical Review E*, **79**, 036704. 38, 62, 63

Pau, G.S.H., Almgren, A.S., Bell, J.B. & Lijewski, M.J. (2009). A parallel second-order adaptive mesh algorithm for incompressible flow in porous media. *Philosophical Transactions of the Royal Society A*, **367**, 4633–4654. 163

Pickup, G.E., Ringrose, P.S., Jensen, J.L. & Sorbie, K.S. (1994). Permeability tensors for sedimentary structures. *Mathematical Geology*, **26**, 227–250. 34

Pope, G. (1980). The application of fractional flow theory to enhanced oil recovery. *SPE Journal*, **20**, 191–205. 110

Prevost, M., Lepage, F., Durlofsky, L.J. & Mallet, J.L. (2005). Unstructured 3D gridding and upscaling for coarse modelling of geometrically complex reservoirs. *Petroleum Geoscience*, **11**, 339–345. 20

Qi, D., Wong, P. & Liu, K. (2001). An improved global upscaling approach for reservoir simulation. *Petroleum Science and Technology*, **19**, 779–795. 20

Quandalle, P. & Besset, P. (1985). Reduction of grid effects due to local subgridding in simulations using a composite grid. In *SPE Paper 13527-MS, Proceedings of SPE Reservoir Simulation Symposium, Dallas, Texas*. 144

Ramé, M. & Killough, J.E. (1992). A new approach to flow simulation in highly heterogeneous porous media. *SPE Formation Evaluation*, **7**, 247–254. 18, 79

Rasaei, M.R. & Sahimi, M. (2008a). Upscaling and simulation of waterflooding in heterogeneous reservoirs using wavelet transformations: application to the SPE-10 model. *Transport in Porous Media*, **72**, 311–338. 141

Rasaei, M.R. & Sahimi, M. (2008b). Upscaling of the permeability by multiscale wavelet transformations and simulation of multiphase flows in heterogeneous porous media. *Computational Geosciences*, **13**, 187–214. 141

Renard, P. & de Marsily, G. (1997). Calculating equivalent permeability: a review. *Advances in Water Resources*, **20**, 253–278. 17, 32, 33

Rietz, D. & Usmani, A. (2009). Case studies illustrating the use of reservoir simulation results in the reserves estimation process. *SPE Reservoir Evaluation & Engineering*, **12**, 149–158. 13

Sahimi, M., Hughes, B.D., Scriven, L.D. & Davis, H.T. (1983). Real-space renormalization and effective-medium approximation to the percolation conduction problem. *Physical Review B*, **28(1)**, 307–311. 38

Schulze-Riegert, R. & Ghedan, S. (2007). Modern techniques for history matching. In *9th International Forum on Reservoir Simulation*, 9–13. 14

Sheng, Y. (2000). Wavelet transform, in "the transforms and applications handbook". *The Electrical Engineering Handbook Series*, 747–827. 50

Sorbie, K.S. (1991). *Polymer-Improved Oil Recovery*. Springer-Verlag. 116

Stein, C.M. (1981). Estimation of the mean of a multivariate normal distribution. *The Annals of Statistics*, **9**, 1135–1151. 142

Stone, H.L. (1991). Rigorous black oil pseudo functions. In *SPE Paper 21207-MS, Proceedings of SPE Symposium on Reservoir Simulation, Anaheim, California*. 42

Talash, A.W. (1976). Experimental and calculated relative permeability data for systems containing tension additives. In *SPE Paper 5810-MS, Proceedings of SPE Improved Oil Recovery Symposium, Tulsa, Oklahoma*. 123

Trangenstein, J.A. (2002). Multiscale iterative techniques and adaptive mesh refinement for flow in porous media. *Advances in Water Resources*, **25**, 1175–1213. 163

Wallstrom, T.C., Hou, S., Christie, M.A., Durlofsky, L.J. & Sharp, D. (1999a). Application of a new two-phase upscaling technique to realistic reservoir cross sections. In *SPE Paper 51939-MS, Proceedings of SPE Reservoir Simulation Symposium, Houston, Texas*. 75

Wallstrom, T.C., Hou, S.L., Christie, M.A., Durlofsky, L.J. & Sharp, D.H. (1999b). Accurate scale up of two phase flow using renormalization and nonuniform coarsening. *Computational Geosciences*, **3**, 69–87. 67

Warren, J.E. & Price, H.S. (1961). Flow in heterogeneous porous media. *Society of Petroleum Engineers Journal*, **1**. 33

Wen, X.H. & Gómez-Hernández, J.J. (1996). Upscaling hydraulic conductivities in heterogeneous media: An overview. *Journal of Hydrology*, **183**, ix–xxxii. 20

Wen, X.H., Durlofsky, L.J. & Edwards, M.G. (2003). Upscaling of channel systems in two dimensions using flow-based grids. *Transport in Porous Media*, 51–343. 20

Wen, X.H., Durlofsky, L.J. & Chen, Y. (2006). Efficient 3D implementation of local-global upscaling for reservoir simulation. *SPE Journal*, **11**, 443–453. 105

Williams, J. (1992). Simple renormalization schemes for calculating effective properties of heterogeneous reservoirs. In P.R. King, ed., *Proceedings of Mathematics of oil recovery*, 281, Clarendon Press, Oxford. 35

Yeo, I. & Zimmerman, R.W. (2001). Accuracy of the renormalization method for computing effective conductivities of heterogeneous media. *Transport in Porous Media*, **45**, 129–138. 36, 65